Astrophysical Constraints on Dark Matter

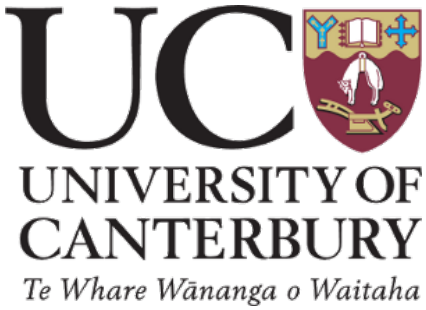

Oscar A. Macías-Ramírez

Department of Physics and Astronomy

University of Canterbury

A thesis submitted for the degree of

Doctor of Philosophy in Physics

November 03, 2014

A Liliana, mi prometida.

Acknowledgements

I would like to express my sincere gratitude to my advisor Dr. Chris Gordon for the continuous support of my Ph.D study and research, for his patience, motivation, enthusiasm, and immense knowledge. His guidance helped me in all the time of research and writing of this thesis. I could not have imagined having a better advisor and mentor for my PhD study.

Besides my advisor, I would like to thank the rest of my thesis committee: Prof. Jenni Adams, Prof. Luis A. Sánchez and Prof. Diego Restrepo, for their encouragement and insightful comments.

I also want to thank my friends and fellow PhD students, old and new - Christoph Bergmann, Cheng-Yang Lee, Ahsan Nazer and Hamish Silverwood - for great company and messing about with a 'proud' Colombian.

My sincere thanks also goes to Rosalie Reilly, Sharlene Mullen and Xuefeng Liu for making me feel so welcomed during my time in this department.

Last but not the least, I would like to thank my fiancee Liliana Jaramillo, I would have never been able to start this work without her infinite love and idyllic patience.

Abstract

Well motivated theoretical models predict the annihilation of dark matter (DM) into standard model particles, a phenomenon which could be a significant source of photons in the gamma-ray sky. With its unprecedented sensitivity and its broad energy range (20 MeV to more than 300 GeV) the main instrument on board the Fermi satellite, the Large Area Telescope (LAT), might be able to detect an indirect signature of DM annihilations. In this work we revisit several interesting claims of extended dark matter emission made from analyses of Fermi-LAT data: First, based on three years of Fermi Large Area Telescope (LAT) gamma-ray data of the Virgo cluster, evidence for an extended emission associated with dark matter pair annihilation in the $b\bar{b}$ channel has been reported by Han et al. (arxiv:1201.1003). After an in depth spatial and temporal analysis, we argue that the tentative evidence for a gamma-ray excess from the Virgo cluster is mainly due to the appearance of a population of previously unresolved gamma-ray point sources in the region of interest. These point sources are not part of the LAT second source catalogue (2FGL), but are found to be above the standard detection significance threshold when three or more years of LAT data is included.

Second, we confirm the detection of a spatially extended excess of 2-5 GeV gamma rays from the Galactic Center (GC), consistent with the emission expected from annihilating dark matter or an unresolved population of about 10^3 milisecond pulsars. However, there are significant uncertainties in the diffuse galactic background at the GC. We have performed a revaluation of these two models for the extended gamma ray source at the GC by accounting for the systematic uncertainties of the Galactic diffuse emission model. We also marginalize

over point source and diffuse background parameters in the region of interest. We show that the excess emission is significantly more extended than a point source. We find that the DM (or pulsars population) signal is larger than the systematic errors and therefore proceed to determine the sectors of parameter space that provide an acceptable fit to the data. We found that a population of order a 10^3 MSPs with parameters consistent with the average spectral shape of Fermi-LAT measured MSPs was able to fit the GC excess emission. For DM, we found that a pure $\tau^+\tau^-$ annihilation channel is not a good fit to the data. But a mixture of $\tau^+\tau^-$ and $b\bar{b}$ with a $\langle\sigma v\rangle$ of order the thermal relic value and a DM mass of around 20 to 60 GeV provides an adequate fit.

We also consider the possibility that the GeV excess is due to non-thermal bremsstrahlung produced by a population of electrons interacting with neutral gas in molecular clouds. The millisecond pulsars and dark matter alternatives have spatial templates well fitted by the square of a generalized Navarro-Frenk-White (NFW) profile with inner slope $\gamma = 1.2$. We model the third option with a 20-cm continuum emission Galactic Ridge template. A template based on the HESS residuals is shown to give similar results. The gamma-ray excess is found to be best fit by a combination of the generalized NFW squared template and a Galactic Ridge template. We also find the spectra of each template is not significantly affected in the combined fit and is consistent with previous single template fits. That is, the generalized NFW squared spectrum can be fit by either of order 10^3 unresolved MSPs or DM with mass around 30 GeV, a thermal cross section, and mainly annihilating to $b\bar{b}$ quarks. While the Galactic Ridge continues to have a spectrum consistent with a population of nonthermal electrons whose spectrum also provides a good fit to synchrotron emission measurements. We also show that the current DM fit may be hard to test, even with 10 years of Fermi-LAT data, especially if there is a mixture of DM and MSPs contributing to the signal, in which case the implied DM cross section will be suppressed.

Preface

The present work is based on the following papers, here listed in chronological order as appearing on the arxiv:

- Paper I: Macias et al. [2012]
- Paper II: Gordon & Macias [2013]
- Paper III: Macias & Gordon [2014]
- Proceeding I: Gordon & Macias [2014]
- Proceeding II: Gordon & Macias [2014]

While completing this work the candidate submitted another paper which was not included in this thesis:

- Paper IV: Macias et al. [2014]

During his PhD, the candidate has also been a member of the IceCube Collaboration for which he developed neutrino simulation software. This has resulted in the following publications

- M. G. Aartsen *et al.* [IceCube Collaboration], "Observation of High-Energy Astrophysical Neutrinos in Three Years of IceCube Data," [arXiv:1405.5303].
- M. G. Aartsen *et al.* [IceCube Collaboration], "Search for non-relativistic Magnetic Monopoles with IceCube," arXiv:1402.3460.
- M. G. Aartsen *et al.* [IceCube-PINGU Collaboration], "Letter of Intent: The Precision IceCube Next Generation Upgrade (PINGU)," arXiv:1401.2046.

- M. G. Aartsen *et al.* [IceCube Collaboration], "Search for neutrino-induced particle showers with IceCube-40," arXiv:1312.0104.
- M. G. Aartsen *et al.* [The IceCube Collaboration], "Search for a diffuse flux of astrophysical muon neutrinos with the IceCube 59-string configuration," arXiv:1311.7048.
- M. G. Aartsen, *et al.* [The IceCube Collaboration], "The IceProd Framework: Distributed Data Processing for the IceCube Neutrino Observatory," arXiv:1311.5904.
- M. G. Aartsen *et al.* [IceCube Collaboration], "Energy Reconstruction Methods in the IceCube Neutrino Telescope," arXiv:1311.4767.
- M. G. Aartsen *et al.* [IceCube Collaboration], "Probing the origin of cosmic-rays with extremely high energy neutrinos using the IceCube Observatory," arXiv:1310.5477.
- M. G. Aartsen *et al.* [IceCube Collaboration], "The IceCube Neutrino Observatory Part VI: Ice Properties, Reconstruction and Future Developments," arXiv:1309.7010.
- M. G. Aartsen *et al.* [IceCube Collaboration], "The IceCube Neutrino Observatory Part V: Neutrino Oscillations and Supernova Searches," arXiv:1309.7008.
- M. G. Aartsen *et al.* [IceCube Collaboration], "The IceCube Neutrino Observatory Part IV: Searches for Dark Matter and Exotic Particles," arXiv:1309.7007.
- M. G. Aartsen *et al.* [IceCube Collaboration], "The IceCube Neutrino Observatory Part III: Cosmic Rays," arXiv:1309.7006.
- M. G. Aartsen *et al.* [IceCube Collaboration], "The IceCube Neutrino Observatory Part II: Atmospheric and Diffuse UHE Neutrino Searches of All Flavors," arXiv:1309.7003.
- M. G. Aartsen *et al.* [The IceCube Collaboration], "The IceCube Neutrino Observatory Part I: Point Source Searches," arXiv:1309.6979.

- M. G. Aartsen *et al.* [The IceCube Collaboration],"Improvement in Fast Particle Track Reconstruction with Robust Statistics," arXiv:1308.5501.
- M. G. Aartsen *et al.* [The IceCube Collaboration],"An IceCube Search for Dark Matter Annihilation in nearby Galaxies and Galaxy Clusters," arXiv:1307.3473.
- M. G. Aartsen *et al.* [IceCube Collaboration],"Measurement of the cosmic ray energy spectrum with IceTop-73," Phys. Rev. D **88**, no. 4, 042004 (2013) [arXiv:1307.3795].

However, this work was not directly related to the thesis project and so are not discussed further here.

Contents

List of Figures

Chapter 1

Introduction

In the past decade, breakthroughs in cosmology have transformed our understanding of the Universe. A wide variety of observations now support a unified picture in which the known particles make up only one-fifth of the matter of the Universe, with the remaining four-fifths composed of dark matter. While other models such as modified gravity are unlikely to be able to explain the wealth of observations that are now available. However, the identity of this form of matter remains a mystery. Current constraints on dark matter properties show that the bulk of dark matter cannot be any of the known particles summarized in the standard model (SM) of particle physics. This first chapter briefly lists some of the most compelling observational evidence for DM. In addition, we mention some of best motivated DM candidates with an emphasis on the ways we could prove their existence.

1.1 Gravitational Evidence for the Existence of Dark Matter

1.1.1 Galaxies and Galaxy Clusters

The first indication for the existence of dark matter in the Universe was found by Fritz Zwicky in the 1930s [Zwicky, 1937]. He noticed that galaxies outside of the central cluster region move much faster than expected from the measured

gravitational potential of the visible mass. In order to reconcile this observation with the virial theorem, he postulated an additional form of matter that does not interact with light.

In the 1970s, Ford and Rubin Rubin & Ford [1970] confirmed earlier findings, but this time, at the scale of galaxies. They found that the radial velocities of stars and gas orbiting the centers of galaxies, rather than decreasing as a function of the distance from the gravitational centers, remain flat out to very large radii. Without any exception, all galaxies studied until now, including our own Galaxy, present flat rotation curves. Indeed, to explain the data, these gravitationally bound structures must be submerged in enormous halos of dark matter making up of order 90% of the total mass of galaxies and galaxy clusters.

1.1.2 Gravitational Lensing

According to General Relativity massive objects can bend light passing close to them. This effect − known as gravitational lensing − can be used to infer the existence of mass even when it emits no light [Refregier, 2003]. When observations of distant quasars and galaxies are made, there can appear multiple images of the distant objects, or the background object can look brighter when these images cannot be individually resolved. The Sloan Digital Sky Survey used statistical studies of lensed astrophysical objects (weak lensing) to conclude that galaxies, including ours, are more massive than it can be deduced from luminous matter. Again, the need for dark matter in galaxies is implied.

1.1.3 Cosmic Microwave Background

Probably the strongest evidence for dark matter comes from measurements on cosmological scales of temperature variations in the cosmic microwave background (CMB). This residual radiation from the hot early days of the universe underwent oscillations that froze in just before it decoupled from the neutrons and protons when the universe was $\sim$ 380000 years old. The angular scale and intensity of these oscillations allows us to fit cosmological parameters like the total energy density, the baryonic component and dark matter fraction. Figure 1.1 shows precision measurements made by Planck [Planck Collaboration et al., 2013] that are

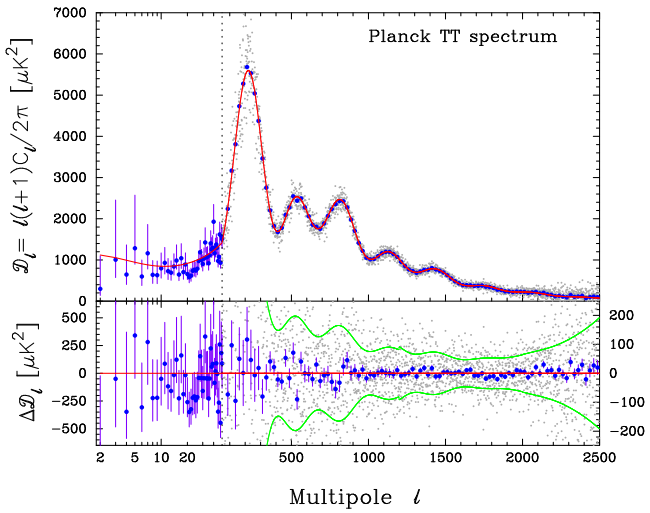

Figure 1.1: CMB angular power spectrum measured by Planck. Data is well fit by a six-parameter ΛCDM theoretical model. Figure from [Ade et al., 2014].

well fit by a six-parameter ΛCDM theoretical model. Furthermore, considering a global fit that also includes measurements of high-redshift supernovae [Perlmutter et al., 1999] and the large-scale distribution of galaxies [Peacock et al., 2001], it is obtained a cosmological model of the universe in which roughly 25% of its content consists of non-relatavistic matter, see for example [Suzuki et al., 2012]. Big bang nucleosynthesis (BBN) constrains the amount of baryonic matter to be about 5% of the total energy density and so DM is needed to make up the rest [Albornoz Vásquez et al., 2012].

Taken together all these observations, along with simulations of structure formation of the Universe, it can be deduced that particles constituting the cosmologically required dark matter had to be moving at low velocities (compared to the speed of light) at the epoch of structure formation in order to reproduce the observed structure of the Universe. We thus conclude that dark matter must be some type of non-baryonic particle which could have been either "cold" or possibly "warm" at the matter-radiation equality as well as possess a lifetime of order the age of the universe. Such weak constraints allows us to hypothesize many different dark matter candidates. In fact, the mass range and strength

of the interactions of these candidates can span many orders of magnitude. In this thesis we focus our attention on the ones that are best theoretically motivated and have the highest chances of being detected with current or near future technology: weakly interacting massive particles (WIMP).

1.2 WIMP dark matter

1.2.1 Theoretical Motivations for WIMPs

WIMPs are expected to have masses in the GeV−TeV energy range and can be naturally produced in the Big Bang with energy densities of the right order of magnitude required for dark matter [Bertone et al., 2005]. These particles are predicted by physics beyond the standard model (SM) theories that attempt to solve the "fine-tuning problem" of the SM − the Higgs boson mass in the SM is quadratically sensitive to the cutoff scale Λ of the SM effective theory via radiative corrections [Bertone et al., 2005]. In supersymmetry, the quadratic divergences in the Higgs mass due to top quark, gauge boson and Higgs loops are canceled by the top squark, gaugino and Higgsino loops, respectively. Although this is not the only theoretical framework that predicts the existence of WIMPs, this is perhaps the best motivated and studied model for new physics [Bertone et al., 2005].

Supersymmetric theories provide us with a prototypical WIMP particle: the lightest neutralino; a Majorana spin 1/2 fermion whose stability can be obtained if a discrete symmetry (R-parity) is introduced to avoid fast proton decay. It appears as a mixture of 4 superpartners (two Higgsinos and two gauginos). Detailed predictions for neutralino properties are highly dependent on the way the mix [Bertone et al., 2005]. However, our approach in this thesis is model independent, that is, we assume that WIMPs are neutral particles that are their own antiparticles, only undergo weak interactions and are long-lived. Alternatively, dark matter models have also been proposed in which dark matter is made of scalar particles [Boehm & Fayet, 2004].

1.2.2 Relic density of WIMP dark matter

If dark matter is made of WIMPs, their relic abundance in the Universe today can be calculated using basic statistical mechanics in the framework of the hot Big Bang [Chiu, 1966; Scherrer & Turner, 1986; Steigman, 1979; Zeldovich, 1965]. It is extremely remarkable that the results of such model-independent calculations are in close agreement with the actual measured abundance of cold dark matter today. Not only does this imply that the weak scale is an especially promising mass scale for dark matter candidates, but also, that cosmology alone is telling us that there should be new physics at the electroweak energy scale. This extraordinary fact is termed as the "WIMP miracle".

If a relic particle's interactions with ordinary matter are strong enough that it is coupled to the thermal bath in the hot, early universe, its number density as a function of time is governed by the Boltzmann equation as formulated for a Friedmann-Robertson-Walker (FRW) universe:

$$\frac{dn}{dt} = -3Hn - \langle \sigma v \rangle \left(n^2 - n_{\rm eq}^2 \right), \tag{1.1}$$

where H is the Hubble constant, n is the number density, $n_{\rm eq}$ is the equilibrium density, t represents the time and $\langle \sigma v \rangle$ is the thermally averaged WIMP annihilation cross section times relative velocity. The first term on the right represents a diminution of number density due to the expansion of the universe while the n^2 term arises from processes WIMP WIMP $\rightarrow$ SM SM that destroy WIMP particles, where SM denotes Standard Model particles, and the $n_{\rm eq}^2$ term arises from the reverse process SM SM $\rightarrow$ WIMP WIMP, which creates WIMP particles.

At early times, the WIMPs are assumed to be in thermal equilibrium, and their distribution is Maxwellian:

$$n_{\rm eq} = g \left(\frac{mT}{2\pi} \right)^{3/2} \exp\left(-\frac{m}{T} \right), \tag{1.2}$$

where T is temperature, m is the WIMP mass and g is the number of WIMP degrees of freedom (e.g. $g = 2$ for fermions). If the WIMP remained in thermal equilibrium, its number density would decrease exponentially with time. However, at freeze-out temperature $T \sim m/20$, the WIMPs ceased to annihilate and

dropped out of thermal equilibrium. Their number density at the present time is given by integrating the Boltzmann equation from freeze-out to the present time, and is

$$\Omega_{\rm WIMP}h^2 = \frac{mn}{\rho_c}h^2 \sim 0.11 \times \frac{2.8 \times 10^{26}\ {\rm cm}^3\ {\rm s}^{-1}}{\langle\sigma v\rangle}. \tag{1.3}$$

Thus, an evaluation of the thermally averaged neutralino annihilation cross-section is central to the evaluation of the relic density which must be of order $\Omega_{\rm WIMP}h^2 \sim 0.11$ to be in agreement with cosmological measurements.

1.3 Searches for WIMP dark matter

There are three different experimental programs that are currently underway trying to pin down the particle nature of dark matter: (i) Direct dark matter detection experiments look for signals produced in the elastic scattering of WIMPs from target nuclei adequately disposed in sensitive instruments. (ii) Linear collider searches aim to find WIMPs through their production in energetic SM particle collisions. (iii) Indirect detection experiments try to detect the products of WIMP pair-annihilations or decays occurring in astrophysical environments.

1.3.1 Direct dark matter detection

This search technique was first proposed by Goodman and Witten Goodman & Witten [1985] in 1985. They argued that the signature of WIMPs scattering in a certain medium might be directly detectable by sensitive instruments, provided that the WIMP interacts with ordinary matter with weak-scale cross sections. The standard value for the local WIMP density used for the interpretation of measurements is $\rho_{DM} = 0.3\,{\rm GeV/cm}^3$.

WIMPs are expected to interact with the atomic nuclei as they pass through our detectors and the nuclear recoil energy of the target particles can in principle be known. As it is a priori not known how WIMPs interact with the detector matter, two cases are typically considered. The first one is a spin-independent

(SI) scalar interaction with the WIMP-nucleus cross section given by

$$\sigma_{SI} = \sigma_n \frac{\mu_N^2}{\mu_n^2} \frac{(f_p Z + f_n(A-Z))^2}{f_n^2} = \sigma_n \frac{\mu_N^2}{\mu_n^2} A^2, \tag{1.4}$$

where σ_n is the scattering cross section on a nucleon, $\mu_{n,N}$ are the reduced masses of the WIMP-nucleon and WIMP-nucleus systems, respectively. The WIMP couplings $f_{p,n}$ to protons and neutrons are identical, leading to an A^2 dependence of the cross section. In the second case, spin-dependent (SD) axial vector couplings, the differential WIMP-nucleus cross section depends on the momentum transfer $\vec{q}$ and can be written as

$$\frac{d\sigma_{SD}}{\mathrm{d}|\vec{q}|^2} = \frac{8G_F^2}{\pi v^2} \left[a_p \langle S_p \rangle + a_n \langle S_n \rangle\right]^2 \frac{J+1}{J} \frac{S(|\vec{q}|)}{S(0)}. \tag{1.5}$$

$S(|\vec{q}|)$ is the spin-structure function, $a_{p,n}$ the couplings to protons and neutrons, and $\langle S_{p,n} \rangle$ are the expectation values of the total spin operators in the nucleus. In this case, no A^2 enhancement is present but the sensitivity depends crucially on the spin-structure of the particular target nucleus and on its total nuclear spin J, leading to a very different picture compared to the spin-independent case. For simplicity, spin-dependent results are usually reported assuming that WIMP couple to protons ($a_n = 0$) or neutrons only ($a_p = 0$).

The most important source of background for direct dark matter searches are neutron-induced nuclear recoil interactions as these cannot be distinguished from a WIMP signal. They are only different in event multiplicity – the WIMP-nucleus interaction cross section is expected to be extremely small, which means that WIMPs will always scatter only once in a detector. Neutrons, on the other hand, will often produce double-scatter signatures. Most of the backgrounds are suppressed by means of massive shields surrounding the detectors, either being made of high-Z materials such as lead and copper to reduce the neutron flux, or consisting of several meters of water. All dark matter detectors are placed in deep underground laboratories, with typically 1-2 km of rock overburden, suppressing the muon induced neutron flux by 5-7 orders of magnitude.

The current parameter space for spin-independent scattering cross sections obtained from direct WIMP searches is shown in Fig. 1.2. It is interesting that

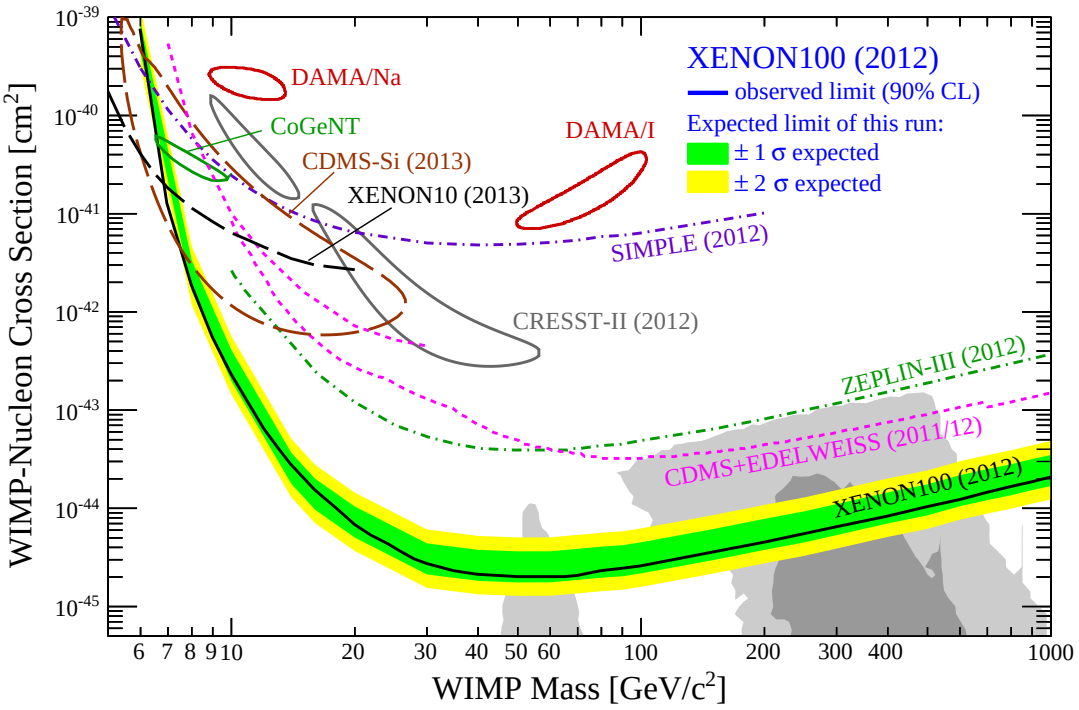

Figure 1.2: Experimental limits on spin-independent WIMP-nucleon scattering cross sections and dark matter detection claims. Several hints for WIMPs seen by CoGeNT Aalseth et al. [2013], CRESST-II Angloher et al. [2012], DAMA/Libra Bernabei et al. [2008], and CDMS-Si Agnese et al. [2013] (the 2σ regions are shown) are in stark tension by the upper limits reported by XENON100 Aprile et al. [2013], XENON10 Aprile et al. [2013], EDELWEISS Armengaud et al. [2011] and ZEPLIN-III Akimov et al. [2012]. Fig. from Schumann [2014].

over the past few years several hints for WIMP signals around masses of $10\,\mathrm{GeV}/c^2$ from several experiments have been reported. It is not clear whether all these positive hints are of common origin, maybe from WIMP interactions, or whether they are due to non-understood backgrounds. As can be seen in Fig. 1.2, the signal regions do not all overlap. However, several other experiments which do not see an excess impose strong upper limits that cover the full parameter space reported in the detection claims. Basically all positive signals are challenged by the null-result of the XENON100 collaboration.

1.3.2 Searches for dark matter at colliders

WIMPs could also leave a trace at the Large Hadron Collider (LHC) [Mitsou, 2013]. The method of detection of these particles is similar to that of neutrinos. At the LHC researchers look at the total energy and momentum budget of an event, as measured in all detector components, in order to indentify WIMP particles via a missing energy signal E_{miss}. In $p\bar{p}$-collisions, the initial longitudial momentum of the partons is unknown, hence they can only use the missing energy in the transversal plane, E^T_{miss} for the WIMP search.

The two general-purpose detectors at LHC, ATLAS and CMS [Mitsou, 2013], both provide almost 4π coverage around the interaction point and were designed to search for the Higgs particle, new physics, as well as for precision tests of the Standard Model. Astrophysical uncertainties are completely absent in collider results, however, the very limited time a particle spends in the detector will make it almost impossible to proof from collider data alone, that a detected candidate is the dark matter particle.

As pair-production of WIMPs of the type

$$q\overline{q} \rightarrow \chi\overline{\chi}, \tag{1.6}$$

are invisible to the detectors, the most generic approach to search for WIMPs at the LHC is to search for pair-production associated with initial (or final) state radiation

$$q\overline{q} \rightarrow \chi\overline{\chi} + X, \tag{1.7}$$

with X being a γ, Z- or W-boson, or a gluon. The unknown coupling of WIMPs (χ) to standard model fermions (q) can be described in a largely model-independent fashion using effective field theories and contact operators. Depending on the choice of the operators, the interaction is similar to direct (spin-independent, spin-dependent) or indirect searches (s-wave and p-wave annihilation). The initial state radiation leads to an imbalance in the detected energy and momentum, and the WIMP search is based on events with a high E^T_{miss} plus a single particle track or jet. The searches are therefore also referred to as monophoton, mono-Z, mono-W and monojet searches.

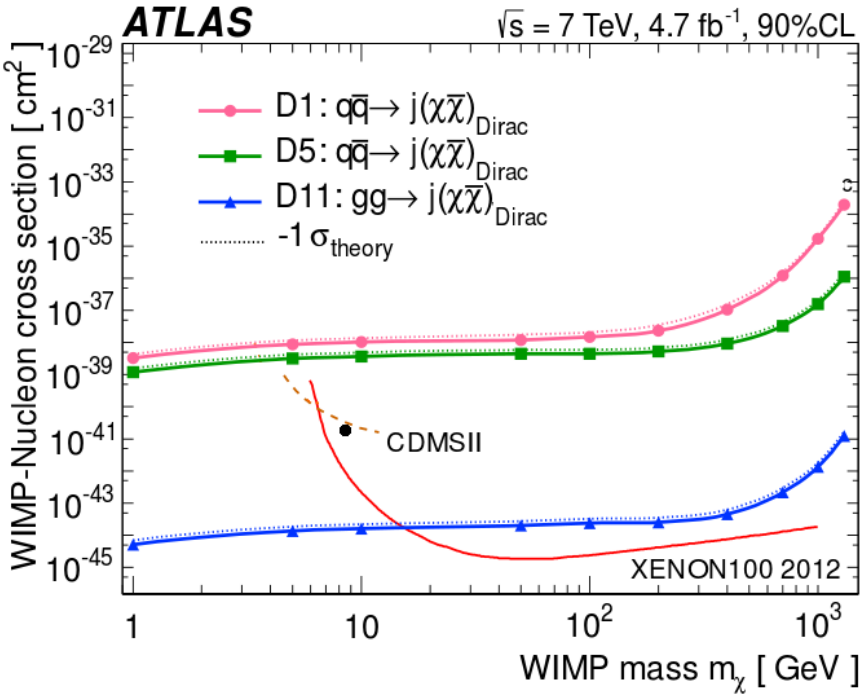

Figure 1.3: Constraints on the spin-independent (Dirac fermion) WIMP-nucleon scattering cross section from a monojet search of ATLAS Aad et al. [2013]. No excess of events was found above the background expectation and the lines labeled with D1, D5, D11 correspond to 90% CL upper limits for different effective interaction operators. For comparison, the direct detection limits from CMDS-II and XENON100 are also shown, as well as the point with the highest likelihood from the CDMS-Si signal claim Agnese et al. [2013] (black point). Figure from Schumann [2014].

An example of a result from a monojet search with ATLAS is shown in Fig. 1.3, using LHC data with a center-of-mass energy of $\sqrt{s} = 7\,\text{TeV}$ and an integrated luminosity of $4.7\,\text{fb}^{-1}$ Aad et al. [2013]. The event selection criteria usually require $E^T_{\text{miss}} \approx 120 \ldots 500\,\text{GeV}$, a well-reconstructed jet with a transverse momentum $p_T > 110\,\text{GeV}$, and no additional lepton or jet. Z-boson production together with a jet, with the Z decaying into two neutrinos, is the main Standard Model background for this search, which is determined by data-driven methods. As no excess of events above the Standard Model expectation has been been found, the experiment could set upper limits on the WIMP-nucleon scattering cross section. Besides the choice of a cut-off scale Λ, the results are model independent in the

sense that the only assumption entering the analysis is that no other particles can be directly produced in the $p\bar{p}$-collision.

1.3.3 Indirect Detection of WIMP dark matter

The most interesting WIMP by-products are gamma-rays [Bergstrom et al., 1998], neutrinos and antimatter. A "smoking gun" signature would be the detection of monoenergetic high-energy photons from WIMP self-annihilation − this is known in the literature as a gamma-ray line. However, WIMP self-annihilation can also lead to quarks, leptons, gauge bosons and gluons, which in turn hadronize into various mesons and baryons. When neutral pions are created they decay almost immediately and yield continuous gamma-ray emission. Unfortunately this type of signature is much harder to single out as common astrophysical objects produce similar spectral patterns, however, distinctive characteristics appear for $E_\gamma < m_\chi$, so that given enough signal rate, an energy cut-off depending on m_χ might be detected [Bertone et al., 2005].

Unlike WIMP gamma-ray and neutrino signals that would point back to the sources, cosmic-rays diffusing out of their generations sites would interact with the random magnetic fields in the Galaxy hiding their original directions. The cleanest cosmic ray signal that could be obtained is likely to be antimatter, which is produced in roughly equal proportions in DM annihilation, but subdominant in usual cosmic ray sources.

The expected flux of secondaries resulting from WIMP self-annihilations scales with the square of the dark matter density along the line of sight to the source. This thus implies that the most promising search targets are regions with large dark matter over-densities and low background. A limited list of indirect dark matter targets are: the Galactic Center, Galactic halo region, dwarf galaxies of the Milky Way, and nearby galaxy clusters [Bertone et al., 2005].

This thesis focuses on identifying gamma-ray signals from dark matter annihilation. The Galactic center is expected to be the brightest source of DM annihilations in the gamma-ray sky. However, this is a very crowded region containing many gamma-ray sources which makes it very difficult to disentangle a tentative dark matter signal. Instead, dwarf galaxies are dark matter dominated

Table 1.1: List of indirect detection experiments.

Experiment	Target	Location	Energy Sensitivity	Technology
Fermi	Photons, e^+/e^-	Satellite	∼20 MeV − 300 GeV	Pair Conversion Telescope and Calorimeter
HESS	Photons, e^-	Namibia	∼100 GeV − ∼15 TeV	Atmospheric Cherenkov Telescope
VERITAS	Photons, e^+/e^-	Arizona, USA	∼100 GeV − ∼10 TeV	Atmospheric Cherenkov Telescope
INTEGRAL	Photons	Satellite	15 keV − 10 MeV	Spectrometer
MAGIC	Photons, e^+/e^-	La Palma	∼100 GeV − ∼10 TeV	Atmospheric Cherenkov Telescope
PAMELA	e^+/e^-	Satellite	50 MeV − 270 GeV (for antimatter)	Pair Conversion Telescope
AMS	e^+/e^-, anti-nuclei	International space station	50 MeV − 1 TeV (for antimatter)	Magnet Spectrometer
IceCube/ DeepCore	Neutrinos	Antarctica	$\sim 10^{11}$ eV − 10^{21} eV	Ice Cherenkov Telescope

objects with very limited backgrounds. Also, since they are predominantly found at high galactic latitudes, the astrophysical foregrounds are comparatively weak. Unfortunately the photon statistics are very low too.

1.3.4 The Fermi-LAT detector

High energy gamma-ray signals can be searched for with the Fermi satellite and ground based air Cherenkov telescopes, see Tab. 1.1 for a brief description of currently operational experiments. The Large Area Telescope (LAT) [Atwood et al., 2009], is a modular pair-conversion gamma-ray detector. It consists of a 4×4 array of identical towers of area 40×40 cm^2 each. These towers are composed of a tracker, a calorimeter, and a data acquisition system. The modules are surrounded by tiled plastic scintillators that serve as charged-particle filters. The

calorimeter contributes significantly to background rejection. The flux of celestial gamma rays is several orders of magnitude smaller than that of cosmic rays at the orbit of Fermi and the design of the LAT and the data processing undertaken in ground enables very efficient rejection of this background. The LAT is sensitive to gamma rays from 20 MeV to greater than 300 GeV with ∼10% resolution over much of that range [Ackermann et al., 2012b]. The effective area peaks at ∼10 GeV and the field of view is 2.4 sr. The angular resolution ranges from several degrees at 100 MeV to ∼0.1 deg at the highest energies. The scanning and rocking pattern of Fermi allows the LAT to observe the entire sky every 3 hours.

1.3.5 Astrophysical Backgrounds

The main sources of uncertainties in our dark matter analyses are: extragalactic diffuse gamma-rays, diffuse Galactic gamma-rays, unresolved gamma-ray point sources and charged cosmic ray particles hitting the Fermi-LAT detector. Of particular interest to us is the Galactic gamma-ray diffuse emission in the innermost part of the Galactic center. In the following chapters we will make a quantitative treatment of their inherent systematic uncertainties using both an empirical approach and a parametric method with the GALPROP software.

1.3.5.1 Diffuse Galactic gamma-rays

The Galactic diffuse emission is several orders of magnitude higher than any other component measured by Fermi-LAT. About 60% of the photons detected by the LAT come from CR particle interactions with gas in the interstellar medium and the interstellar radiation field [The Fermi-LAT Collaboration, 2012]. The main components originating the diffuse emission in the Milky Way are π^0-decay, inverse Compton and bremsstrahlung.

The Fermi team produced a spatial and spectral template model[1] which is recommended for most analyses of LAT data. This model was constructed as a linear combination of gas column densities and an inverse Compton (IC) intensity map as a function of energy. Gas column densities are determined from spectral

[1] http://fermi.gsfc.nasa.gov/ssc/data/access/lat/BackgroundModels.html

line surveys of HI− extracted from radio data using a uniform value for the spin temperature of 200 K − and CO−a tracer of molecular hydrogen−. They also accounted for gas not traced by the lines with optical depth maps of dust.

1.3.5.2 Diffuse Extragalactic gamma-ray background

The extragalactic gamma-ray background is a nearly isotropic component that is difficult to separate from the dominant Galactic foreground [The Fermi-LAT Collaboration, 2012]. As such, its spectrum depends on the model adopted for the Galactic diffuse emission, which is itself uncertain. Charged cosmic ray particles like protons, electrons and positrons, as well as a number Earth albedo photons, present a difficult instrumental background to potential DM signals, especially for gamma-ray lines. The Fermi collaboration provided a template obtained from a fit to the data taken from the region $\mid b \mid < 30^{\circ}$ which also accounts for the effects of charged particles hitting the detector. This template map depends on the filters applied to the measured photons and our knowledge of the instrument response function. Diffuse Extragalactic gamma-ray background is generally only a very small contribution to the areas of study in this thesis.

Chapter 2

Evaluating the Gamma-Ray Evidence for Self-Annihilating Dark Matter from Clusters of Galaxies

2.1 Introduction

Galaxy clusters are the largest massive objects in the Universe and they are promising astrophysical targets to study the hypothetical annihilation radiation Pinzke et al. [2009]. Compared to smaller objects, like dwarf spheroidal galaxies, clusters possess DM substructures or subhalos which are less affected by tidal stripping, and the uncertainties related with the DM density profiles are usually lower. More importantly, it has also been shown that the presence of subhalos in clusters can considerably enhance the DM luminosities Gao et al. [2012]; Pinzke et al. [2011]. On the downside, the gamma-ray foreground of clusters may be contaminated with point sources such as active galactic nuclei (AGN) and star-burst Acciari et al. [2009]; Acero [2009] galaxies. Also, there could be a significant contribution of gamma-rays from cosmic rays (CRs) in clusters, see for example Pinzke et al. [2011]. Consequently, the task of disentangling a DM signal in the continuum spectrum from the astrophysical noise in galaxy clusters

may be difficult Jeltema et al. [2009]; Pinzke & Pfrommer [2010].

Through the use of dedicated cosmological simulations of cluster halos and subhalos from the Phoenix Project Gao et al. [2012] and by making some reasonable theoretical assumptions Pinzke et al. [2011], accurate extended dark matter density profiles have been reported Gao et al. [2012]. In Pinzke et al. [2011] it was found that resolved and unresolved substructures in the inner part of clusters are expected to play a more important role than that of the main smooth Navarro-Frenk-White (NFW) halo. From this it follows that nearby clusters should be the brightest DM radiative sources after the milky way (MW) in the gamma-ray sky. In fact, in Pinzke et al. [2011], Fornax, M49 and Virgo are found to yield the most intense pair-annihilation radiation as a result of the enhancement provided by their subhalos.

From the analysis of the first 11 months of publicly available Fermi-LAT data and adopting a smooth NFW density profile, null DM results, from clusters, were obtained Ackermann et al. [2010]; Dugger et al. [2010]. Instead, constraints on cross sections and masses of WIMPs were derived. It was also the case for the work shown in Huang et al. [2012] where, however, an extended DM halo profile (different to the one shown in Gao et al. [2012]) and almost 3 years of Fermi data were employed.

An interesting study of the Virgo cluster by Han et al. Han et al. [2012a] (HFEGW hereafter) which used a high resolution DM density profile Gao et al. [2012] was recently undertaken. They claimed to have found some evidence for DM annihilation from Virgo in the $b\bar{b}$ channel for a WIMP mass of about 28 GeV and with a detection significance of 4.4σ. They found that their signal is from a spatially extended region which is also spectrally distinct from the the radio galaxy (M87) located in the center of the region of interest (ROI). They also found that the target region prefers a DM hypothesis over a CR model. HFEGW used the 2FGL catalogue to determine the list of gamma-ray point sources used in their astrophysical model. We reproduce in Fig. 2.1 the main results shown in HFEGW for the No-CR model where we make use of their same data set and assumptions. The test statistic (TS) is defined as in Nolan [2012]

$$TS = 2\left[\log \mathcal{L}(\text{new source}) - \log \mathcal{L}(\text{NO-new source})\right], \tag{2.1}$$

where $\mathcal{L}$ stands for the maximum of the likelihood of the data given the model with or without the new source at a certain location of the ROI. In the large sample limit, under the no source hypothesis, TS has a $\chi^2/2$ distribution with the number of degrees of freedom equal to the number of parameters associated with the proposed positive amplitude new source Mattox et al. [1996]; Wilks [1938]. As, in the current case, only one degree of freedom (the cross-section) is required by the DM, the TS values in Fig. 2.1 are approximately equal to the square of the number of standard deviations of a DM detection. Further details on our analysis are given in the next section.

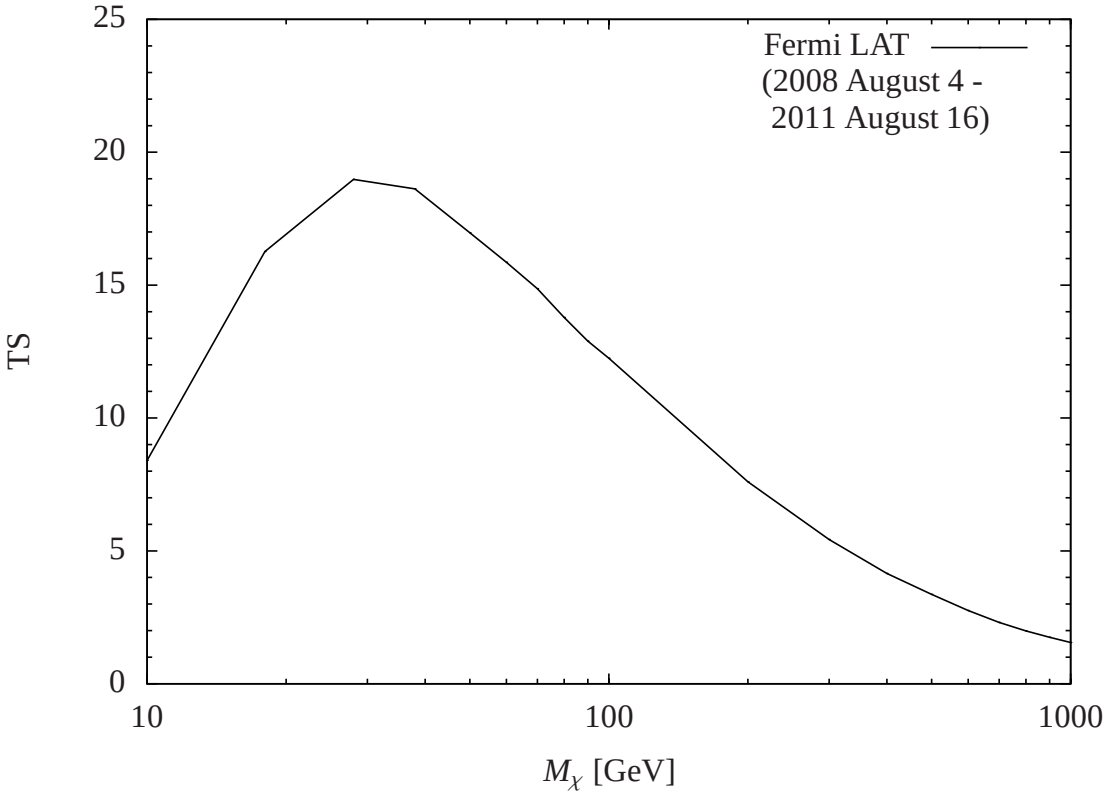

Figure 2.1: TS values obtained for the Virgo cluster with an extended dark matter density profile plus the 2FGL catalogue point sources and backgrounds. Dark matter annihilation is assumed to be in the $b\bar{b}$ channel. The CR component is assumed negligible. The fit is based on roughly 3 years of Fermi LAT data. See Han et al. [2012a] for details.

The 2FGL catalogue is fundamentally a catalogue of significant gamma-ray

point sources detected by the LAT in the first 24-months of operation Nolan [2012]. The method employed by the Fermi Collaboration to construct the 2FGL catalogue consists of three analysis steps; source detection, localization (position refinement), and significance estimation. Transient sources were not considered.

After applying the method outlined above, the collaboration considered a spatially unresolved gamma-ray source as part of the 2FGL catalogue if its test statistic TS exceeds 25, or equivalently (as there are four new degrees of freedom), if its significance detection was larger than 4.1σ. Generally speaking, it might occur that sources that were just on the threshold for the 2-year data set, become significant for larger LAT data samples. For example, after two years of LAT observations, Pictor A had a test statistic value of 20, however, after three years of LAT observations, Pictor A was found to have a TS value of 33 Brown & Adams [2012] . It is important to note that when using extended dark matter profiles, new gamma-ray sources not taken into account in the model can mimic a DM signal. Here, we show that indeed the emission from weak gamma-ray point sources, that were not included in the 2FGL catalogue, were a significant contaminant to the flux interpreted as continuous gamma-ray emission in HFEGW.

2.2 Analysis and Methods

In order to compute the effect that weak point sources (which were not included in the 2FGL catalogue) have on the analysis presented in HFEGW, we considered three different periods of Fermi data: 2 years, 3 years and 3.8 years of nominal all-sky survey data. The filters applied to the data sets, the instrument response function utilized, background models and properties of the Virgo cluster assumed are the same as those adopted in HFEGW. We refer the reader to that study for details.

To check for new point sources in the ROI we do not assume the extended DM template as part of the model. A brief description of the method used is outlined in Sec. 2.2.1. In Sec. 2.2.2 we illustrate the spatial and spectral agreement of the new proposed background with the observations and we then recheck for the claimed continuous DM self-annihilation in Sec. 2.2.3.

2.2.1 Determination of missing gamma-ray point sources

Using a binned likelihood technique Mattox et al. [1996], we performed an analysis of the Fermi-LAT spectrum over three different periods of time: (2008 August 4 through 2010 August 4), (2008 August 4 through 2011 August 16) and (2008 August 4 through 2012 June 26). The normalization and index for all the point sources from the 2FGL catalogue that fell within 10° of the center of the core of M87 were left free in the fit. The spectral parameters of sources which were within 5° of the ROI perimeter were fixed to their catalogue values.

From the resulting best-fit we construct a residual TS map for each of the three data sets over a grid of 19600 points in a $14° \times 14°$ squared region centered at M87. For each given point of the grid we add sequentially a new point source with a conventional spectral definition Nolan [2012], and maximize the likelihood as a function of its flux. This step was realized using the Fermi Science Tool[1] (version v9r27p1) `gttsmap` and the resulting array of TS values is shown in Fig. 3.1. To estimate the position of the new sources, we take into consideration a list of sets of adjacent pixels which satisfy the condition $TS > 10$. For every set of pixels, the coordinates of its centroid were computed as an average of the pixel positions weighted by their respective TS values. All of the candidate sources which are sufficiently isolated under visual inspection are then passed to the significance and thresholding step in this iterative process.

In order to get the significances of the possible new point sources, we assumed their spectrum was described by a simple power-law, then a binned `pyLikelihood`[1] routine with an energy binning to 25 bins was run. We made no distinction between *Front* and *Back* events. The Fermi collaboration stipulated that sources with a $TS > 25$ should be included in the catalogue of gamma-ray point sources Nolan [2012]. Those sources that survived this threshold analysis were then passed onto the next step which consisted of a position refinement. Finding the best position for the candidate sources is accomplished with the Fermi Science Tool `gtfindsrc`[1]. By using an unbinned analysis technique, this tool seeks the highest TS value for different positions around our initial value based on an analysis of groups pixels. We also estimate the uncertainties in the source positions in

[1] http://fermi.gsfc.nasa.gov/ssc/data/analysis/documentation/Cicerone/

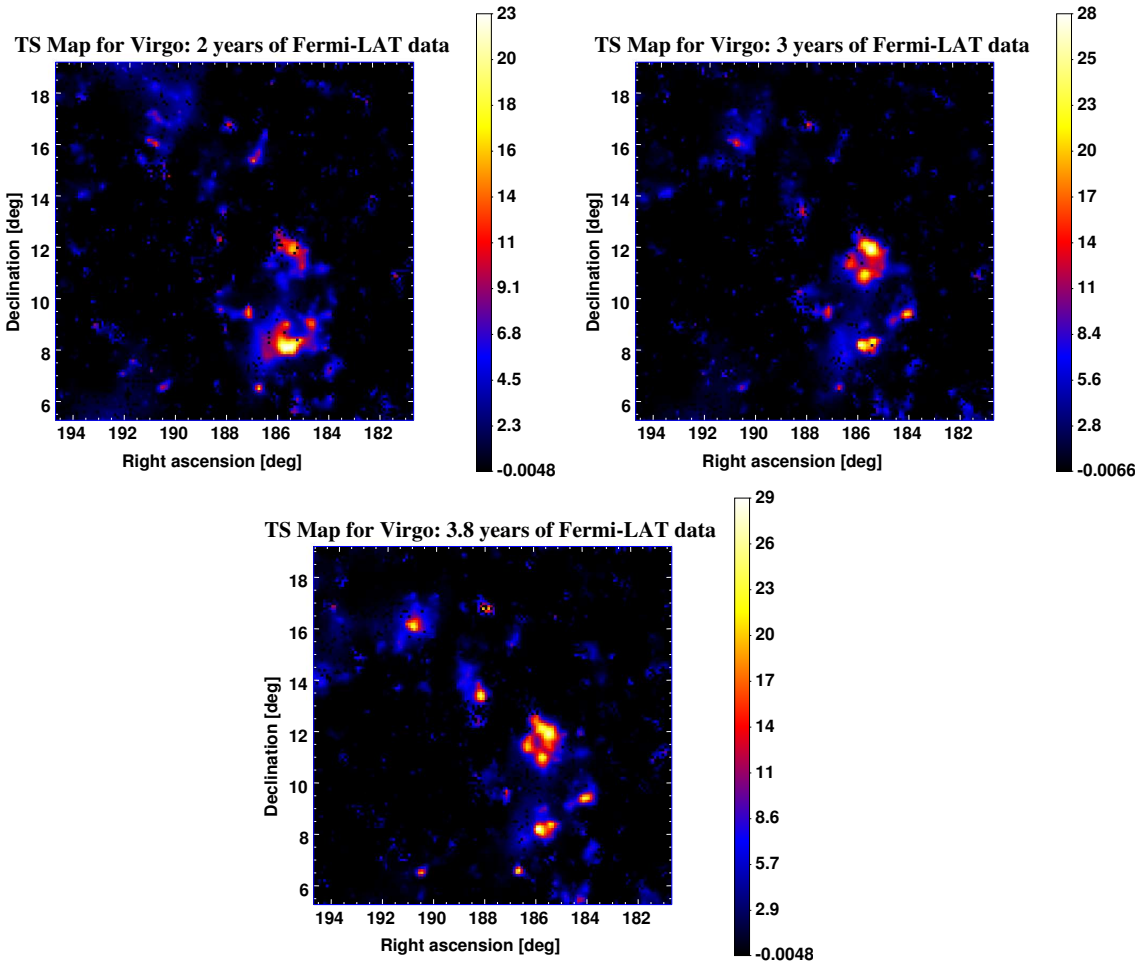

Figure 2.2: TS maps for three different periods of Fermi data of the Virgo cluster. The maps span a $14° \times 14°$ region of the sky which is centered at the coordinates of M87. The extent of every pixel is $0.1° \times 0.1°$.

this step.

We did not find evidence for new point sources with a $TS > 25$ for the 2 years data set Nolan [2012]. However the significance for some weak source candidates was appreciably enhanced when more LAT data was included. The results are shown in Table 3.1.

2.2.2 Quality of the background fit

Since there is sufficient evidence for a group of new gamma-ray sources in the Virgo cluster, we included these sources in our background model and evaluated the agreement with the LAT data. A new fit to the observations for the data period of 3.8 years was made where the normalizations of the galactic and isotropic backgrounds were left free, as well as, the spectral shape and normalizations for all point sources that fell within a squared region of $14° \times 14°$ centered at the M87 position.

In Figures 4.3 and 2.4 we illustrate the spatial and spectral quality of the fit. The spatial residual map is scaled to the Poisson noise and the pixel size was resampled from their original size of $0.1° \times 0.1°$ to avoid statistical fluctuations. It is consistent with random noise and contains no noticeable spatial features. The spectrum in Figure 2.4 is a good fit without any noticeable patterns in the residuals. As can be seen, the new point sources have a greater contribution to the overall fit than many of the ones already included in the 2FGL catalogue. Thus the background model we have found is a better representation of the gamma-ray sky in the Virgo region and should therefore be used as the background template in any studies in this region Huang et al. [2012].

2.2.3 The effect of unresolved point sources on the significance of the DM annihilation signal

The significance of a DM annihilation signal is examined using three alternative case scenarios for the background model: (i) a model following the approach taken in HFEGW for the NO-CR model; (ii) a model including the seven sources shown in the top part of Table 3.1 with $TS \gtrsim 25$, plus the 2FGL sources and

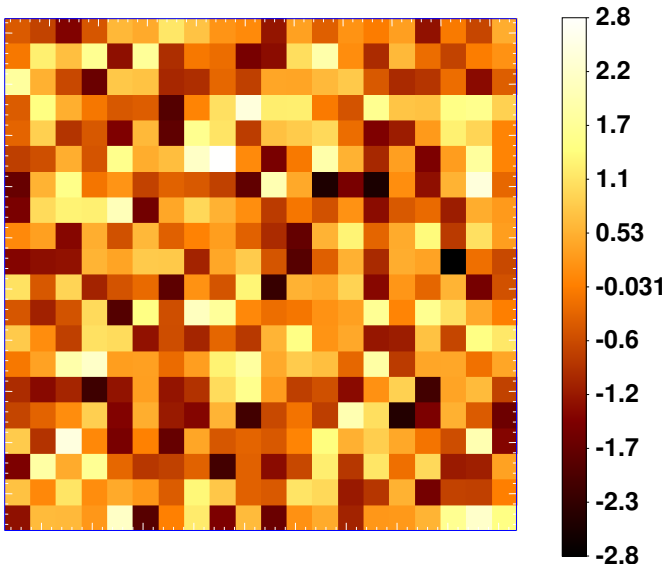

Figure 2.3: The spatial residual map shows (data − BG model)/$\sqrt{\text{BG model}}$ in σ units, where the background (BG) model includes the 2FGL catalogue sources plus the new point sources discovered in the ROI (here conservatively we consider all sources shown in Tab. 3.1). The pixel size was rescaled to $0.5° \times 0.5°$ and the map spans a $10° \times 10°$ centered at the cluster position. Counts are summed over the full energy range of 100 MeV−100 GeV for the 3.8 years of Fermi-data.

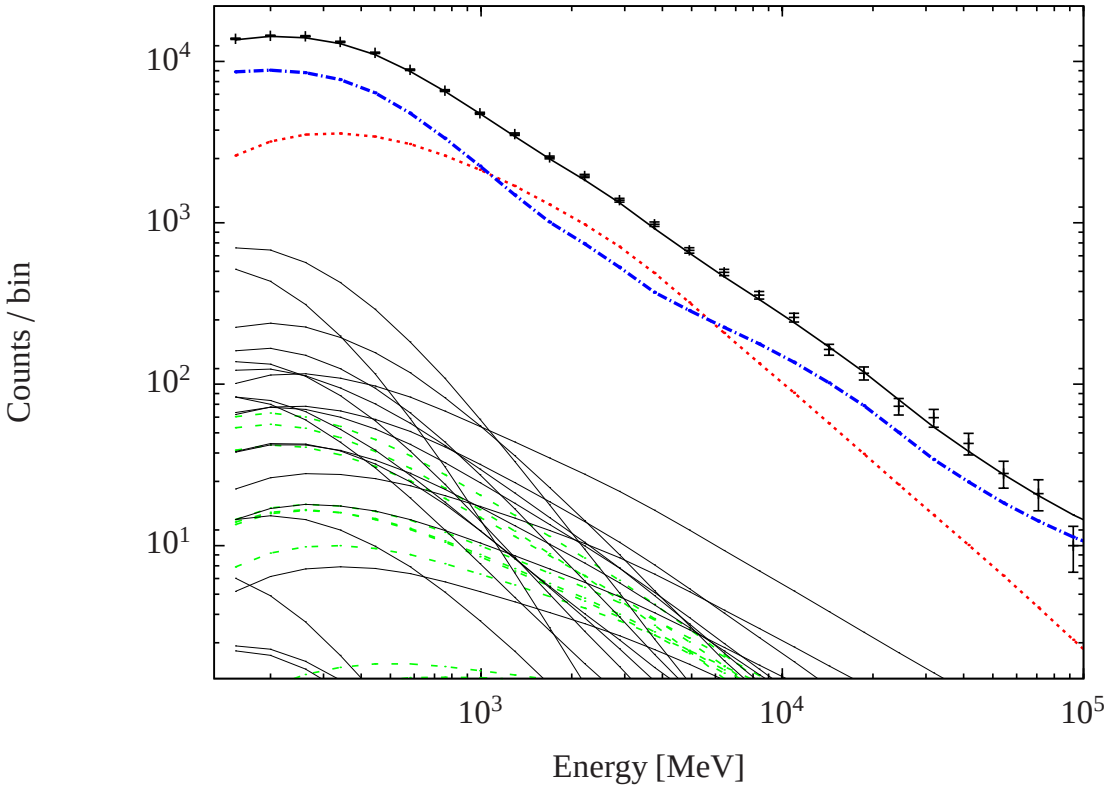

Figure 2.4: Fit to the spectrum of the BG model. Red (dotted) and blue (dash-dotted) lines correspond to Galactic and isotropic extragalactic background respectively. The green dashed lines show the contribution of the new point sources and the black lines stand for the 2FGL catalogue point sources. Counts are read from a Fermi-data period of 3.8 years in the full energy range of 100 MeV−100 GeV.

diffuse backgrounds; (iii) a model conservatively including all the new sources from Table 3.1 plus the 2FGL sources and diffuse backgrounds.

We use the high resolution extended DM halo profile obtained in Gao et al. [2012] and model the WIMP spectrum with the `DMFit` package Jeltema & Profumo [2008] as implemented in the `Science Tools` analysis software. Since our case study is the self-annihilation of WIMP particles in the $b\bar{b}$ channel we do not take into account Inverse Compton (IC) effects. There is also the issue of whether it is possible to successfully account for the significant point source at the center of Virgo (M87). HFEGW found that their DM signal was spatially extended and so concluded that it could not be due to the M87 point source. We also checked that M87 did not have a significantly curved or time-varying spectrum and found no vidence of extended emission from M87 using the 3.8-year data set Nolan [2012]. Based on these checks, we model M87 as a point-source with a power-law spectrum. Any deviation from this may erroneously enhance an apparent DM signal, but given we find that the addition of the new point sources makes the apparent DM signal not significant, this is unlikely to be an important factor for our study.

A new fit to the LAT data period of 3.8 years corresponding to the NO-CR model (see HFEGW for details) is shown in Fig. 2.5. Interestingly, we note that if only the 2FGL sources plus galactic and extragalactic backgrounds are included (case (i)), the significance detection for extended DM radiation exceeds 5σ. However, and the main point of this paper, all significant point sources must be included in the background model for such studies. Indeed when we included in the template model the seven new point sources with $TS \gtrsim 25$ Table 3.1 (case(ii)) the significance of detection decreased substantially to 3.6σ. And for case (iii) when we included all of the new point sources found with TS-values larger than 15 the significance of detection decreased to 3.0σ. Here we should also stress that if a detailed CR component is added to the model, the significance of detection for DM would decrease further.

As can be seen in Fig. 3.1, the data favor additional localized point sources rather than a more diffuse signal that would be expected from annihilating DM. In introducing seven new point sources we should however consider that we are introducing 28 new parameters (seven times the positions, the amplitudes and the

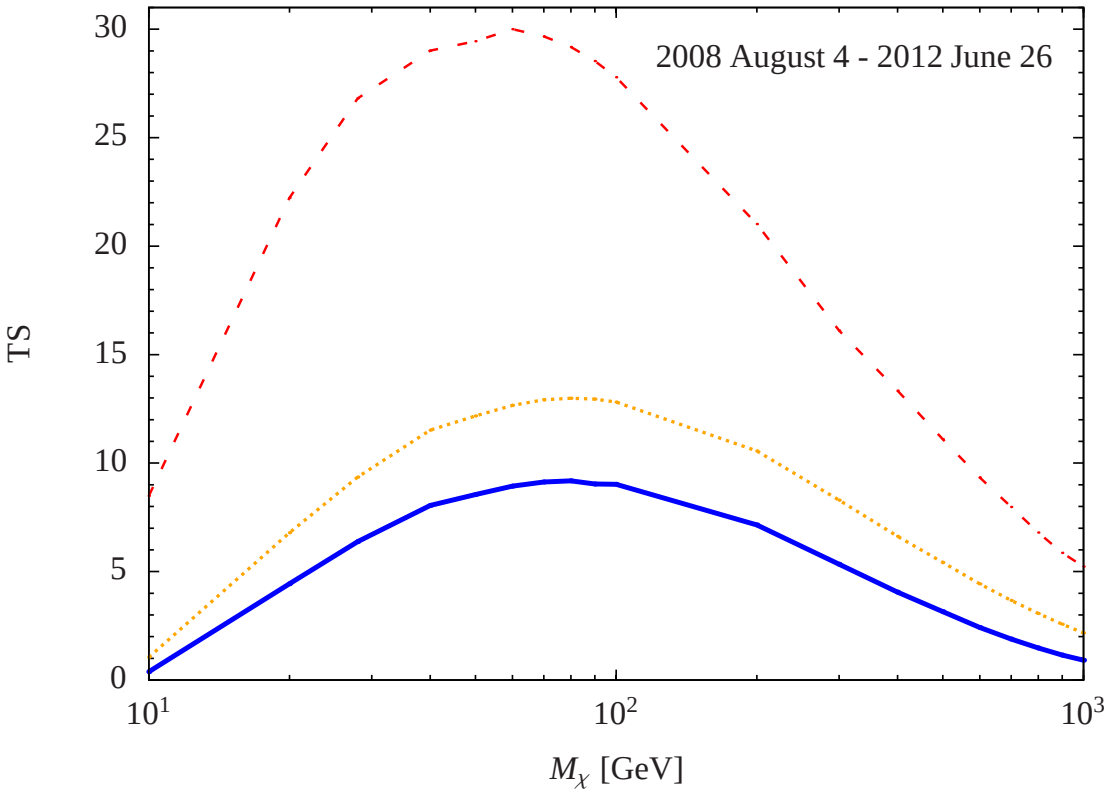

Figure 2.5: TS values for DM radiation in the $b\bar{b}$ channel, an extended DM density profile and source class of Fermi-LAT data taken between 2008 August 4 and 2012 June 26. The fit is made by considering three distinct background models. The red dashed line is obtained by assuming the same background model used in HFEGW. For the yellow (dotted) and blue (solid) lines shown, the fit is obtained by using a modified background which considers 7 additional new point sources, and 9 additional point sources respectively (see text).

spectral indices), while adding DM corresponds to only two new parameters (the cross-section and the mass). We can statistically compare the two alternatives by evaluating the p-values for each case using Wilks' theorem Mattox et al. [1996]; Wilks [1938]. As the p-values are quite small we can convert to "σ's of detection" by comparing the p-values to the one parameter case. The TS for including seven new point sources is 192 which corresponds to a 11 σ detection. While the TS for including DM with no new point sources corresponds to a TS of 28.9 which for two degrees of freedom is only a 5 σ detection. So clearly the 7 new point source case is a much better fit to the data despite requiring more parameters.

We found that the new point sources did not have significant curvature in their spectrum or time variation on a monthly scale Nolan [2012]. There are detections of point sources at other wavelengths in areas consistent with the positions we found for the new point sources. It would be interesting in future work to evaluate statistically whether they can be associated with the new point sources, as was done for the 2FGL point sources Nolan [2012], but it is beyond the scope of the current study.

As the observing time increases, it is expected that more astrophysical point sources will in general be found as the signal to noise is increasing. However, it would not be valid to extrapolate the number of new point sources we have detected in the Virgo cluster to other areas of the sky. It should be noted the it was only the Virgo cluster that HFEGW found a significant signal excess despite checking several other clusters. Also, clusters in general will be expected to have a greater number of point sources compared to random areas of the sky.

2.3 Conclusions

We have investigated whether there is evidence for extended emission from DM annihilation in the Virgo cluster. We have focussed particularly on the results found by HFEGW. There, using three years of LAT data, they found, assuming a negligible CR contribution, there was a 4σ detection of a CDM component annihilating to the $b\bar{b}$ channel. They found a somewhat weaker significance for the $\mu^+\mu^-$ case. Also, they found that including fitting for a CR component reduced the $b\bar{b}$ case significance to 3σ. We have focussed on their most significant

case to highlight the effects of unresolved point sources. Crucially, they used the point source catalogue derived from two years of LAT data. But, we have found the extra data now means that point sources which were below the TS=25 threshold in the 2-year data, are above it in the 3-year data. Such point sources should be included in the background template for studies using the 3-year data set.

We redid the HFEGW analysis with 3.8 (rather than 3) years of LAT data and found that the HFEGW result went up to a 5σ detection for DM annihilating into the $b\bar{b}$ channel (with negligible CRs assumed) if the 2FGL catalogue is still used to construct the background template. But, if we included the seven new point sources with $TS \gtrsim 25$ for the four year data, we found the DM signal is only significant at the 3σ level, and this will go down further if the CRs are fitted for rather than assumed negligible. Therefore, we have shown that the HFEGW result was significantly affected by unresolved point sources. This highlights that when using the LAT data, it is important to check for new point sources if one is using more data than was used in deriving the most recent point source catalogue.

Shortly after the article by Macias et al. [2012] (on which this chapter is based) was placed on the arXiv, a revised version of HFEGW was uploaded, with an extended set of authors Han et al. [2012b]. Their new conclusions were consistent with ours. There were some small differences in the number and positions of the new point sources found which is likely due to the slightly different algorithms used for point source detection and the area for which new sources were searched for. However, as in this paper, the conclusion was that the continuous gamma-ray signal, interpreted as evidence for DM in HFEGW, was in fact due to unresolved point sources.

Right Asc. [deg]	Dec. [deg]	95% error radius [deg]	TS
190.92	16.21	0.07	31.47
187.91	16.88	0.09	24.90
188.18	13.56	0.11	41.92
185.85	8.30	0.05	30.92
186.68	6.68	0.04	25.40
185.48	12.04	0.11	26.18
184.12	9.48	0.06	24.61
185.74	11.06	0.09	18.25
187.15	9.71	0.09	15.18

Table 2.1: New point source candidates found in the Virgo cluster for 3.8 years of Fermi-LAT data. We show in the top part of the table seven new point sources which satisfy all the requirements to be included in upcoming catalogues. In the bottom part of the table an additional two sources that do not quite satisfy the thresholding condition are also shown.

Chapter 3

Dark Matter and Pulsar Model Constraints from Galactic Center Fermi-LAT Gamma Ray Observations

3.1 Introduction

The central region of the Milky Way is expected to be the brightest source of dark matter annihilation gamma-rays by at least two orders of magnitude. However, the Galactic Center (GC) region also contains a large number of bright astrophysical sources. In particular, the interaction of energetic cosmic rays with the interstellar gas constitutes the main source of Galactic diffuse emission. Unfortunately, there is significant uncertainty about the propagation and origin of these cosmic rays, the distribution of the magnetic fields, radiation fields and the interstellar medium. In addition, due to the relatively low angular resolution of the LAT instrument ($\sim 0.2^{\circ}$ at 10 GeV), several undetected point-like gamma ray sources could mimic diffuse gamma ray emission, consequently, the task of disentangling a tentative DM signal from the astrophysical background necessarily implies the implementation of detailed techniques to account for the uncertainties of the Galactic diffuse emission model.

The GC hosts a supermassive black hole with a mass of $\sim 4 \times 10^6 M_\odot$, called Sagittarius A* (Sgr A*). With the Fermi-LAT resolution, it can be modeled as point source with curved spectral shape Nolan [2012]. The interesting analysis performed in [Linden et al., 2012a] points out that the upcoming Cherenkov Telescope Array (CTA) will be key in the understanding of the physical mechanisms powering high energy photons from Sgr A*.

Constraints on annihilating DM have been made using dwarf galaxies Ackermann et al. [2011a]; Geringer-Sameth & Koushiappas [2011] and galaxy clusters (e.g., . Ando & Nagai [2012]; Han et al. [2012d]; Chapter 2). Several independent groups have reported evidence of extended excess gamma-ray emission above the diffuse galactic background (DGB) from the central $1^\circ - 2^\circ$ around the Galactic center Abazajian & Kaplinghat [2012a, 2013]; Boyarsky et al. [2011]; Goodenough & Hooper [2009a]; Hooper & Goodenough [2011]; Hooper et al. [2012]; Hooper & Linden [2011a]. These investigations were based on Fermi Large Area Telescope (LAT) data. Although the Fermi-LAT Collaboration have not yet published a full Galactic Center analysis, in a preliminary study with one year of data, the Fermi team has reported an excess in observed counts peaking at energies of $\sim 2 - 5$ GeV Vitale & Morselli [2009]; Vitale et al. [2011]. Two main alternative explanations for its origin have been posited:

(i) DM particles with masses of about $10 - 100$ GeV annihilating into $b\bar{b}$ and $\tau^+\tau^-$ final states or a combination of both Abazajian & Kaplinghat [2012a, 2013]; Goodenough & Hooper [2009a]; Hooper & Goodenough [2011]; Hooper et al. [2012]; Hooper & Linden [2011a]. Importantly, it was argued in Chapter 3 that the signal has a relatively soft spectral shape, which makes it difficult to fit the GCEG data with a dark matter model annihilating mainly to leptons. The spatial profile of the DM was found to be well fit (Chapter 3) by a generalized NFW profile [Iocco et al., 2011] with inner slope $\gamma = 1.2$. As the DM signal is proportional to ρ^2, the spatial profile used will be the square of a generalized NFW profile with inner slope $\gamma = 1.2$. We will denote this spatial profile as $(\mathrm{NFW}^2_{1.2})$.

(ii) A superposition of $\sim 10^3$ millisecond pulsars (MSPs) within a radius of $r \lesssim 150$ pc of the Galactic Center whose number density follow a $\mathrm{NFW}^2_{1.2}$

profile Abazajian [2011]; Abazajian & Kaplinghat [2012a, 2013]; Mirabal [2013]; Wharton et al. [2012]; Chapter 3 (Paper II). However, [Hooper & Slatyer, 2013; Huang et al., 2013] have claimed that there is evidence of a gamma-ray excess at 2 kpc $\leq r \leq$ 3 kpc that is consistent with DM annihilation but is too extended to be explained by a concentrated population of MSPs given the number of MSPs that have been resolved by Fermi-LAT [Hooper et al., 2013a].

In the present chapter we scrutinize these two hypothesis using the most rigorous methods proposed in the literature [Ackermann et al., 339]. In particular, we extend the treatment of Abazajian & Kaplinghat [2012a, 2013] in a number of ways; We estimate systematic errors for the galactic diffuse background. We also evaluate marginalized confidence intervals and determine the areas of parameter space that provide an acceptable fit to the data. In Sec. 3.2 we describe the data used and some initial goodness of fit tests. In Sec. 3.3 we check the spatial fit of the models and evaluate the systematic errors in the diffuse Galactic background. The results are given in Sec. 4.5 and the discussion and conclusions are given in Sec. 3.5 and 3.6.

3.2 Fermi-LAT observations and data reduction

A detailed description of the characteristics and performance of the LAT instrument aboard Fermi is given in [Ackermann et al., 2012b]. The LAT data used in this work were collected for about 45 months of continuous sky survey observations over the period August 4th 2008−June 6th 2012 (corresponding to mission elapsed time (MET) 239557417 − 360716517). The `SOURCE` event class was chosen and photons beyond the earth zenith angle of 100° were excluded to minimize Earth albedo gamma rays. Time periods during which the spacecraft rocking angle is larger than 52° are also excluded as an additional guard against gamma-ray contamination. We further restrict the analysis to the photon energy range 200 MeV−100 GeV and make no distinction between *Front* and *Back* events.

We select all events within a squared region of interest (ROI) of size 7° × 7° centred on $(\alpha, \delta) = (266.417, -29.008)$. This position coincides with the current

best fit coordinates of the gamma-ray source `2FGLJ1745.6-2858` (Sgr A*). The analysis is performed using the LAT Science Tools package `v9r27p1` and the `P7_V6` instrument response functions (IRFs).

We model the Galactic background component using the LAT standard diffuse background model `gal_2yearp7v6_v0.fits`. The extragalactic and residual instrumental backgrounds, assumed as being isotropic, are fitted with the file `iso_p7v6source.txt`.

The analysis of the Fermi-LAT spectrum was performed using a binned likelihood technique Mattox et al. [1996] with the *pyLikelihood* library in the Science Tools. The energy binning was set to 20 logarithmic evenly spaced bins.

We adopted the same fitting procedure followed in [Abazajian & Kaplinghat, 2012a, 2013]. This is a relaxation method which consists in freeing the spectral model parameters consecutively from their distance to Sgr A*. Normalizations are freed first, and then the full spectra within concentric regions: within 2°, then within the $7^\circ \times 7^\circ$ square region and finally in the full ROI and for all sources whose $TS > 25$. Where, the test statistic (TS) is defined as in Eq. 2.1.

In the large sample limit, under the no source hypothesis, TS has a $\chi^2/2$ distribution with the number of degrees of freedom equal to the number of parameters associated with the proposed positive amplitude new source Mattox et al. [1996]; Wilks [1938] which in this case is two for position, one for amplitude, and one for spectral slope, so four in total. As the amplitude is restricted to be be non-negative, a $\chi^2/2$ distribution rather than the χ^2 distribution is needed.

Using the `make2FGLxml.py` tool we generated all the relevant 2FGL sources that could contribute to the ROI and applied to it the aforementioned relaxation method, this is called the "baseline" model [Abazajian & Kaplinghat, 2012a, 2013].

3.2.1 Detection of an Extended Source at the Galactic Center

In order to evaluate to what extent the data prefers a model that considers GC excess extended emission instead of the conventional one assumed in the second year Fermi catalogue (2FGL) [Nolan, 2012], we have constructed two residual

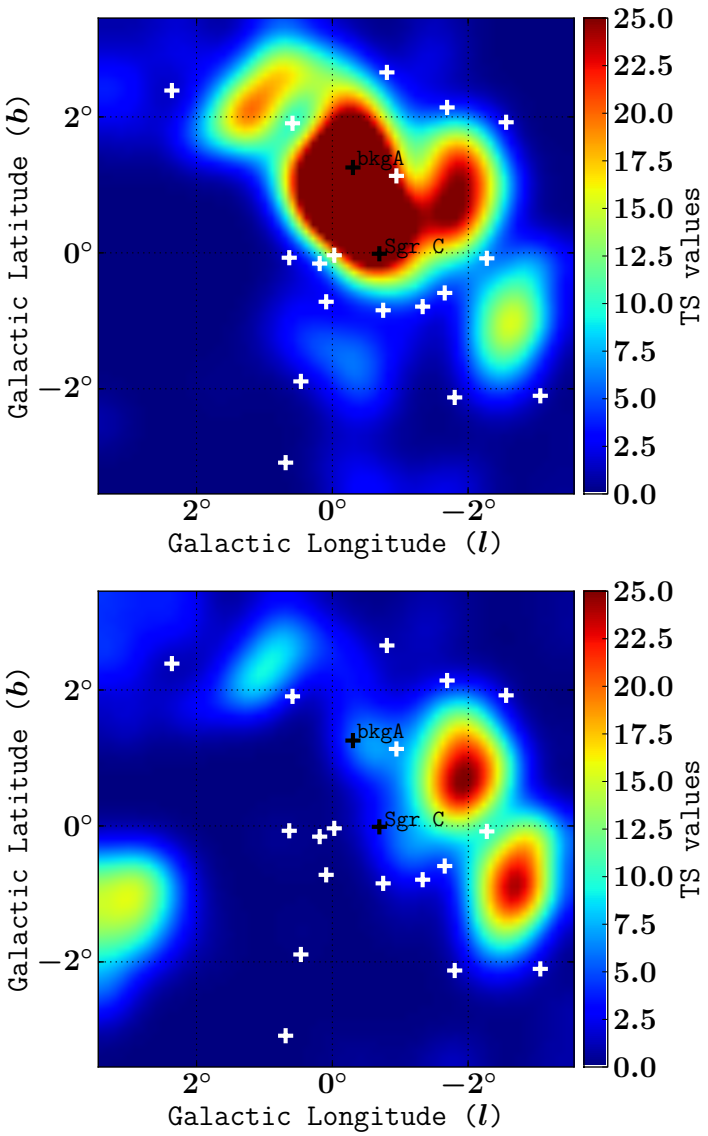

Figure 3.1: Residual test statistics (TS) maps in the energy range 300 MeV−100 GeV for two different best fit models of the Galactic Center region using: (a) only the known 2FGL point and extended sources (baseline model), highlighted here with white crosses (b) the full set of 2FGL sources plus the best fit spatial and spectral model of an extended source at the Galactic Center (see Sec 3.3 for details on maps for the extended source). The the two black crosses show the localization of two recently proposed gamma-ray PSs Yusef-Zadeh et al. [2013] named `bkgA` and `Sgr C`, whose significance drops drastically once the extended source has been taken into consideration. This can be seen in the bottom figure. The maps span a $7^\circ \times 7^\circ$ region of the sky centered at the Sgr A* position and the extent of every pixel is $0.1^\circ \times 0.1^\circ$. The residual TS maps have been smoothed for display with a $\sigma = 0.3^\circ$ Gaussian. For display purposes the images have been thresholded at $TS = 25$.

test statistics (TS) maps shown in Fig. 3.1. For a given pixel in the map, a trial new PS is added with a power law spectrum and its TS evaluated. The usual convention Nolan [2012] is to investigate the possibility of a new PS if $TS \geq 25$ for PSs far from the galactic plane. In producing the TS images, we made use of the Fermi Science Tool `gttsmap` as recommended in the `Cicerone`. [1]

We notice that by including the new best fitting spatially extended source Fig. 3.1-(b), the ROI integrated TS of the map decreased by 48% relative to a fit with no GC extended source, Fig. 3.1-(a). The inclusion of an GC extended source typically has a TS of order 800 and so very significantly favored by the data. In Yusef-Zadeh et al. [2013] two new PSs named `bkgA` and `Sgr C`, were claimed to have been discovered. In fact, our analysis shows that once the more adequate extended source is included, their significance fades in the Fermi-LAT data. Nevertheless, the incidence that these two new PSs had on the extended source hypothesis was evaluated in [Abazajian & Kaplinghat, 2012a, 2013] finding negligible variation on their main conclusions. We therefore do not attempt to model those sources in this analysis.

Visual inspection of the TS image shown in Fig. 3.1-(b) suggests that the residuals can be further ameliorated by including two new PSs at the coordinates listed in Table 3.1. However, based on the examination of the sources nearby Cygnus, Orion and molecular clouds, the Fermi collaboration [Nolan, 2012] stipulated that depending on the intensity of the diffuse background, sources near the galactic ridge need to have $TS \gg 25$ to not be considered diffuse features.

We calculated the background photon count per pixel N_{bkgd} by integrating from 589 MeV to 11.4 GeV the diffuse model cube for our ROI and found an average of $N_{bkgd} = 42.2$ counts per pixels (where each pixel spans an area of $0.1^\circ \times 0.1^\circ$). According to this source detection criteria, a new source would need to have a $TS \gtrsim 80$ to be seriously considered for a multi-wavelength search. We therefore do not claim the discovery of new PSs in the field of view.

Interestingly, in a recent study of the Virgo cluster [Han et al., 2012a], it was claimed the detection of extended gamma-ray emission interpreted as Dark Matter annihilation. That hypothesis was later disputed in Chapter 2 arguing that a set of previously unknown PSs or features of the diffuse background could

[1] http://fermi.gsfc.nasa.gov/ssc/data/analysis/documentation/Cicerone/

have accounted for the majority of the excess emission. This was later confirmed in [Han et al., 2012c].

We undertook here the same approach as in Chapter 2 and evaluated the new significance of the excess emission when the PSs in Table 3.1 are included. However, contrary to what happened in the Virgo case Chapter 2, we found that the TS and flux of the extended source at the GC were mildly enhanced (see details in Sec. 3.3).

Table 3.1: Point source candidates found in the GC field of view for almost four years of Fermi-LAT data. The PS detection and localization were carried out following the same approach explained in Chapter 2.

Right Asc. [deg]	Dec. [deg]	TS
264.813	-30.270	70.8
265.735	-31.814	65.1

In the innermost region of the GC (a circular area with a radius of about 1° centred on Sgr A*) the spectral parameters describing the gamma-ray sources are degenerate with the extended source parameters [Abazajian & Kaplinghat, 2012a, 2013]. This means that when the new extended gamma-ray source is not considered in the analysis Fig. 3.1-(a), the four nearest sources to the central position are assigned a larger amplitude to account for the excess emission [Abazajian & Kaplinghat, 2012a, 2013]. This phenomena can be seen in Fig. 3.2, where the behavior of the four sources in the innermost region is depicted.

3.3 Morphology of the Extended Source

3.3.1 Dark Matter and Pulsars Maps

The gamma ray flux emitted by WIMP particle interactions with mass $M_{\rm DM}$ can be factorized [Bergstrom et al., 1998] in two conceptually distinct terms (i) a "particle physics factor" $\Phi^{PP}(E_\gamma)$ that accounts for the number of gamma ray photons produced per annihilation event at a given photon energy, and (ii) an "astrophysical factor" $J(b,l)$, which measures the number of dark matter particle

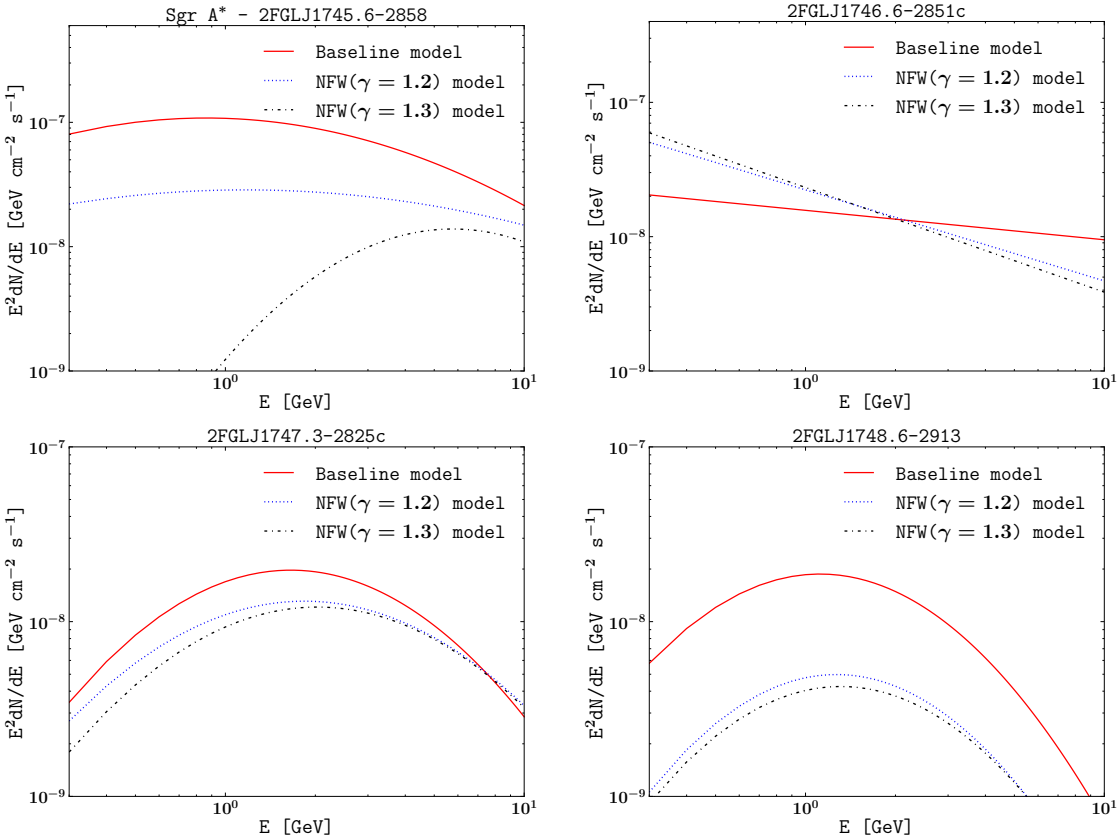

Figure 3.2: Shown is the spectrum of the four 2FGL PS displaying the largest degeneracy pattern as obtained from three different fits: Continuous red line shows the spectrum for each source that we get from our baseline model (*i.e.* a model that just assumes the conventional 2FGL sources). Blue dotted and black dash-dotted exhibit the sources spectra when the newly discovered extended source at the GC is included. This extended source is modelled with spatial maps following a universal NFW profile with inner slope $\gamma = 1.2$ and $\gamma = 1.3$ respectively (see details on maps in Sec. 3.3). The spectra of the extended source is modelled with a Log Parabola for both cases. The sources spectra shown here are organized in order of their proximity to the central position from left to right and top to bottom and all of them are located within 1° of the centre of the ROI.

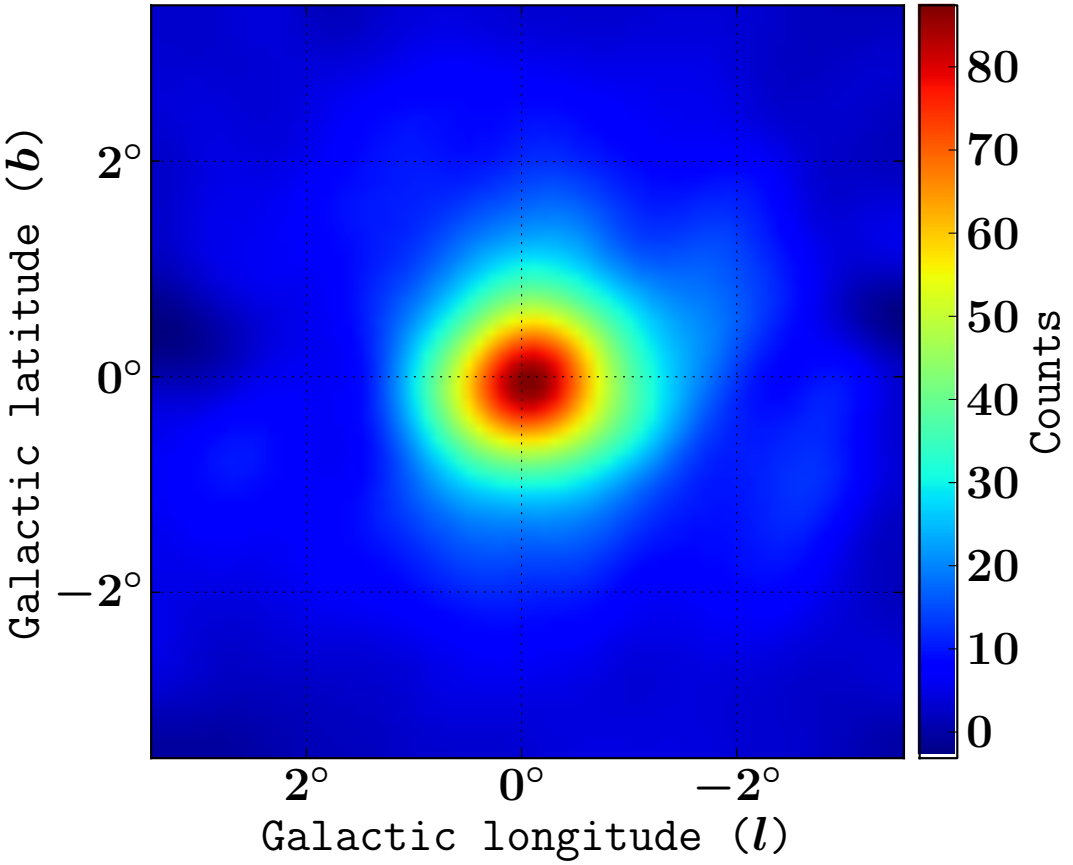

Figure 3.3: LAT residual map after subtraction of our best fit model with an extended GC source, but without subtracting the extended source model component. The counts were summed over the energy range 300 MeV−10 GeV. The map spans a $7^\circ \times 7^\circ$ region of the sky centred at the Sgr A* position with pixel size of $0.1^\circ \times 0.1^\circ$. The residual has been smoothed with a $\sigma = 0.3^\circ$ Gaussian.

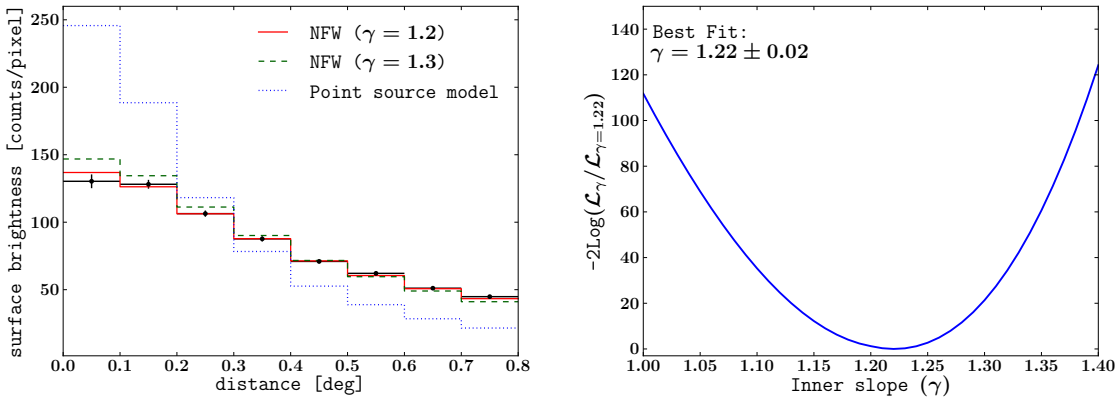

Figure 3.4: (a) Radial profile of the LAT residuals shown in Fig. 3.3 as obtained from a ring analysis computed around Sgr A*. The histograms show the effective LAT point spread function (PSF) for three different profile models: (i) NFW with inner slope $\gamma \simeq 1.2$ (red continuous line) for which we get $\chi^2/\mathrm{dof} = 5.5/7$. (ii) NFW with $\gamma = 1.3$ (green dashed line) and $\chi^2/\mathrm{dof} = 44.6/7$, and lastly (iii) the profile for a PS model (blue dotted line) with $\chi^2/\mathrm{dof} = 2479.9/7$. For all cases the spectra was modelled with a Log Parabola. (b) Shown is the significance of NFW profiles with varying inner slope, where $\mathcal{L}_\gamma$ represents the likelihood function at a given γ. This was assessed by performing a set Fermi Tools runs where for each case the relaxation method was used. The spectra was fitted with a Log Parabola function and only statistical uncertainties were taken into account.

pairs producing photons along the line of sight direction. That is

$$\Phi(E_\gamma, b, l) = \Phi^{PP}(E_\gamma) \times J(b, l), \tag{3.1}$$

where b and l are the Galactic latitude and longitude respectively. The particle physics contribution is often written as

$$\Phi^{PP}(E_\gamma) = \frac{1}{2} \frac{\langle \sigma v \rangle}{4\pi M_{DM}^2} \sum_f \frac{dN_f}{dE_\gamma} B_f, \tag{3.2}$$

where $\langle \sigma v \rangle$ is the annihilation cross-section of two DM particles times their relative velocity, averaged over the velocity distribution. dN_f/dE_γ is the differential gamma ray multiplicity per annihilation, B_f the branching ratio and f stands for the final state particles resulting from the annihilation. Note, that in this work we only consider prompt emission, that is, we do not take into account the possible effects of diffusion from secondary charged particles. This will enable us to compare our results with those by Abazajian & Kaplinghat [2012a, 2013]; Boyarsky et al. [2011]; Goodenough & Hooper [2009a]; Hooper & Goodenough [2011]; Hooper & Linden [2011a].

The astrophysical factor in the (b, l) direction is integrated over the line of sight [Bergstrom et al., 1998]

$$J(b, l) = \int_0^\infty ds \;\; \rho(r)^2 \big|_{r=\sqrt{R_\odot^2 - 2sR_\odot cos(b)cos(l) + s^2}}, \tag{3.3}$$

with s varying in the line-of-sight path and $R_\odot = 8.25$ kpc is the distance from the solar system to the GC. Since the spatial binning of our Fermi files was $0.1^\circ \times 0.1^\circ$, we constructed the spatial maps by averaging the astrophysical factor over the corresponding solid angle around the (b, l) coordinates [Bergstrom et al., 1998]

$$\langle J(b, l) \rangle_{\Delta\Omega} = \frac{1}{\Delta\Omega} \int_{\text{pixel}} J(b, l) d\Omega, \tag{3.4}$$

where the differential solid angle is given by $d\Omega = db\, dl \cos(b)$.

As in [Abazajian & Kaplinghat, 2012a, 2013], throughout this work we shall use template maps of DM that assume a generalized Navarro-Frenk-White (NFW)

profile Klypin et al. [2002]; Navarro et al. [1996]

$$\rho(r) = \frac{\rho_s}{\left(\frac{r}{r_s}\right)^{\gamma}\left[1+\left(\frac{r}{r_s}\right)^{\alpha}\right]^{(\beta-\gamma)/\alpha}}, \tag{3.5}$$

where we fixed $r_s = 23.1$ kpc, $\alpha = 1$, and $\beta = 3$.

It has been suggested that the excess emission seen in the GC can also be explained by a superposition of unresolved PSs (MSPs) that might be distributed as a mildly contracted NFW profile. We tested this hypothesis by normalizing to unity the $\langle J(b,l)\rangle$ maps as explained in the `Cicerone`. [1]

These normalized maps were also used to fit for the inner slope γ. This was done with two equivalent methods:

- We first computed the residual emission shown in Fig. 3.3. From this we produced a radial profile Fig. 3.4-(a) of the photon excess. This was compared with that expected from a PS and also from well motivated spatially extended sources using a χ^2 test. The profiles for extended source shown in the histograms Fig. 3.4-(a) were obtained with the `gtmodel` routine. The models entered to this Tool were $\langle J(b,l)\rangle$ maps normalized to unity with $\gamma \in [1.0, 1.5]$ and a Log Parabola spectra

$$\frac{dN}{dE} = N_0 \left(\frac{E}{E_0}\right)^{-\left(\alpha+\beta\log\left[\frac{E}{E_0}\right]\right)}. \tag{3.6}$$

  The height of each bin is given by the mean of the residual in a ring of pixels centered around the GC. The error bars were evaluated as the standard deviation of the pixels in the ring divided by the square root of the number of pixels in the ring.

- Following a more statistically robust approach we proceeded to fit for γ with the *pyLikelihood* Tool Fig. 3.4-(b). Compared to the previous method, this one has the advantage of carefully considering the energy binning in the likelihood function.

[1] http://fermi.gsfc.nasa.gov/ssc/data/analysis/scitools/extended

As we are using the profile likelihood approach Rolke et al. [2005], we set $\gamma = 1.2$ unless otherwise specified. Although ideally one should maximize the likelihood for γ simultaneously with the other parameters, our initial tests show that the preference for $\gamma = 1.2$ is robust to changes in the spectral model. Also maximizing the likelihood of the microlensing and dynamical data (see Fig. 5 of Iocco et al. [2011]), $\gamma = 1.2$ corresponds to $\rho_0 \equiv \rho(R_\odot) = 0.36$ GeV cm^{-3}. From PhiPhiPPJnfw the annihilation gamma ray flux is $\Phi \propto \langle \sigma v \rangle \, \rho_0^2$ and so ρ_0 is not constrained by the Fermi-LAT measurements alone. Also, the microlensing and dynamical data have a very weak constraint on γ, compared to our Fermi-LAT analysis and so this justifies using the Fermi-LAT best fit value for γ in constraining ρ_0.

The microlensing and dynamical data constrain the scale radius to be $r_s = 20^{+15}_{-10}$ kpc Iocco et al. [2011]. As this is much larger than the extent of the excess emission (200 pc), the gamma ray data is not able to constrain r_s. But, as can be seen from Jnfw, r_s may effect J and it will also be completely degenerate with $< \sigma v >$. In line with the profile likelihood approach, we choose r_s to be consistent with the maximum likelihood value given in [34]. It would be better to use the maximum likelihood value of r_s when γ is fixed to 1.2, but the joint confidence intervals for r_s and γ are not given in Iocco et al. [2011]. Our current approach should provide a reasonable approximation, unless the microlensing and dynamical data have a very high correlation in the joint confidence intervals for r_s and γ.

As it has been seen in Fig. 3.4-(a) and Fig. 3.4-(b), comparisons between LAT PSFs and photon distributions indicates that the observed excess emission is consistent with an extended source whose spatial distribution is well described by a mildly contracted NFW profile. Below we outline how we examined its spectral morphology for a DM hypothesis.

We calculated the gamma ray spectra from WIMPs self-annihilations with the `DMFIT` tool as described in [Jeltema & Profumo, 2008]. This package provides interpolating functions calculated from simulations of DM annihilations with the `DarkSUSY` software [Gondolo et al., 2004] which in turn interpolates over `PYTHIA 6.4` [Sjostrand et al., 2006] tables.

It has recently been pointed out that there are discrepancies [Cembranos et al., 2013] between the gamma ray spectra calculated with `PYTHIA 6.4` (Fortran

version) and `PYTHIA 8.1` [Sjostrand et al., 2008] (C++ version), that software analysis using interpolating functions can overestimate the energy cut-off of the gamma-ray spectra, and that not considering electroweak corrections can also create deviations between predicted DM annihilitions spectra [Ciafaloni et al., 2011; Kachelriess et al., 2009]. We therefore looked for a statistical bias in our analysis by producing `PYTHIA 8.1` tables for a few WIMP masses and found that for the relevant energy scale and annihilation channels used in our work, the discrepancies between the results obtained with DMFIT and `PYTHIA 8.1` were marginal.

For the DM spectrum we considered soft gamma ray spectra produced from annihilation into $b\bar{b}$ quarks and hard spectra as produced by annihilations into $\tau^+\tau^-$ or a combination of leptons pairs e^+e^-, $\mu^+\mu^-$ and $\tau^+\tau^-$. Since the annihilation products are highly model dependent we studied extremes of the possible annihilation channels assuming a branching ratio of 100% for each of them in turn (except for the case of 100% e^+e^-), but mixtures of soft and hard spectra were also evaluated in order to fit for the best branching ratio B_f.

3.3.2 Examination of Systematics in the Galactic Diffuse Background Model

The LAT team developed a model for the Galactic diffuse background map which is an essential input to the analysis for detecting and characterizing gamma ray sources. The model file `gal_2yearp7v6_v0.fits` introduced in the 2FGL catalogue [Nolan, 2012] was created by fitting all-sky gamma ray data with a highly sophisticated physical model. In a nutshell; the distribution of interstellar gas and dust was obtained from independent observations, then three-dimensional models of magnetic fields, distributions of optical photons and models of p and e^- injections were assumed. By propagating these primary particles through the gas with the GALPROP[1] software package, the resulting photons from inverse Compton (IC), bremsstrahlung and π^0 decays, were predicted and fitted with gamma ray data.

Since the newly discovered extended source is located in the region where

[1] http://galprop.stanford.edu

the Galactic diffuse background component largely dominates over any other sources, we therefore expect the uncertainties[1] associated with the Galactic diffuse background model to constitute the largest systematic effects for the analyses in this study.

In order to estimate the uncertainties of the Galactic diffuse background at the GC, we would like to examine a region of the sky which has a similar Galactic diffuse background as the GC but does not contain any other sources which then would also contribute to the residuals. As argued in Ackermann et al. [2012a], the Galactic diffuse background has a relatively similar uncertainties within the inner Galaxy ($-80^\circ \geq l \leq -80^\circ$, $-8^\circ \leq b \geq 8$). Based on these considerations, we estimate the percentage uncertainties from nearby regions, along the Galactic plane, which do not have any point sources.

We first examined the spectral uncertainties by obtaining the energy dependence of our model residuals. Following a similar approach to that explained in [Abdo et al., 2010], we compared the observed counts with the model counts in a nearby circular region with a radius of 0.5° centred on $\Delta l \sim +2.3^\circ$ and $\Delta b \sim 0^\circ$ where the Galactic diffuse background component was found to be dominant, see Fig. 3.5-(a). The "model counts" map was computed from our best fit model (*i.e.* the baseline model plus a NFW distributed source with $\gamma = 1.2$ and Log Parabola spectra). This step is summarized in Fig. 3.5-(b), where the residuals as function of energy are shown.

In order to assess the spatial uncertainties of the Galactic diffuse background component, we quantified the dispersion of the fractional residuals in 10 regions, where the Galactic diffuse background component was found to be dominant. The regions selected are located in the Galactic plane and special attention was put on not considering sectors with known 2FGL PSs within them. The fractional residual for each region was calculated in five energy bands: 0.30−0.50 GeV, 0.50−0.80 GeV, 0.80−1.30 GeV, 1.3−10 GeV and 10−100 GeV. The results obtained in this step are shown in Fig. 3.6. It follows that the standard deviation of the fractional residuals is 11%. We thus used this value as an estimate of the uncertainties in the spatial distribution of the Galactic diffuse background com-

[1]The uncertainties are mainly due to contributions of unresolved PSs and imperfections of the Galactic diffuse background model.

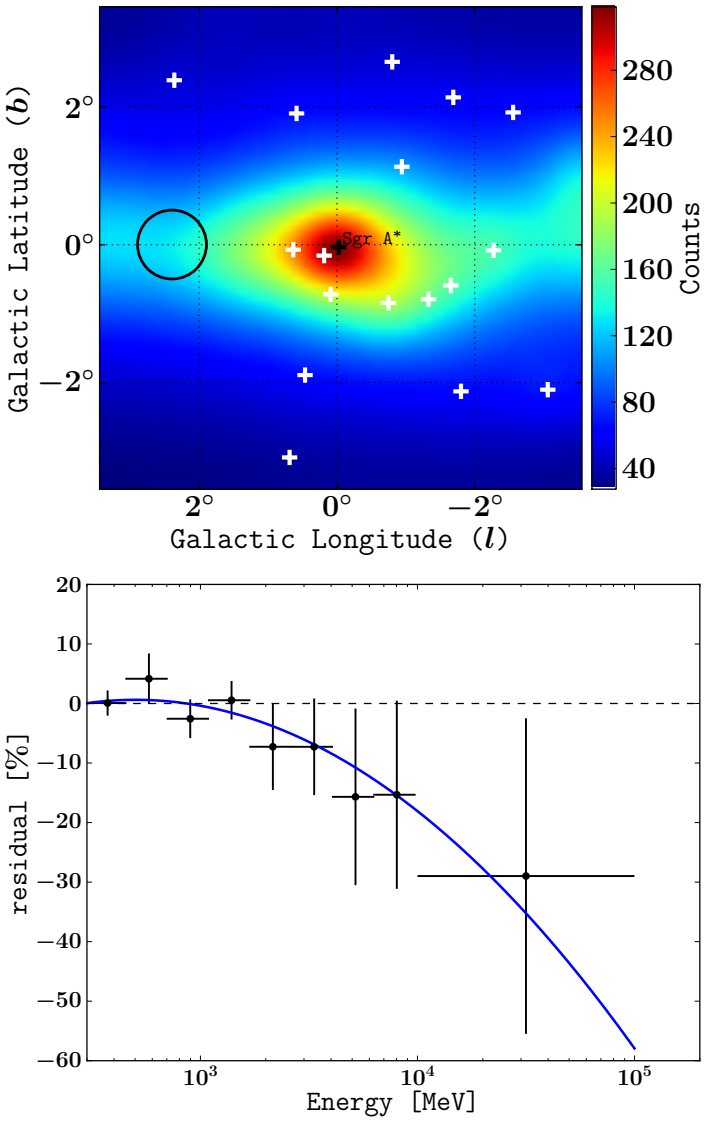

Figure 3.5: (a) Counts map in the 0.3−100 GeV energy band of the best fit model for the ROI. This model considered the conventional 2FGL sources plus an additional extended source at the central position (see details in Sec. 3.3.1). Gaussian smoothing is applied with a kernel size of $\sigma = 0.3°$. The black circle superposed on the image shows a region dominated by the Galactic diffuse background that was used to examine the spectral uncertainties. (b) Fractional residuals, that is (observed-model)/model, evaluated at eight energy bins in a circle centered at $(l, b) = (+2.3°, 0°)$ with radius of 0.5° shown in the above image. The residual data was fitted with a quadratic function in logarithmic scale as described by the blue line.

ponent. A similar magnitude for the spatial and spectral uncertainties was found in [Abdo et al., 2010] which was also in the inner Galaxy.

The spectral and spatial uncertainties described above will be used in Sec. 3.3.3 to estimate the systematic error in flux of the extended source.

3.3.3 Spectral Morphology of the Extended Source

The procedure of obtaining the spectral energy distribution (SED) of the extended source was based on the method used for the flux band analysis in [Nolan, 2012]. We started by applying the relaxation method (explained in Sec. 3.2) to the ROI in the full energy range of 0.3−100 GeV. The extended source was modeled with a NFW($\gamma = 1.2$) map normalized to unity and the spectra with a Log Parabola formula, as defined in Eq. 3.6. Once the best fit spectral parameters $\alpha(E_0)$ and β have been found, we calculated the spectral slope of the Log Parabola at any given energy as

$$\alpha(E) = \alpha(E_0) + 2\beta \log\left(\frac{E}{E_0}\right), \tag{3.7}$$

where E_0 is the pivot energy [Nolan, 2012].

We divided the energy range of the extended source into 12 energy bands evenly separated in the range 0.3−10 GeV and one energy band from 10 GeV to 100 GeV. Next, the extended source photon fluxes in each band were computed by freezing the spectral indexes of all the 2FGL sources to those obtained in the fit over the full range and fitting the normalizations in each spectral band. Note that the diffuse galactic and extragalactic backgrounds were not frozen and neither where the PS amplitudes. They were optimized along with each band amplitude. In an initial analysis we had also included a 200−300 MeV band but we found it had a TS of only 0.4, so we did not include it in our further analysis. Also, the extended source models generally have a negligible amplitude in the 200−300 MeV band compared to Sgr A*. For each remaining energy band, the GC extended source spectrum was approximated by a power law function

$$\frac{dN}{dE} = N_0 \left(\frac{E}{E_0}\right)^{-\Gamma}, \tag{3.8}$$

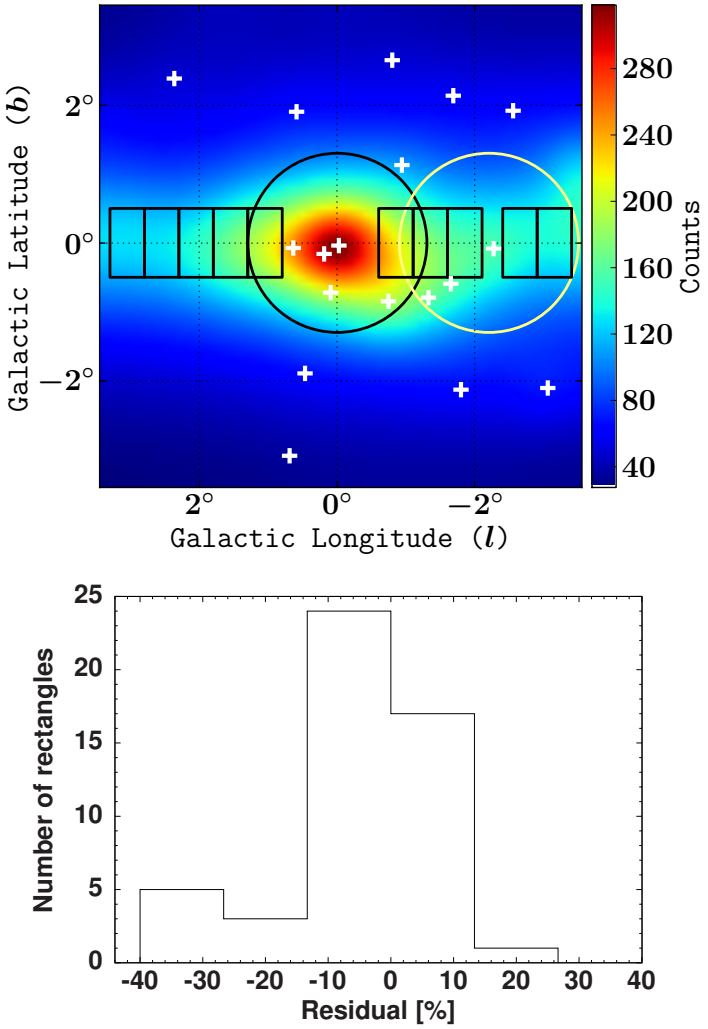

Figure 3.6: (a) Counts map in the 0.3−100 GeV energy band smoothed with a Gaussian filter of radius $\sigma = 0.3°$. The black rectangles ($1.0° \times 0.5°$) highlight the regions selected for the examination of the spatial uncertainties in the Galactic diffuse background. The black and yellow circles show the regions where the flux of the file `gal_2yearp7v6_v0.fits` was varied to evaluate the effects of the spatial dispersion of the model. (b) Histogram of the fractional residuals for ten rectangular regions in five energy bands: 0.30−0.50 GeV, 0.50−0.80 GeV, 0.80−1.30 GeV, 1.3−10 GeV and 10−100 GeV. The residuals were calculated as (observed-model)/model, where we also subtracted the best fit fluxes of all the sources (except for the Galactic diffuse background source) from the observed counts map. As there are 10 rectangles and 5 energy bands, the histogram is compiled from of a total of 50 values.

where the spectral index Γ in a band was set to the local spectral slope defined in Eq. 3.7, at the logarithmic mid-point of the band $\sqrt{E_n E_{n+1}}$, restricted to be in the interval $[0, 5]$. We calculated 2σ upper limits instead of actual fluxes for those bands with either a Test Statistics $TS < 10$ or relative uncertainty on the flux $\Delta F_i/F_i > 0.5$.

Systematic errors due to uncertainties in the Galactic diffuse background model were evaluated by modifying the model file `gal_2yearp7v6_v0.fits` in the band analysis. This was done differently for spectral and spatial uncertainties:

- To calculate the spectral uncertainties we performed an additional band analysis where we altered the energy distribution of the Galactic diffuse background model according to the curve in Fig. 3.5. We thus compared the fit with and without this modification and set the spectral systematic error to be the difference between the two.

- Spatial uncertainties were estimated using two modified `gal_2yearp7v6_v0.fits` files in the fit. For all energy bins in the model cubes, we varied the fluxes by 11% in first, a disk of radius 1.3° centred on Sgr A* and then an offset disk at $(b, l) = (0°, 2.1°)$ with the same dimensions. Again, after a comparison of both fits we chose the one with the largest uncertainties to included in our SED calculation. Both disks are illustrated on Fig. 3.6-(a).

The resulting systematic errors due to uncertainties of the spectral distribution in the Galactic diffuse background model were found to on average be about 2%, while for the spatial errors we obtained on average about 20%, both for the energy ranges $\leq$ 10 GeV. For the 10 to 100 GeV band we found the systematic error to be of order 40%. Also, we find that in general the models that fit the $\leq$ 10 GeV range have negligible values in the higher than 10 GeV band. For these reasons we do not use the 10 to 100 GeV energy band.

Total systematic errors were computed by adding in quadrature the spatial, spectral and effective area systematics which is explained below eq:Csyst. In Figure 3.7 we show the SED of the extended source with the best fit over the full range overlaid. The red error bars indicate the total systematic errors and black error bars the statistical uncertainties. We also list the SED and errors in Table V of Appendix 4.2 so that the reader may try fit other spectral models.

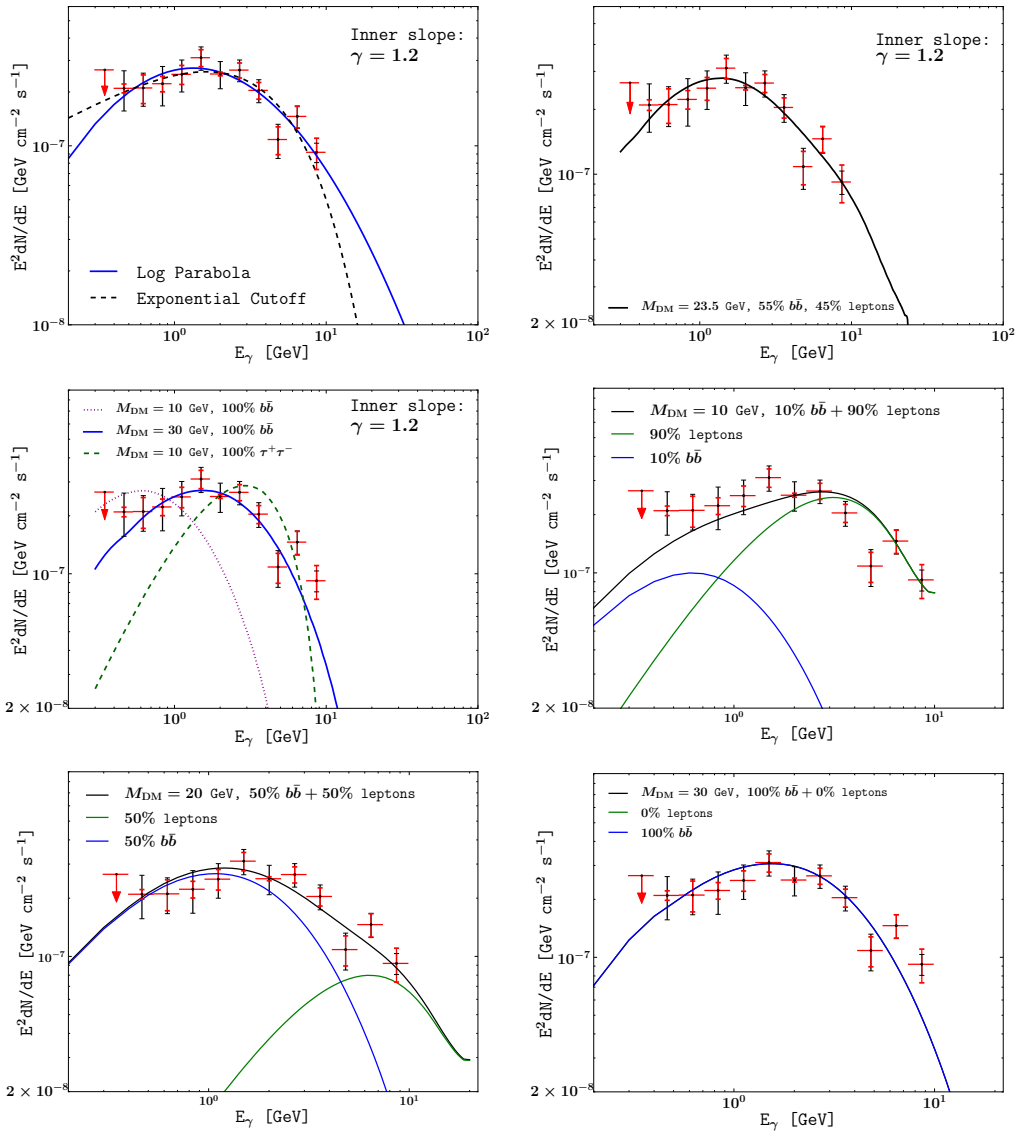

Figure 3.7: Spectrum of the extended source measured with the Fermi-LAT. As shown in the legends, the model for the spatial distribution of the source is a NFW profile with inner slope $\gamma = 1.2$. The red and black error bars show the (1σ) systematic and statistical errors, respectively. The upper limit is 2σ. The fit over the full range is overlaid over the twelve band energy fluxes on each figure as follows: (a) The continuous blue line and dashed black line represent the best fit spectrum for a population of MSPs resembling a NFW spatial distribution. (b) Shown is the best fit DM spectrum. $M_{\rm DM}$, B_f and $\langle\sigma v\rangle$ were treated as free parameters in the fit (here "leptons" denotes an unweighted mixture of e^+e^-, $\mu^+\mu^-$ and $\tau^+\tau^-$), respectively. (c) Panel shows 3 different examples of DM spectra with high TS values as obtained with Fermi Tools. (d)- (f) Show several combinations of leptons and quarks that provide a good fit to the data.

In order to study the validity of the distinct types of spectral shapes found with high TS values in our Fermi Tools runs, we used the same spectral fit quality estimator introduced in [Nolan, 2012] except that we also added our systematic errors for the diffuse Galactic background

$$C_{\rm sys} = \sum_i \frac{(F_i - F_i^{\rm fit})^2}{\sigma_{i\,\rm stat}^2 + \sigma_{i\,\rm spatial}^2 + \sigma_{i\,\rm spectral}^2 + \sigma_{i\,\rm area}^2} \tag{3.9}$$

where i runs over all bands with $TS > 10$, $F_i^{\rm fit}$ is the flux predicted in that band from the spectral fit to the full band and the denominator contains a sum of the squares of the statistical error, the Galactic diffuse background spatial systematic error, the Galactic diffuse background spectral systematic error, and the effective area systematic error. Also, $\sigma_{i\,\rm area}^2 = (f_i^{\rm rel} F_i^{\rm fit})^2$ where $f_i^{\rm rel}$ represents the systematic uncertainty in the effective area Nolan [2012]. The f_i were set to 0.05 for the first seven bands and 0.08 from band eight to twelve. The first energy band situated in the range 300 MeV−400 MeV was found to have a $TS < 10$, therefore it was not included in our analysis. We will assume that has a χ^2 distribution with the number of degrees of freedom equal to the number of bands (11) minus the number of parameters used to determine $F_i^{\rm fit}$. Assuming that the systematic errors can be treated as independent and Gaussian distributed, this is a good approximation as we have a large number of counts for each band.

The goodness of fit can be evaluated from the p-value which is the probability of taken on a value larger than the observed value. We can evaluate the p-value as $\int^{\infty} p(x)\,dx$ where $p(x)$ is a χ^2 distribution with degrees of freedom equal to 11 minus the number of parameters. In Nolan [2012] they take a good fit to be one with a p-value greater than 10^{-3}. For a 2 parameter fit with 11 bands this corresponds to < 27.9. For the 3 parameter case this corresponds to < 26.1.

In the first row of Fig 3.7 we show examples of spectra with high TS values and significant curved spectral shapes for two well motivated hypothesis; an unresolved population of MSPs in the GC and dark matter self-annihilating into a mixture of $b\bar{b}$ quarks and leptons. While Figure 3.7-(c) shows examples of DM spectra proposed in the literature as good-fitting models for the GC gamma ray excess. However, our analysis demonstrates that DM particles of $M_{\rm DM} = 10$ GeV annihilating into $\tau^+\tau^-$ or $b\bar{b}$ only do not fit the LAT data correctly, since they

have $\gg 27.9$.

3.4 Results

3.4.1 Millisecond Pulsars

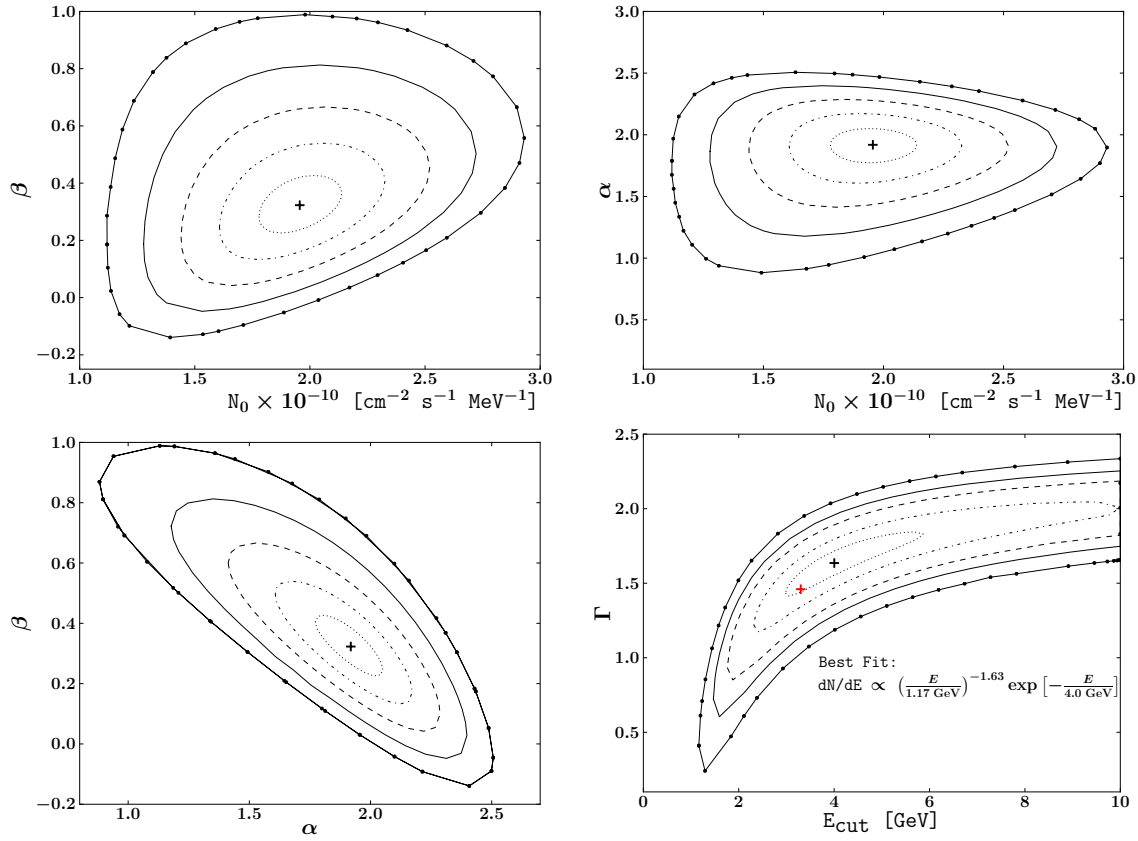

Figure 3.8: Confidence regions (1σ, 2σ,...5σ) for an unresolved population of Millisecond Pulsars using Fermi-LAT data taken from around the GC in the energy range 0.3−10 GeV. The spatial distribution of Pulsars follows a normalized NFW profile with inner slope $\gamma = 1.2$. The two frames in the upper panel and the first one in the lower panel use a Log Parabola with $E_0 = 1176$ MeV for spectral shape, but, the second figure in lower row uses an exponential cut-off as shown in the plot. Best fit parameters are denoted by black crosses. The red cross is the best fit obtained in [Hooper et al., 2013b] as the average best-fit of all the MSPs reported in the 2FGL catalogue.

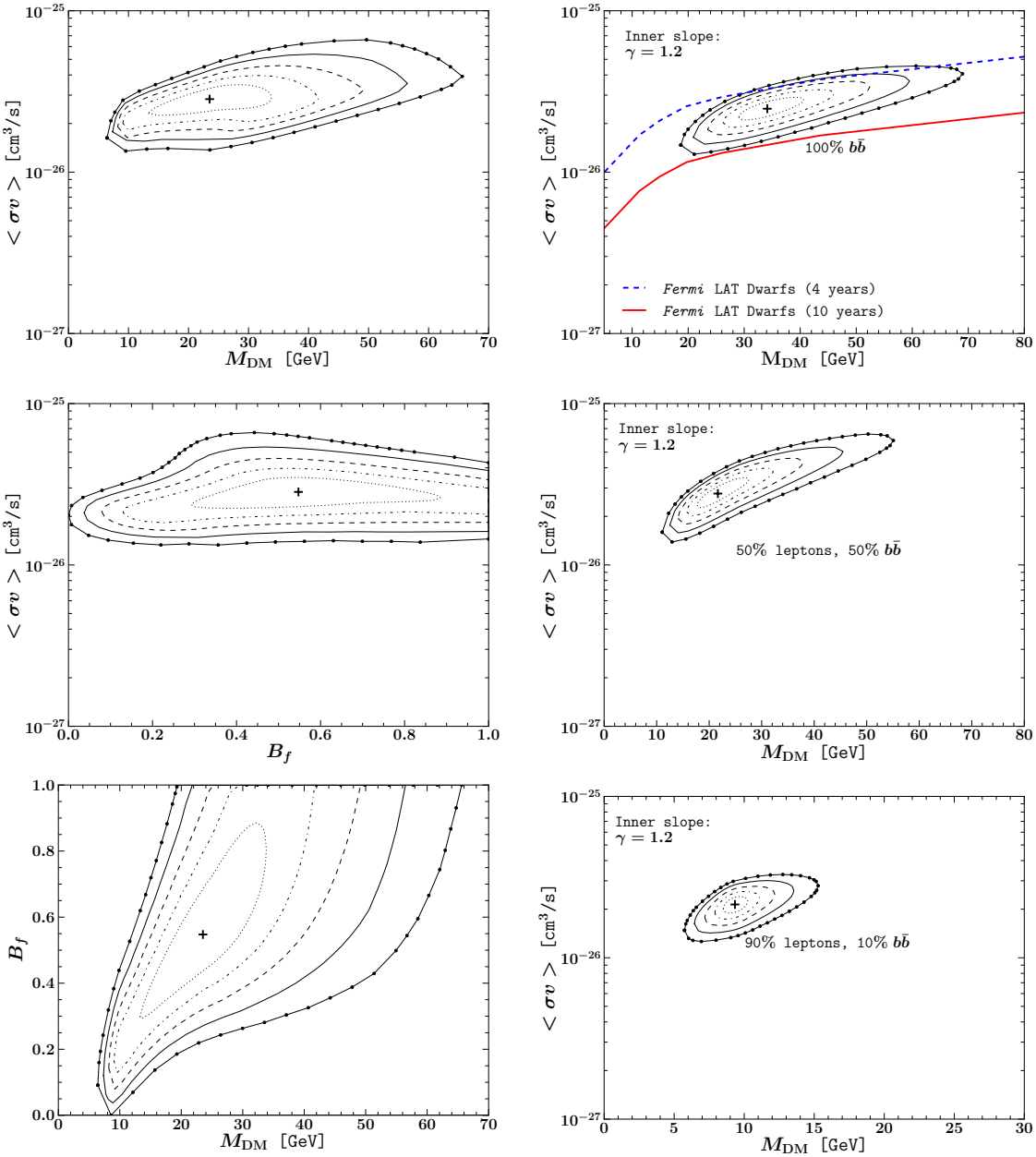

Figure 3.9: Confidence regions (1σ, 2σ,...5σ) for dark matter using Fermi-LAT data taken from around the GC in the range 0.3−10 GeV. `Left Panel:` Best fit $M_{\rm DM}$, $\langle\sigma v\rangle$ and B_f and errors, marginalized over the remaining parameter. Where $B_f = 1.0$ implies 100% $b\bar{b}$ and $B_f = 0.0$ means 100% leptons (*i.e* an unweighted combination of e^+e^-, $\mu^+\mu^-$ and $\tau^+\tau^-$ pairs). The Dark matter spatial distribution follows a NFW profile with inner slope $\gamma = 1.2$. `Right Panel:` Best fit $M_{\rm DM}$ and $\langle\sigma v\rangle$ for several fixed values of B_f as indicated in the figures. The crosses in all frames denote the best-fit point. See Tables 3.2 and 3.3.

It has been suggested [Abazajian & Kaplinghat, 2012a, 2013] that a population of $\sim 10^3$ Millisecond Pulsars (MSPs) constitutes a reasonable explanation for the gamma ray excess seen in the GC. The main physical reasons that support this claim are: MSPs can emit gamma rays over large time scales, their binary companions could prevent them from free-streaming out the GC and estimates of the spatial distribution of M31 low mass X-ray binary population indicate that the number of MSPs located in the GC could scale as steeply as $1/r^{2.4}$ (with r the two-dimensional projected radius).

To compare the spectral shape of the gamma ray excess seen in the GC with that of typical LAT MSPs in the second year pulsar catalogue [Nolan, 2012], we fit the LAT spectrum of the GC extended source by a power law with exponential cutoff:

$$\frac{dN}{dE} = K \left(\frac{E}{E_0}\right)^{-\Gamma} \exp\left(-\frac{E}{E_{\rm cut}}\right), \tag{3.10}$$

where photon index Γ, a cut-off energy $E_{\rm cut}$ and a normalization factor K are free parameters. The best fit parameters, with $E_0 = 1176$ MeV, were $K = 2.5 \times 10^{-10} \pm 4 \times 10^{-11}$ ph cm^{-2} s^{-1} MeV^{-1}, $E_{\rm cut} = 4000 \pm 1500$ MeV, and $\Gamma = 1.6 \pm 0.2$. The confidence regions are shown in the lower right panel of Fig. 3.8. It has been found in [Hooper et al., 2013b] that the sum of the spectra of the 37 MSPs reported in the 2FGL catalogue are well described by Eq. 4.2 with $\Gamma = 1.46$ and $E_{\rm cut} = 3.3$ GeV (see the red cross in Fig. 3.8-(d)). Therefore the LAT spectrum of the extended source in the GC agrees within 1σ with what has been observed from the 37 resolved MSPs of the 2FGL.

The best fit and confidence intervals were performed with the tool `Minuit` [James & Roos, 1975]. eq:Csyst was used as the goodness of fit statistic. Note that the 1σ contours, for our two dimensional plots, corresponds to the 68.3% profile likelihood Rolke et al. [2005] confidence region and are defined by all areas of the two dimensional parameter space which have a $\Delta \leq 2.3$ where Δ is the difference between at the best fit point in the plot and at the point considered for inclusion within the confidence interval. All other parameters not shown in a plot are chosen to minimize at each point in the plot. The corresponding Δ thresholds for 2, 3, 4, and 5 σ are 6.2, 11.8, 19.3, and 28.7 respectively (see for example

the Statistics section of the "The Review of Particle Physics" [Beringer et al., 2012a]). For any one parameter confidence intervals, we quote the 68.3% level which corresponds to a $\Delta = 1$ threshold.

Frames shown in the upper panel and left lower panel of Fig. 3.8 describe the results of a spectral fit to the LAT data using a Log Parabola formula 3.6 instead of an exponential cut-off. As it can be seen, the full parameter space is shown in three two-dimensional plots. The model parameter E_0 in Eq. 3.6, kept fixed during the fit and set to $E_0 = 1176$ MeV, was calculated as the energy at which the relative uncertainty on the differential flux N_0 was minimal. This was done with a damping procedure that made use of the covariance matrix between parameters as obtained from the `MIGRAD` algorithm in `Minuit` [James & Roos, 1975]. The best-fit parameters shown with black crosses in the corresponding frames of Fig. 3.8 are $N_0 = 1.96^{+0.18}_{-0.17} \times 10^{-10}$ ph cm^{-2} s^{-1} sr^{-1}, $\alpha = 1.92^{+0.13}_{-0.15}$ and $\beta = 0.32^{+0.10}_{-0.09}$ (for completeness, the $\pm 1\sigma$ total errors are included as well).

In [Abazajian & Kaplinghat, 2012a, 2013] the fit to the gamma ray data was performed by considering statistical errors only and fixing $E_0 = 100$ MeV in the Log Parabola. However, we found that this choice of pivot energy produces a large correlation between the parameters N_0, α and β. We thus notice that this degeneracy can be alleviated by searching for a more adequate value of E_0, as outlined above.

3.4.2 Self-Annihilating Dark Matter

Best-fit Branching ratio	$\langle \sigma v \rangle$ [cm^3/s]	$M_{\rm DM}$ [GeV]
$55^{+18}_{-16}\%$ $b\bar{b}$	$2.84^{+0.43}_{-0.41} \times 10^{-26}$	$23.5^{+6.7}_{-6.6}$

Table 3.2: Best fit values on the DM velocity averaged annihilation cross-section, DM mass and branching fraction when the three parameters are varied at a time. The spectra is constructed as an evenly weighted combination of $b\bar{b}$ and leptons pairs. The leptons fraction denotes an unweighted combination of e^+e^-, $\mu^+\mu^-$ and $\tau^+\tau^-$ pairs. Errors shown here include systematic uncertainties. See left panel of Figure 4.6 for further details.

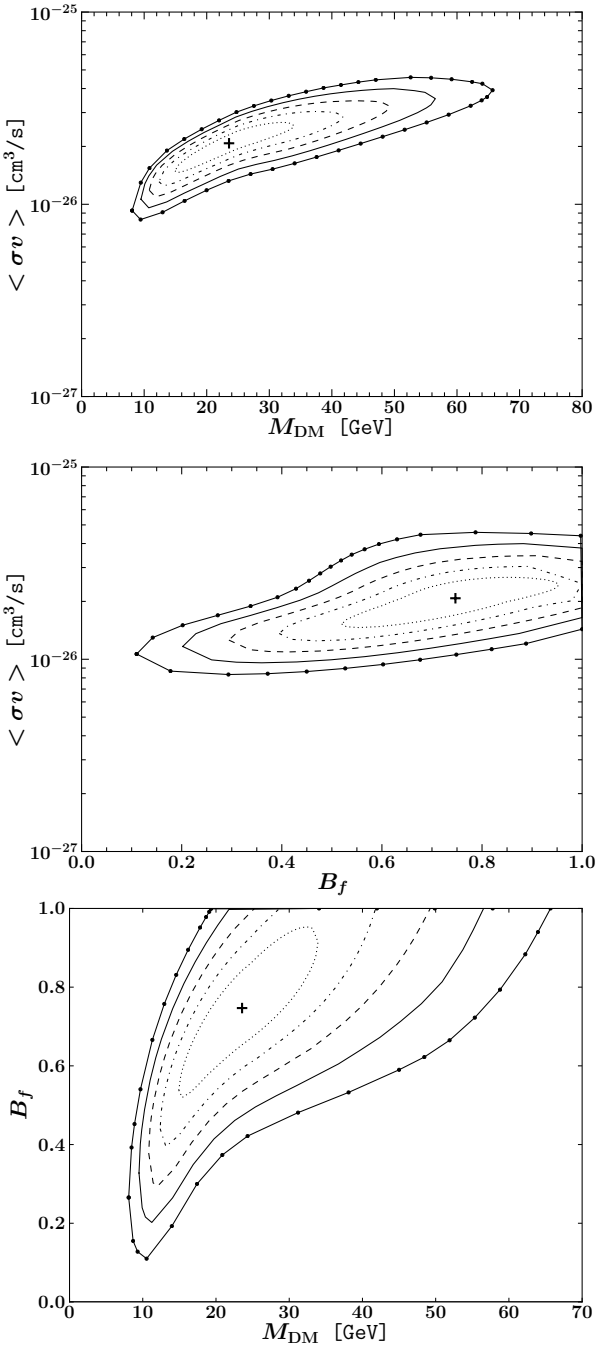

Figure 3.10: Confidence regions (1σ, 2σ,...5σ) for dark matter using Fermi-LAT data taken from around the GC in the range 0.3−10 GeV. Best fit $M_{\rm DM}$, $\langle\sigma v\rangle$ and B_f and errors, marginalized over the remaining parameter. Where $B_f = 1.0$ implies 100% $b\bar{b}$ and $B_f = 0.0$ means 100% $\tau^+\tau^-$. The Dark matter spatial distribution follows a NFW profile with inner slope $\gamma = 1.2$. The crosses in all frames denote the best-fit point. See also Table 3.4.

Branching ratio	$\langle\sigma v\rangle$ [cm^3/s]	$M_{\rm DM}$ [GeV]
100% $b\bar{b}$	$2.47^{+0.28}_{-0.25} \times 10^{-26}$	$34.1^{+4.0}_{-3.5}$
50% $b\bar{b}$, 50% leptons	$2.77^{+0.47}_{-0.35} \times 10^{-26}$	$21.7^{+3.8}_{-2.8}$
10% $b\bar{b}$, 90% leptons	$2.14^{+0.17}_{-0.16} \times 10^{-26}$	$9.3^{+0.6}_{-0.5}$

Table 3.3: Best fit $M_{\rm DM}$ and $\langle\sigma v\rangle$ for several fixed values of B_f. The leptons fraction denotes an unweighted combination of e^+e^-, $\mu^+\mu^-$ and $\tau^+\tau^-$ pairs. Errors shown here include systematic uncertainties. See right panel of Figure 4.6 for further details.

Best-fit Branching ratio	$\langle\sigma v\rangle$ [cm^3/s]	$M_{\rm DM}$ [GeV]
75^{+13}_{-15}% $b\bar{b}$	$2.1^{+0.27}_{-0.45} \times 10^{-26}$	$23.6^{+6.7}_{-6.4}$

Table 3.4: Best fit values on the DM velocity averaged annihilation cross-section, DM mass and branching fraction when the three parameters are varied at a time. The spectra is constructed as an unweighted combination of $b\bar{b}$ and $\tau^+\tau^-$ pairs. Errors shown here include systematic uncertainties. See Figure 3.10 for further details.

We have seen in Figures 3.3 and 3.4 that there is evidence for a single strong positive residual emission in the Galactic Center with a spatial morphology that agrees well with that of a NFW profile with inner slope $\gamma = 1.2$. Also, the evaluation of the systematic uncertainties related to imperfections in the Galactic diffuse background led us to the conclusion that the dark matter signals are much larger in size than the systematic errors. Thus, the next logical step is to calculate the regions of the self-annihilating DM parameter space that provide a good fit to the LAT data. In Figures 4.6 and 3.10 we present the main results of this analysis. Contours are shown at 1σ, 2σ,...5σ confidence level.

In the right upper panel of Fig. 4.6 we show the preferred regions of the parameter space for 100% $b\bar{b}$ final states. The 95% upper limits obtained in the Fermi-LAT analysis of Dwarf Galaxies [Ackermann et al., 2011b] are also shown for comparison. We notice that the best DM region is not yet in tension with those limits. However, one would expect that the limits obtained from Dwarf Galaxies will be strengthened with larger data sets. We estimated that for 10 years of LAT data obtained from observations of Milky Way Dwarf Galaxies the

95% upper limits on $\langle\sigma v\rangle$ can be approximated to two standard deviations of a Gaussian with a mean of zero. As the standard deviation is inversely proportional to the square root of the number of observations we can approximate the upper limits for 10 years to be $\sqrt{2/10} = 0.45$ of the upper limit of two years (this is plotted in Fig. 4.6 with a red line). We now see that our best fit region would be ruled out by the 10 years data set. However, this is for our assumed value of $\rho_0 = 0.36$ GeV cm^{-3} and so our GC constrained $\langle\sigma v\rangle$ contours could move up or down by about 30%.

Finally and for completeness, we present 95% CL upper limits on $\langle\sigma v\rangle$ from GC data in Fig. 3.11. Since we only used photon data in the energy range 0.3−10 GeV, we decided to compute the upper limits up to 100 GeV. We show that our derived limits are competitive with those obtained from Dwarf Galaxies, albeit with more uncertainty in the systematic error.

3.5 Discussion

We find that when we include only statistical error bars in our band analysis, we get best fits and errors that are a good match to using the Fermi Science Tools with the same energy range. This is a good check that our band analysis is providing an accurate representation of the data.

Using our band analysis, we could evaluate the equivalent of a TS value which includes the TS value by subtracting in eq:Csyst with $F_i^{\rm fit}$ set to the best fit value from with $F_i^{\rm fit} = 0$. Although in this case, as the $F_i^{\rm fit} = 0$ is so far from the best fit, the Gaussian approximation, implicit in our use of the band analysis, would be expected to break down.

Although, the $\tau^+\tau^-$ only case may have $TS \gg 25$, as can be seen from Figs. 3.7 and 3.10, it does not provide a good fit to the data. Hooper & Linden [2011a] and Abazajian & Kaplinghat [2012a, 2013] provide analysis of the $\tau^+\tau^-$ as an acceptable model. Although, we agree the $\tau^+\tau^-$ with $M \approx 10$ GeV does provide a good TS value, we have shown it provides a poor fit to the data. Similarly, as can be seen from Fig. 4.6, a pure lepton spectrum does not provide a good fit to the data. However, as can be seen from Figures 4.6, 3.7, and 3.10, a $b\bar{b}$ only spectrum does provide a good fit. In Abazajian & Kaplinghat [2012a, 2013], they

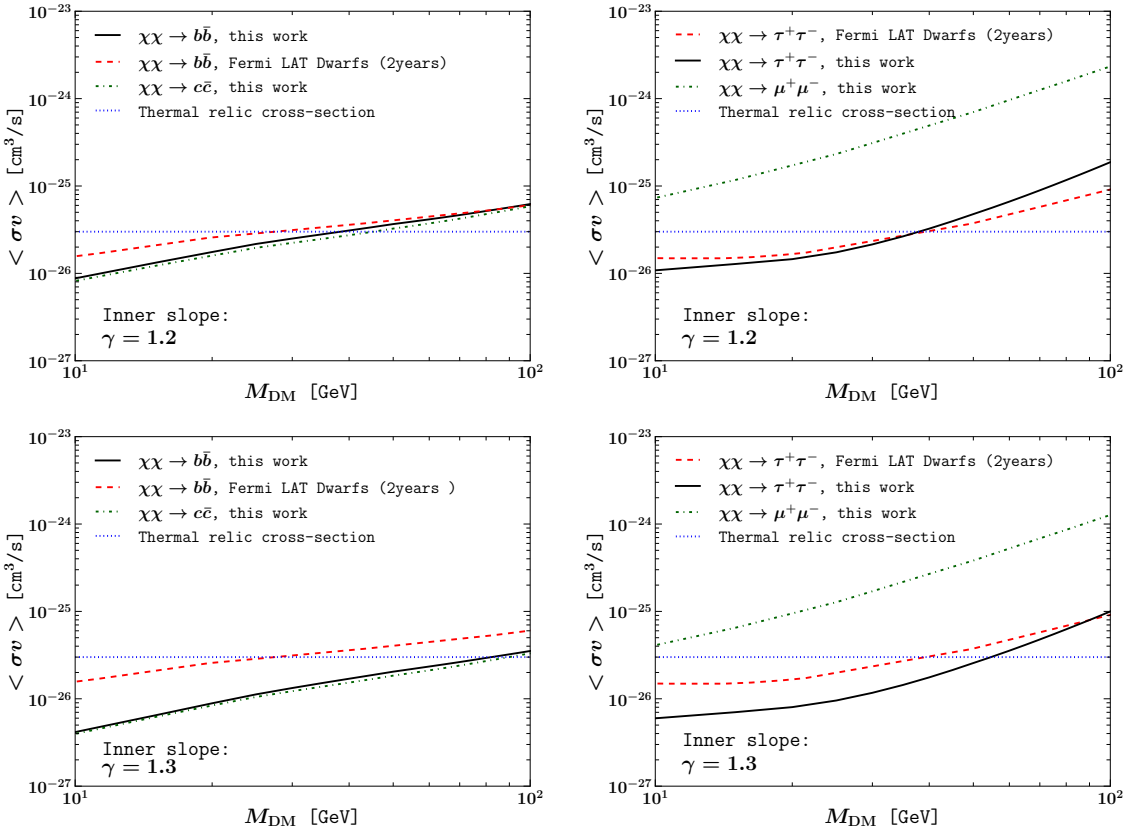

Figure 3.11: Derived 95% CL upper limits on the velocity averaged cross-section for various annihilation channels: 100% $b\bar{b}$, 100% $c\bar{c}$, 100% $\tau^+\tau^-$ and 100% $\mu^+\mu^-$. The horizontal dotted blue line denotes the thermal decoupling cross-section expected for WIMPs particles. Shown for comparison are the upper limits on $\langle\sigma v\rangle$ obtained from the analysis of Dwarf Galaxies in [Ackermann et al., 2011b]. Limits are obtained from the analysis of 3.8 years of GC photon data in the energy range 0.3−10 GeV. `Upper panel`: Assumes a DM distribution given by a NFW profile with $\gamma = 1.2$ and $\rho(R_\odot) = 3.6$ GeV cm^{-3}. `Lower panel`: Assumes a DM distribution given by a NFW profile with $\gamma = 1.3$ and $\rho(R_\odot) = 3.4$ GeV cm^{-3}.

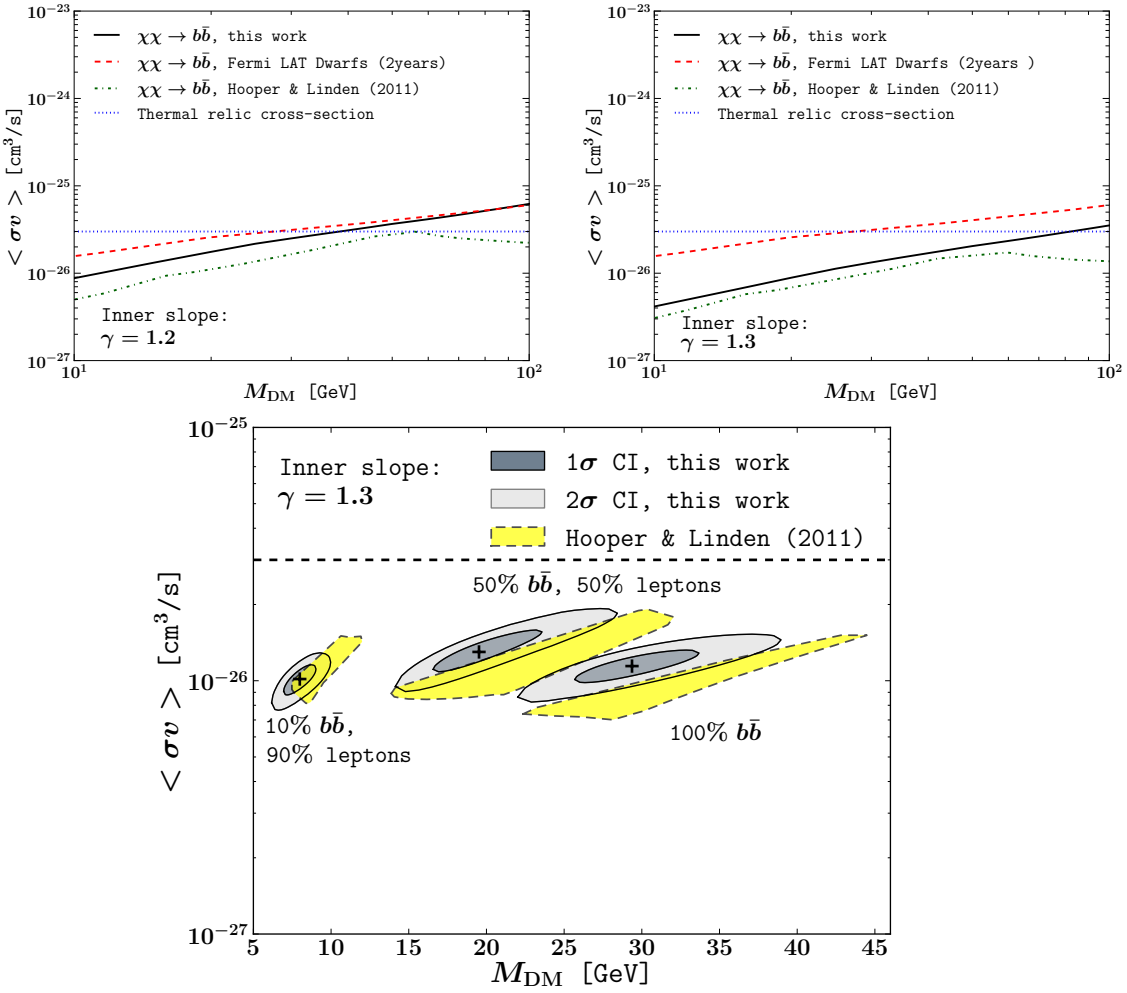

Figure 3.12: `Upper panel`: Shown are the 95% CL upper limits on the velocity averaged cross-section for 100% $b\bar{b}$ final states. The horizontal dotted blue line denotes the thermal decoupling cross-section expected for WIMPs particles. Shown for comparison are the upper limits obtained from the analysis of Dwarf Galaxies in [Ackermann et al., 2011b] and GC analysis in [Hooper & Linden, 2011a] (see more details in Fig. 3.11). `Lower panel`: Shown are the regions of the parameter space which provide a good fit to Fermi-LAT data as derived in this work (grey area) and in Hooper et al [Hooper & Linden, 2011a] (yellow area).

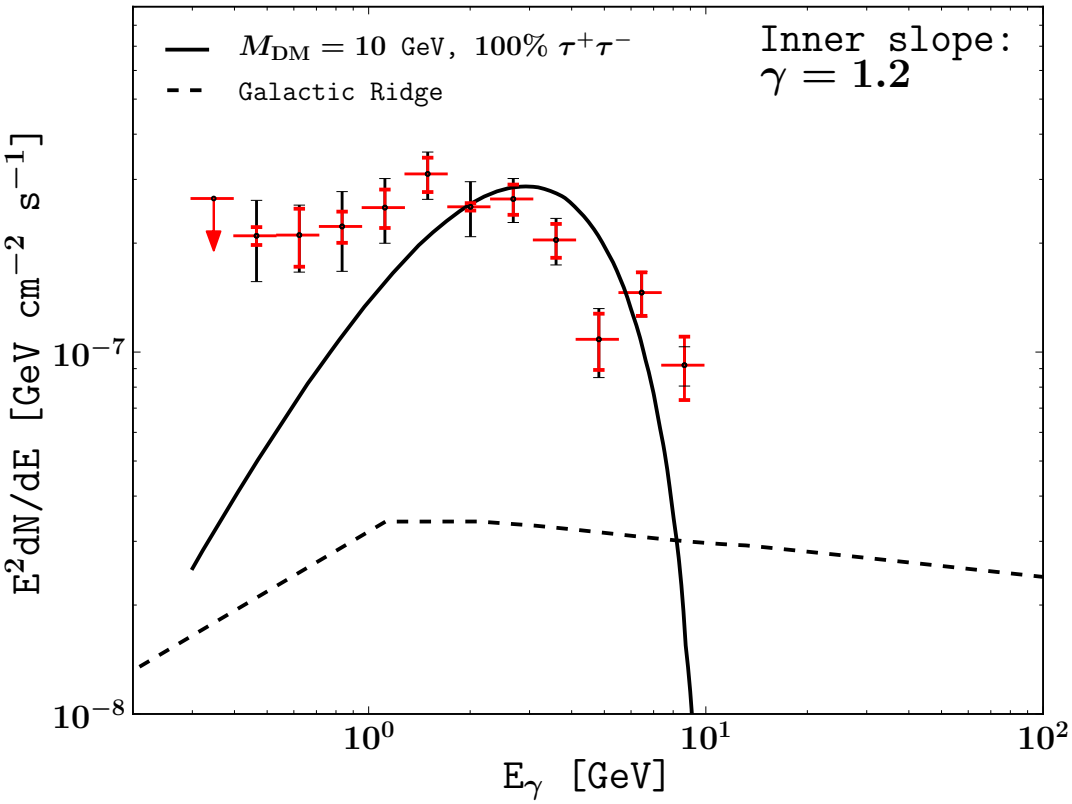

Figure 3.13: SED of the extended source assuming a NFW profile with $\gamma = 1.2$ and $\rho(R_\odot) = 0.36$ GeV cm^{-3}. The best fit spectrum obtained with $M_{\rm DM} = 10$ GeV and 100% $\tau^+\tau^-$ final states is overlaid over the twelve energy fluxes data points. Red error bars represent systematics errors and black error bars statistical errors. For illustration we also plotted the spectra of the Galactic Ridge as obtained in Fig. 7 of [Hooper & Linden, 2011a], but this source was not considered in our actual fits. See text for a discussion on this.

fit for a range of masses for a $b\bar{b}$ model. For their Fermi Science Tools analysis they find models with $10 \leq M_{\rm DM} \leq 110$ have $TS \geq 25$. Using the same data and method we have reproduced their constraints on $\langle \sigma v \rangle$ in Fermi-tools. However, as we see from Fig. 4.6, only $b\bar{b}$ models with $20 \leq M_{\rm DM} \leq 60$ GeV are within the 4σ confidence region. This shows that despite models such as $M_{\rm DM} = 10$ GeV providing a good TS value, they do not provide a good fit to the data as can also be seen in Fig. 3.7.

If the WIMP particles are Majorana fermions, then the pair-annihilation into light fermions is highly suppressed since the invariant scattering amplitude $|\mathcal{M}|^2 \propto m_f^2$ [Profumo, 2013]. Furthermore, if annihilations into gauge bosons are also suppressed and the WIMPs are lighter than the top quark then the prevailing annihilations final states are $b\bar{b}$ and $\tau^+\tau^-$. By virtue of the color charge of the bottom quarks [Profumo, 2013], one would expect the production of $b\bar{b}$ pairs to be typically more than three times larger than those of $\tau^+\tau^-$. Thus, we note that one could easily accommodate a theoretical model to these findings.

The best fit DM models, see Tables 3.2, 3.3, 3.4, Figures 4.6, and 3.10 have values for $\langle \sigma v \rangle$ intriguingly close to the simple thermal relic value. An even closer match is obtained from a more precise WIMP relic abundance cross-section of $\langle \sigma v \rangle = 2.2 \times 10^{-26}$ cm^{3}s^{-1} which has a feeble mass-dependence for masses above 10 GeV Steigman et al. [2012].

Our SEDs are designed to be of the GC extended emission component only, while those of Hooper & Linden [2011a] also include Sgr A* and a component known as the HESS ridge which we will discuss later in this section. Also, comparing our results with Hooper & Linden [2011a] is difficult as they use a profile with a slope $\rho \propto r^{-\gamma}$ rather than a generalized NFW profile as in nfw. For a generalized NFW profile the line of sight integral, J, formally extends to an infinite distance from the observer. Because of the steep drop off beyond r_s, the integral is insensitive to the actual upper bound used provided it is much larger than r_s. However, if only the inner slope is used then the J factor depends sensitively on the upper bound assumed and an upper bound of ∞ would give much too large an answer. Unfortunately, the range of the line of sight integral used for the galactic center results of Hooper & Linden [2011a] is not provided and so we are unable to reliably compare our constraints with theirs for $\langle \sigma v \rangle$. But, interestingly, our

constraints for the $\gamma = 1.3$ case are a good match with theirs, see Figs. 3.11 and 3.12. For the $\gamma = 1.3$ case, we determined ρ_0 from maximizing the likelihood of the microlensing and dynamical data (see Fig. 5 of Iocco et al. [2011]) with $\gamma = 1.3$ to be $\rho_0 = 0.34$ GeV cm^{-3}. Our ρ_0 for $\gamma = 1.2$ and $\gamma = 1.3$ match the corresponding ρ_0 in Hooper & Linden [2011a]. But, without the upper limit for their line of sight integral, it is not clear whether this match is coincidental or not. Note that in the upper-limits plot of Fig. 3.12, the match is not as good for $M_{\rm DM} > 100$ GeV but this likely due to in their corresponding plot they use their 10 to 100 GeV bin and for $M_{\rm DM} > 100$ GeV the DM spectrum significantly overlaps with that region.

For $\gamma = 1.2$ the match is not as good, see Fig. 3.12. As Fig. 3.2 shows the inner PSs are very degenerate with the excess emission component and in the GC analysis of Hooper & Linden [2011a] they use the 2FGL parameters for all the PSs except Sgr A* which they fit a PS to the data without an GC excess emission component. Their Sgr A* fit (see Fig. 4 of Hooper & Linden [2011a])is very similar to ours for the baseline model in Fig. 3.2. They do use a broken power law parametrization rather than a Log Parabola, but that difference has a negligible effect. So their analysis does not utilize the degeneracy between the PSs, especially Sgr A*, and the GC excess emission component. This implies the analysis of Hooper & Linden [2011a] will have a suppressed dark matter $\langle \sigma v \rangle$ when compared to ours.

In [Hooper et al., 2012] they do use a generalized NFW profile, but there they do not account for Sgr A* as they are seeking a robust upper limit to the DM cross-section. They also choose values of γ and ρ_0 consistent with the microlensing and dynamical data Iocco et al. [2011] but chosen to be conservative with respect to a potential dark matter annihilation signal. Consistent with this, their upper limits are larger than ours. Also, again the match is more discrepant for $M_{\rm DM} > 100$ GeV but this likely due to them using the 10 to 100 GeV data range and for $M_{\rm DM} > 100$ GeV the DM spectrum significantly overlaps with that energy region.

In the GC analysis of Hooper & Linden [2011a], they investigate adding a HESS Galactic ridge component Aharonian et al. [2006]. The 2 by 1 degree HESS Galactic ridge was measured by HESS over the energy range 0.2 to 10

TeV. It was found to be spatially correlated with the molecular clouds in the central 200 parsec of the Milky Way. Its origin is usually taken to be the decays of neutral pions produced in the interactions of harder than usual population of cosmic ray protons and nuclei with the surrounding molecular gas. In Hooper & Linden [2011a] they evaluate the spectrum for this model at energies less than 100 GeV and use this in their model fit. We study this in great detail in the next chapter.

As can be seen from Fig. 3.13, the HESS ridge postulated by Hooper & Linden [2011a] should not significantly effect the fit in our case. This is because we are using $\gamma = 1.2$ that leads to a higher inferred DM flux and also we are refitting our PSs which allows the DM flux to be higher by lowering the emission of the PSs close to the GC.

The GC excess emission results of Hooper & Slatyer [2013] are quoted as being derived from a generalized NFW which is effectively equivalent to the one we are using for $\gamma = 1.2$, albeit with a density of $\rho_0 = 0.4$ GeV/cm^3. But, as they are not simultaneously fitting their PS and DM models, this is likely to explain why they find a significantly smaller value for $\langle \sigma v \rangle = 8 \times (0.4/0.36)^2 \times 10^{-27} = 9.9 \times 10^{-27}$ cm^3 s^{-1} for the $M_{\rm DM} = 50$ GeV (100% $b\bar{b}$) case for $\gamma = 1.2$. Where we have converted their value to the equivalent value for our assumed local density. As can be seen from the top left plot in Fig. 4.6, this is outside our 5σ confidence region. However, if instead of taking the best fit ρ_0 from the microlensing and dynamical data (see Fig. 5 of Iocco et al. [2011]), one sees how the result changes if one takes the contour 68% limits, $\rho_0 \in [0.3, 0.4]$, the error for $\langle \sigma v \rangle$ becomes of order 20% taking into account the ρ_0^2 dependence of the J factor shown in J. However, this is only important in estimating $\langle \sigma v \rangle$ and does not affect statements like a 10 GeV DM annihilating only to $\tau^+\tau^-$ does not provide a good fit to the Fermi-LAT data, as the goodness of fit to the gamma-ray data is independent of $\langle \sigma v \rangle$ due to the complete degeneracy between $\langle \sigma v \rangle$ and ρ_0^2.

In Hooper & Linden [2011a], they state that they include the observed spatial variations of the residuals as a systematic error. Details are not given on the magnitude. While in an earlier related paper Hooper & Goodenough [2011] a value of 3% is given. By varying the parameters used in GALPROP for the distribution of cosmic-rays, interstellar gas and radiation fields, the Fermi-LAT

team reported a systematic error of order 10% for the inner Galaxy and for energies less than 10 GeV with unresolved point sources being cited as a likely cause Ackermann et al. [2012a]. Boyarsky et al. [2011] found systematic errors of about 10% in a 2° around the GC by doing Monte Carlo simulations of a model with no GC diffuse source. Thus, overall our estimate of 20% is higher than other estimates.

Our confidence regions for MSPs are in good agreement with the average pulsar spectrum measured by Fermi-LAT, see Fig. 3.8. For the pulsar hypothesis, it is interesting to evaluate the number of MSPs needed to account for the excess emission. For an energy range of 100 MeV to 10 GeV, Abdo et al. [2009] found 47 Tuc had a flux of $2.6(\pm 0.8) \times 10^{-8}$ photons cm^{-2} s^{-1}. The population of MSPs in 47 Tuc is taken to be 30 to 60. Following Abazajian & Kaplinghat [2012a, 2013] we then use this to estimate the order of magnitude of the flux of a single MSP to be $\sim 10^{-9}$ ph cm^{-2} s^{-1}. The flux of our best fit exponential cutoff in the energy range 100 MeV to 10 GeV is obtained by integrating the parametric form eq:expcut with the best fit parameters quoted in Sec. 3.4.1 and is found to be 1.7×10^{-6} ph cm^{-2} s^{-1}. Therefore we find the number of MSPs needed to explain the GC excess emission to be ~ 1000 which is compatible with what Abazajian & Kaplinghat [2012a, 2013] found as our flux estimates of the GC excess are compatible with theirs.

However, if the excess extended emission was also responsible for the bulk of the low latitude, low energy emission of the Fermi Bubbles as suggested in Hooper & Slatyer [2013], the spectral and spatial properties typical of a population of MSPs would not be a good fit to the signal Hooper et al. [2013b].

Abazajian & Kaplinghat [2012a, 2013] also examined a proposal by Yusef-Zadeh et al. [2013] which entails high energy cosmic ray electrons producing bremsstrahlung gamma-rays on molecular gas. This case can have significant extent to the spatial emission. Yusef-Zadeh et al. [2013] finds that the source electron population is consistent with radio observations of synchrotron emission from the high energy population of electrons, as well as the morphology of the FeI 6.4 keV X-ray emission. Abazajian & Kaplinghat [2012a, 2013] find that using the radio emission morphology, tracing the synchrotron emission from the cosmic ray electrons improves the fit over the base model with a TS=252 for an energy

range of 1 to 100 GeV. But this was significantly smaller than what they obtained for a Log Parabola spectrum for the same energy range which gave TS=412.

This indicates that the bremsstrahlung model may not be providing a good fit, in much the same way as we have found $\tau^+\tau^-$ has a good TS but not as good as $b\bar{b}$ which was a good fit.

3.6 Conclusions

We have found that either a DM annihilation model or unresolved pulsar population is consistent with the observed excess gamma ray emission seen in the GC. Our analysis marginalized over the PS and diffuse background amplitudes in the region of interest. We included an estimated systematic error for the diffuse galactic background of about 20%. We provide confidence regions for the model parameters.

Importantly, by measuring the gamma-ray spectrum we showed that it would be hard to explain the data with only prompt emission from a pure leptophilic model, we demonstrated that WIMPs models with branching ratios near 100% in the $\tau^+\tau^-$ channel are ruled out at 5σ if the effects of diffusion of the resulting secondary leptons are not considered. However, as subsequently shown by Lacroix et al. [2014], the effects of diffusion and other secondary leptons can make the $\tau^+\tau^-$ channel acceptable. This has a negligible effect on the $b\bar{b}$ channel. Notwithstanding we found that the average measured Fermi-LAT millisecond pulsar spectrum was also a good fit. In fact, our analysis showed that a superposition of $\sim 10^3$ millisecond pulsars (MSPs) within a radius of $r \lesssim 150$ pc of the Galactic Center whose number density follows a generalized NFW profile was also strongly favored by the data.

Chapter 4

Contribution of cosmic rays interacting with molecular clouds to the Galactic Center gamma-ray excess

4.1 Introduction

In the previous chapter 3 we explored the possibility that the Galactic Center excess gamma rays (GCEG) were mainly due to either DM or a population of $\sim 10^3$ MSPs. However, another possibility is that the signal is being produced by cosmic rays interacting with gas in the Galactic Center Goodenough & Hooper [2009a]; Hooper & Linden [2011a]; Linden et al. [2012a]; Yusef-Zadeh et al. [2013]. This alternative solution can be divided in two different scenarios, the hadronic and nonthermal bremsstrahlung. The first one consists of π^0-decays resulting from the emission of high energy protons and their subsequent collision with gas in the Galactic Center. In Linden et al. [2012a] it was found that a model based on hadronic emission from Sgr A* would be determined predominately by the gas distribution and would appear point-like to the Femi-LAT gamma-ray detector. Therefore, that model would not be suitable for explaining the extended nature of the GCEG.

In the second scenario, the nonthermal bremsstrahlung emission model, a case which results in extended emission has been proposed by [Yusef-Zadeh et al., 2013]. Based on multi-wavelength observational data obtained with the Green Bank Telescope (GBT) Law et al. [2008], Susaku, X-ray Multi-Mirror Mission (XMM)-Newton, Chandra, Fermi-LAT and High Energy Stereoscopic System (HESS) it was argued [Yusef-Zadeh et al., 2013] that the ∼GeV GCEG is nonthermal, diffuse and is probably generated by a population of synchrotron emitting electrons interacting with gas in molecular clouds.

In this chapter we focus on the spatial and spectral morphology of the gamma-ray Galactic Ridge (hereafter "Galactic Ridge") region, and confirm that an extended source associated with the Galactic Ridge can improve the GCEG fit (notice that we made some preliminary investigations on this in the previous chapter 3). But, we find that adding a Galactic Ridge does not remove the need for also adding a spherically symmetric extended source whose radial profile follows a $\mathrm{NFW}^2_{1.2}$ profile. We show that the spectral parameters of the $\mathrm{NFW}^2_{1.2}$ template are not significantly affected by inclusion of a Galactic Ridge.

4.2 Data Reduction

The Fermi-LAT data selection is the same as described in Chapter 3. In summary, we analysed Pass-7[1] data taken within a squared region of $7^\circ \times 7^\circ$ centred on Sgr A* in the first 45 months of observations over the period August 4, 2008−June 6, 2012. We used the standard data cuts and kept only the `SOURCE` class events which have a high probability of being photons of astrophysical origin. We also selected events between 200 MeV−100 GeV without making any distinction between *Front* and *Back* events.

The spectra were obtained by maximizing the likelihood of source models using the binned *pyLikelihood* library in the Fermi Science Tools. We followed the same fitting procedure adopted in [Abazajian & Kaplinghat, 2012a, 2013] which has been recommended to be more suitable for crowded regions like the Galactic Center. Unless otherwise stated, the models included all sources suggested in the

[1]Preliminary checks have shown our results are not significantly changed if we instead use Pass-7 reprocessed data.

2FGL [Nolan, 2012] catalog plus the LAT standard DGB and extragalactic background models `gal_2yearp7v6_v0.fits` and `iso_p7v6source.txt` respectively.

4.3 Models for the Extended Source at the Galactic Center

The HESS telescope has revealed a point-source coinciding with the dynamical center of the Milky Way Galaxy as well as diffuse emission that is spatially correlated with the molecular clouds in the Galactic Ridge Aharonian et al. [2006]. In [Yusef-Zadeh et al., 2013] it was argued that bremsstrahlung from nonthermal electrons in Galactic Center molecular clouds can explain the GCEG measured at TeV scales by HESS and at GeV scales by Fermi-LAT. The non-thermal electrons in the molecular clouds are proposed to mainly come from supernova remnants and nonthermal radio filaments (see [Law et al., 2008; Yusef-Zadeh et al., 2013] and references therein). A proposed population of nonthermal electrons is constrained, by both radio and gamma-ray data, to need a broken power law spectrum where the break is attributed to rapid cooling of electrons at high energies [Yusef-Zadeh et al., 2013]. By comparing the frequency of the break in the radio data and the energy of the break in the gamma-ray data, the magnetic field value can be constrained, see Sec. 4.5.

The TeV nonthermal electrons, proposed to explain for the HESS Galactic Ridge, are assumed to be a separate younger population of nonthermal electrons in the Galactic Center molecular clouds. This extra population is assumed to have not had time to cool and so is modeled with a power law distribution [Yusef-Zadeh et al., 2013].

To study the evidence for a new component of extended GeV emission in the Fermi-LAT data, the authors in [Yusef-Zadeh et al., 2013] tried spatial templates obtained from X-ray, 20-cm continuum emission radio data, and the HESS residuals. For a spectral model they initially employed a broken power law of the form:

$$\frac{dN}{dE} = N_0 \times \begin{cases} \left(\frac{E}{E_b}\right)^{-\Gamma_1} & \text{if } E < E_b \\ \left(\frac{E}{E_b}\right)^{-\Gamma_2} & \text{otherwise.} \end{cases} \tag{4.1}$$

They found that the 20-cm radio and HESS residual templates had similar high test statistic (TS) values.

For illustration, we show in Fig. 4.1 the HESS residual and 20-cm spatial templates. The 20-cm template was based on GBT continuum emission data which measures nonthermal and thermal plasma distributions [Law et al., 2008; Yusef-Zadeh et al., 2013]. Note, this is distinct from the 21-cm line temperatures used by the Fermi team in constructing the DGB as that gives a measure of the column density [Diffuse & Collaboration, 2009]. Both templates initially had a DC value, evaluated from a nearby region, subtracted. They have also had Sgr A removed and they have been normalized so that their total area integrated flux is unitary.

To test whether the GCEG is better fitted by a combination of a $\mathrm{NFW}^2_{1.2}$ template and a Galactic Ridge template we have done a broad band analysis within the Fermi Tools and also a bin-by-bin analysis for each of the extended sources under scrutiny.

4.4 Systematic errors and parameter constraints

The DGB accounts for a large proportion of the photons detected by the LAT instrument. For regions near the Galactic Center this component can be several orders of magnitude brighter than any other source. In particular, the dominant systematic error at energies $\sim$1 GeV emerges from the uncertainties in the DGB model. These systematics were studied in a previous analysis (Chapter 3).

Since this work involves the analysis of an extra extended source (see section 4.3) not considered in Chapter 3, we have reassessed the systematic errors in the DGB by following the same approach explained in Chapter 3. There is consistency between the present and previous analysis Chapter 3, we found that the overall systematic flux error is energy and spatial dependent: systematic errors due to uncertainties of the spectral distribution amounts to an average of about 2% at $\sim$1 GeV, and the dominant fraction for the systematics arises from the spatial part, we obtained on average about 23% for energy bins $\leq$ 10 GeV and 18% in the 10$-$100 GeV energy band. The total systematic error is evaluated by summing in quadrature the spatial, spectral, and effective area [Nolan, 2012]

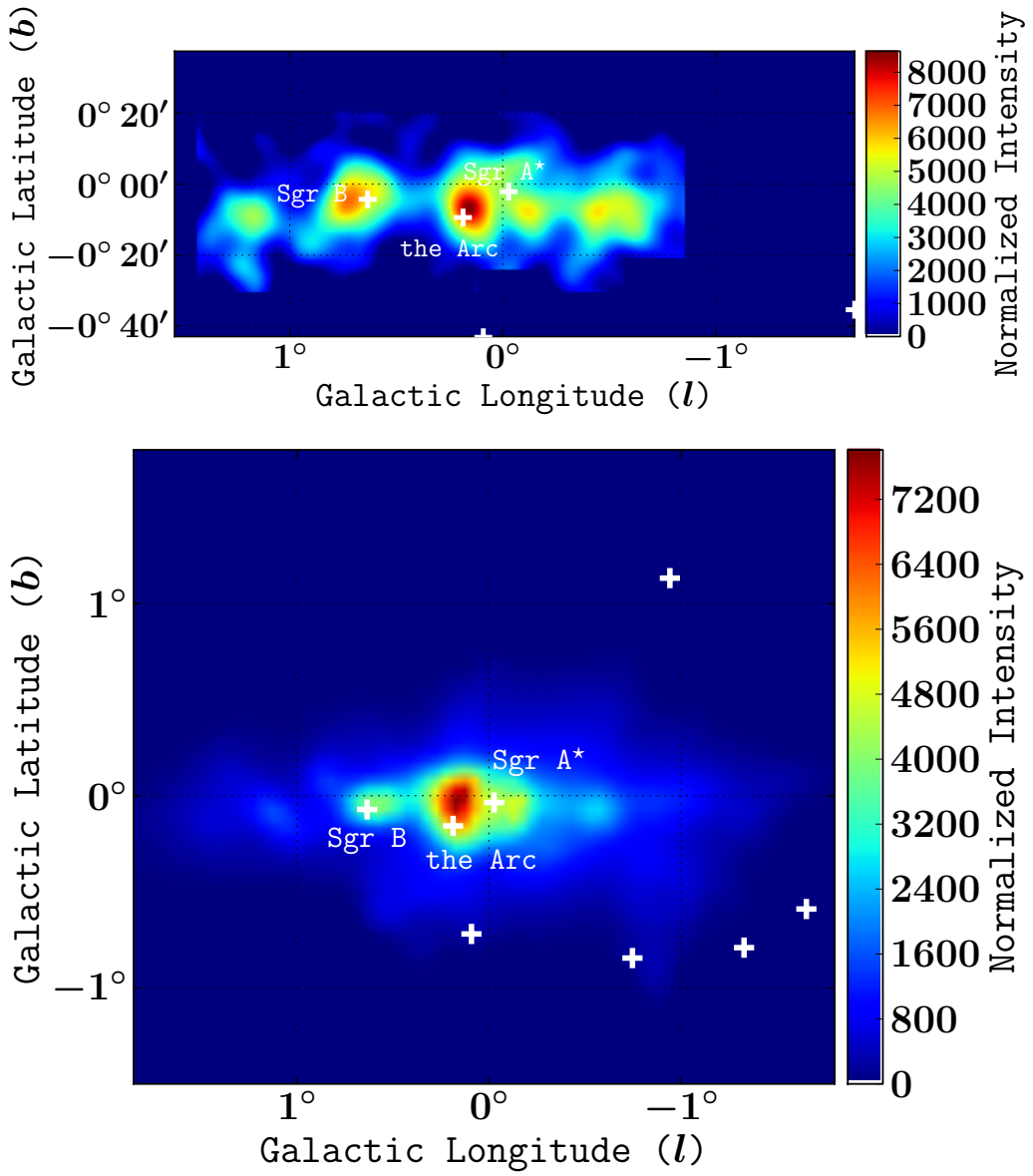

Figure 4.1: *Top:* Gamma-ray image of the Galactic Center as observed by the HESS telescope ($E > 380$ GeV) after subtracting the dominant point sources [Aharonian et al., 2006]. To include this template map in the likelihood function within the Fermi Science Tools package, we background subtracted, thresholded and normalized the data provided in [Aharonian et al., 2006]. *Bottom:* Background-subtracted, thresholded, and normalized image from 20-cm continuum emission GBT data. This template was the same one as used in [Yusef-Zadeh et al., 2013] and we refer the reader to that article for details[1]. This spatial template is named the "20-cm template" in the rest of this work. The crosses overlaid on the image represent the position of the 2FGL catalog point sources.

systematic errors (see Chapter 3).

Our parameter constraints method is the same as used in Chapter 3. In summary we use the Fermi Tools to construct a spectrum of the source of interest [Nolan, 2012]. As in . [Nolan, 2012] and Chapter 3, we allow the amplitude of all sources, in the region of interest, to vary when fitting a band. We then add, in quadrature, the systematic errors (evaluated as described above) to the statistical errors of the spectral bands. The spectrum likelihood is then approximated as a multivariate Gaussian and a profile likelihood approach is used to construct confidence intervals.

In plotting the spectra we display both the systematic and statistical errors. For bands which have a test statistic (TS) [Nolan, 2012] less than 10, or whose total error is more than the half of the best fit band value, we plot the 95% upper limit. We do not plot or use bands in our parameter constraints which have TS<1. Unless otherwise stated, best fit parameter values are quoted with 68% confidence intervals.

To cross-check the systematical errors explained above, we have also estimated the systematic uncertainties in the DGB following the interesting analysis technique utilized in [Ackermann et al., 2012a]. We constructed eight different diffuse emission models using GALPROP [Strong & Moskalenko, 1998; Vladimirov et al., 2011], and each of these templates were included in the likelihood fit of the sources of interest as an alternative to the standard DGB recommended in the 2FGL catalog [Nolan, 2012].

The set of alternative DGB models taken into account in this analysis consider a range of possible values for the input parameters that were found to exhibit the largest sensitivities [Ackermann et al., 2012a]. The parameters varied in the models are the cosmic ray propagation halo heights (4 kpc or 10 kpc), cosmic ray source distribution (supernova remnants or pulsars) and the atomic hydrogen spin temperature (150 K or optically thin). An $E(B-V)$ magnitude cut of 5 mag was also chosen. The results obtained through this method are displayed as grey shaded areas in the spectra of Fig. 4.2.

The DGB provided with the Fermi Tools is generated by a weighted sum of gas column densities and an inverse Compton intensity map [Diffuse & Collaboration, 2009]. In the DGB generation, the weights depend on the energy band and

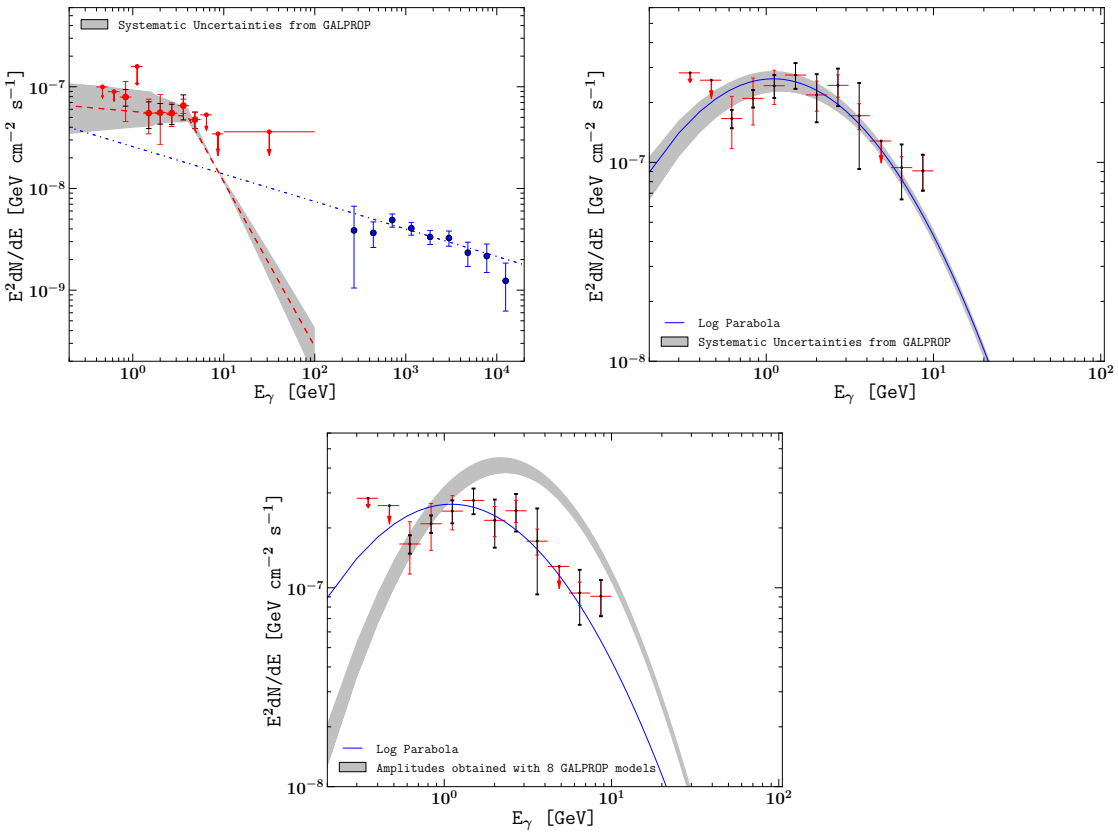

Figure 4.2: *Top Left:* Galactic Ridge spectrum generated from model 2 in Table 4.1. The red dashed line shows the best fit broken power-law as obtained from a Fermi Tools broad band fit. The grey area is an estimate of the systematic uncertainties as calculated with 8 different GALPROP models of the DGB. Black and red error bars are the LAT (1σ) statistical and systematic errors. A red arrow indicates a 95% upper limit. The blue points correspond to data taken by HESS Aharonian et al. [2006] and the blue dotted line is the best fit power law to them. *Top Right:* spectrum for $\mathrm{NFW}^2_{1.2}$ spatial profile generated with model 1 in Table 4.1. The blue solid line is the best fit Fermi tools log parabola spectrum. The grey area shows the systematic uncertainties as computed with 8 different GALPROP models of the DGB. The spectra and error bars are listed in Table 4.5 and 4.6. *Bottom Center:* Same as top right, except the GALPROP based model results are shown rather than just the relative errors obtained from them.

the gas template weights also depend on the ring radius concentric around the Galactic Center. The weights are fitted to all sky Fermi-LAT data. Due to the greater degree of freedom this method produces a better fit to the Fermi-LAT data than the GALPROP based approach described above. So in general the GALPROP simulations do not envelope the solution found using the standard DGB. Therefore we use the relative dispersion of the GALPROP simulations in constructing the grey bands in the top panels of Fig 4.2. In the bottom panel of Fig 4.2 we plot the band of solutions obtained when the GALPROP DGB's are used. In this panel, the $\mathrm{NFW}^2_{1.2}$ template has a greater amplitude as the GALPROP estimate of the DGB is not as good a fit as the standard DGB provided with the Fermi Tools.

4.5 Results

As seen from Fig. 4.1, the Arc and Sgr B are bright sources in the Galactic Center. They are thought to be associated with cosmic rays interacting with molecular clouds [Yusef-Zadeh et al., 2013] and so in Table 4.1 we consider models with and without them being assumed to be included in the Galactic Ridge template.

The results listed in Table 4.1 show that the broad band analysis revealed significant detections of both a Galactic Ridge and a $\mathrm{NFW}^2_{1.2}$ extended source.

The need for the Galactic Ridge can be seen in the residuals shown in Fig. 4.3. It is particularly noticeable in those bands which have a high TS (see Table 4.6).

Based on the GBT radio data, [Yusef-Zadeh et al., 2013] set the synchrotron flux at 325 MHz to be $F_{325} = 508$ Jy and a synchrotron spectrum of electrons of the form E^{-p} with $p = 1.5$ below the break frequency $\nu_b = 3.3$ GHz and $p = 4.4$ above it. The GCEG spectrum can be used to constrain the break energy for the electron spectrum (E_b) via Eq. 16. This can be converted to a constraint on the magnetic field strength B by using the measured radio frequency spectral break ν_b and the general relation between electron energy and characteristic synchrotron radio frequency given in Eq. 7. The GBT uncertainties for the spectral slopes, ν_b, and F_{325} were not given in Yusef-Zadeh et al. [2013] and so our analysis just includes their point estimates.

Fitting the bremsstrahlung model (Eq. 16), we varied the number density

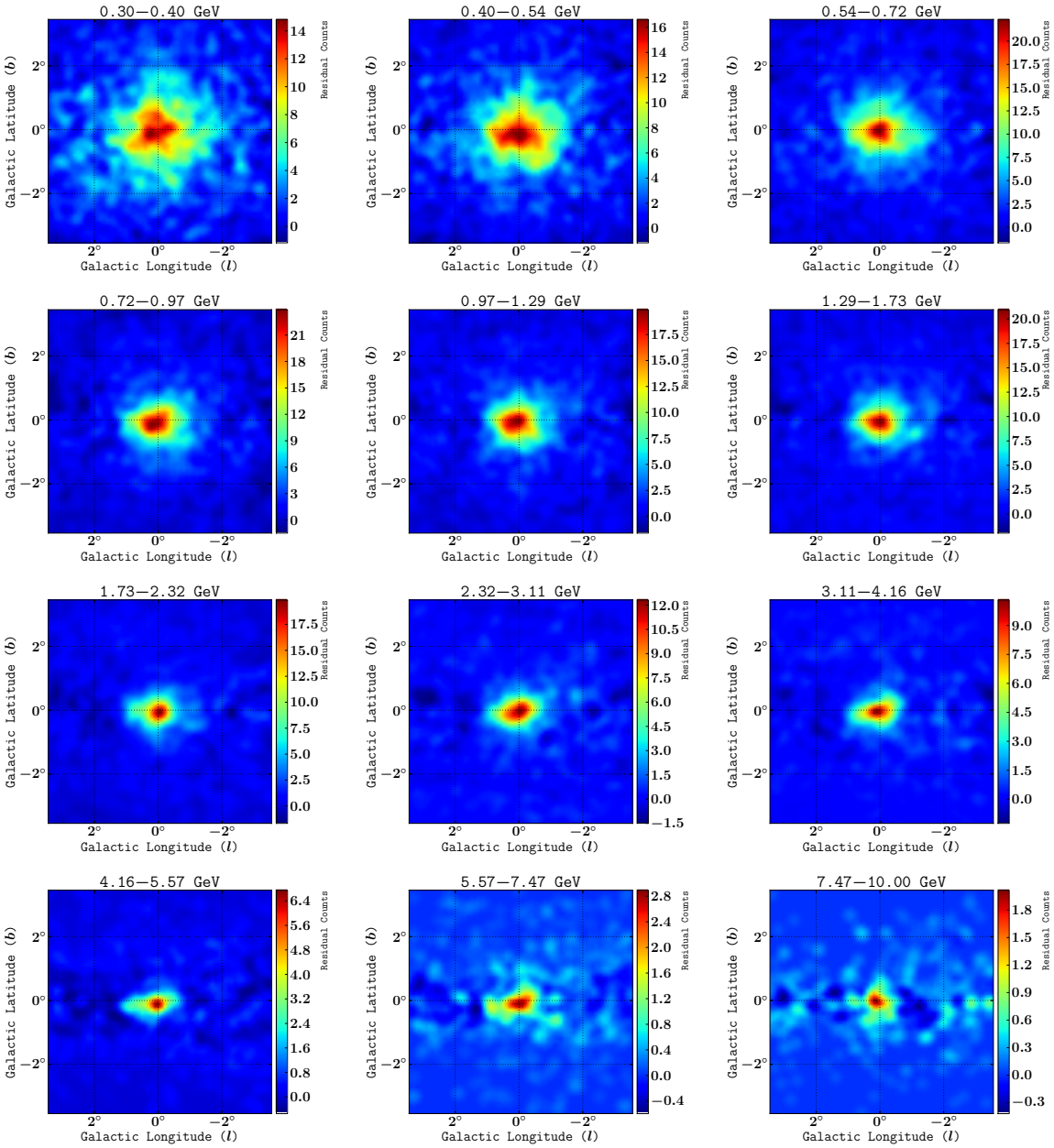

Figure 4.3: Shown are the residuals of model 2 in Table 4.1 where the model components of the $\mathrm{NFW}^2_{1.2}$ and the 20-cm Galactic Ridge have not been subtracted from the data. The images have been smoothed with a 0.3° radius Gaussian filter.

Model	$2\log(\mathcal{L}/\mathcal{L}_{\rm base})$	dof−dof$_{\rm base}$
Base (2FGL−"the Arc"−Sgr B)	0	0
2FGL	425	4+5=9
2FGL+20-cm template	638	4+5+4=13
2FGL+NFW$^2_{1.2}$	1295	4+5+3=12
2FGL+NFW$^2_{1.2}$ + HESS residual template	1325	4+5+3+4=16
2FGL+NFW$^2_{1.2}$ + 20-cm template (**model 1**)	1330	4+5+3+4=16
Base+NFW$^2_{1.2}$ + HESS residual template	1164	3+4=7
Base+NFW$^2_{1.2}$ + 20-cm template (**model 2**)	1170	3+4=7

Table 4.1: The likelihoods evaluated in compiling the above table are maximized with a broad band analysis using the Fermi Tools. Alternatives models of the Galactic Center in the 200 MeV−100 GeV energy range are listed. Each point source in the model has degrees of freedom (dof) from its spectrum and two extra dof from its location. The spectra for the Galactic Ridge templates are modeled by a broken power law. While the spectra for the NFW$^2_{1.2}$ templates are modeled by a log parabola which has enough flexibility to mimic a good fitting DM or MSP spectra Chapter 3.

of hydrogen nuclei n_H and the magnetic field B. We simultaneously fit the normalization and slope of the power-law formula corresponding to the TeV HESS data. Using a bin-by-bin analysis we made a parameter scan as shown in Fig. 4.4 and Table 4.2.

$n_{\rm H}$ [cm^{-3}]	B [μG]	N_0 [ph cm^{-2} s^{-1} MeV^{-1}]	Γ
5^{+6}_{-3}	6^{+3}_{-2}	$(2 \pm 1) \times 10^{-11}$	$2.25^{+0.07}_{-0.08}$

Table 4.2: Best fit values obtained in the bremsstrahlung analysis for the gas number density ($n_{\rm H}$), the magnetic field (B), and the HESS power law spectrum amplitude (N_0) and spectral index (Γ). The best fit spectra and data fitted to are shown in the LHS panel of Fig. 4.4.

Additionally, this analysis enabled us to study to what extent the Galactic Ridge component affects the model parameters of a DM or unresolved MSPs extended source. We therefore made a detailed parameter scan corresponding to the DM and MSPs hypotheses in models which included a Galactic Ridge. The

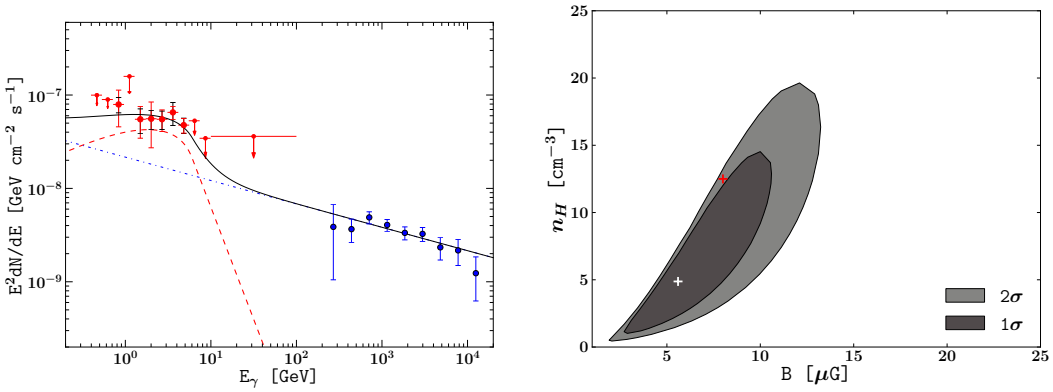

Figure 4.4: *(Left)* Red filled circles show the Fermi-LAT Galactic Ridge energy flux points obtained under the assumption of Model 2 in Table 4.1. They are listed in Table 4.6. The blue circles represent the Galactic Ridge as measured by the HESS telescope Aharonian et al. [2006]. Black and red error bars show statistical and systematic errors respectively. Red arrows show 2σ upper limits. The red dashed curve is the gamma-ray nonthermal bremsstrahlung model generated from Eq. 16. The blue dotted line is a nonthermal bremsstrahlung model represented by a power law. The black solid line is the sum of the red dashed curve and blue dotted line. It gives the best fit to the combined Fermi-LAT and HESS Galactic Ridge data. *(Right)* Confidence regions generated from the data and models shown in the left panel. The parameter n_H is the number density of hydrogen nuclei and B the magnetic field. The white cross shows our best-fit values while the red cross corresponds to the values found in [Yusef-Zadeh et al., 2013]. See also Table 4.2.

dark matter spectra are obtained using DMFIT [Jeltema & Profumo, 2008] while the standard exponential cut off form is used for the MSPs' spectrum:

$$\frac{dN}{dE} = K \left(\frac{E}{E_0}\right)^{-\Gamma} \exp\left(-\frac{E}{E_{\rm cut}}\right), \tag{4.2}$$

where photon index Γ, a cut-off energy $E_{\rm cut}$ and a normalization factor K are free parameters. The results are summarized in Fig. 4.5 and Table 4.3 for the MSPs hypothesis, and Fig. 4.6 and Table 4.4 for the DM hypothesis.

Model	$E_{\rm cut}$ [GeV]	Γ	G_{100} [10^{-9} erg cm^{-2} s^{-1}]
MSPs	4^{+2}_{-1}	1.6 ± 0.2	1.5 ± 0.2
MSPs + Galactic Ridge	3^{+2}_{-1}	1.4 ± 0.3	$1.2^{+0.2}_{-0.1}$

Table 4.3: Best-fit values for MSPs hypothesis. The spectrum of the MSPs is fitted with a power law with an exponential cut off (see Fig. 4.5). The first row shows the result from an analysis without a galactic ridge (Chapter 3). The second row parameters were fitted to the spectral data plotted on the top RHS panel of Fig. 4.2. The GCEG energy flux for 100 MeV$\leq E \leq$ 100 GeV is denoted by G_{100}.

Model	Best-fit Branching ratio	$\langle\sigma v\rangle$ [cm^3/s]	$M_{\rm DM}$ [GeV]
DM	$(60 \pm 20)\%$ $b\bar{b}$	$(2.8 \pm 0.4) \times 10^{-26}$	24 ± 7
DM + 20-cm template	$(80 \pm 20)\%$ $b\bar{b}$	$2.0^{+0.5}_{-0.6} \times 10^{-26}$	27^{+8}_{-9}

Table 4.4: Best-fit values for the branching fraction between $b\bar{b}$ and $\tau^+\tau^-$, DM velocity averaged annihilation cross section and DM mass. DMFIT was used to generate the model spectra [Jeltema & Profumo, 2008]. The first row shows the result from an analysis without a Galactic Ridge Chapter 3. The second row parameters were fitted to the spectral data plotted on the top RHS panel of Fig. 4.2.

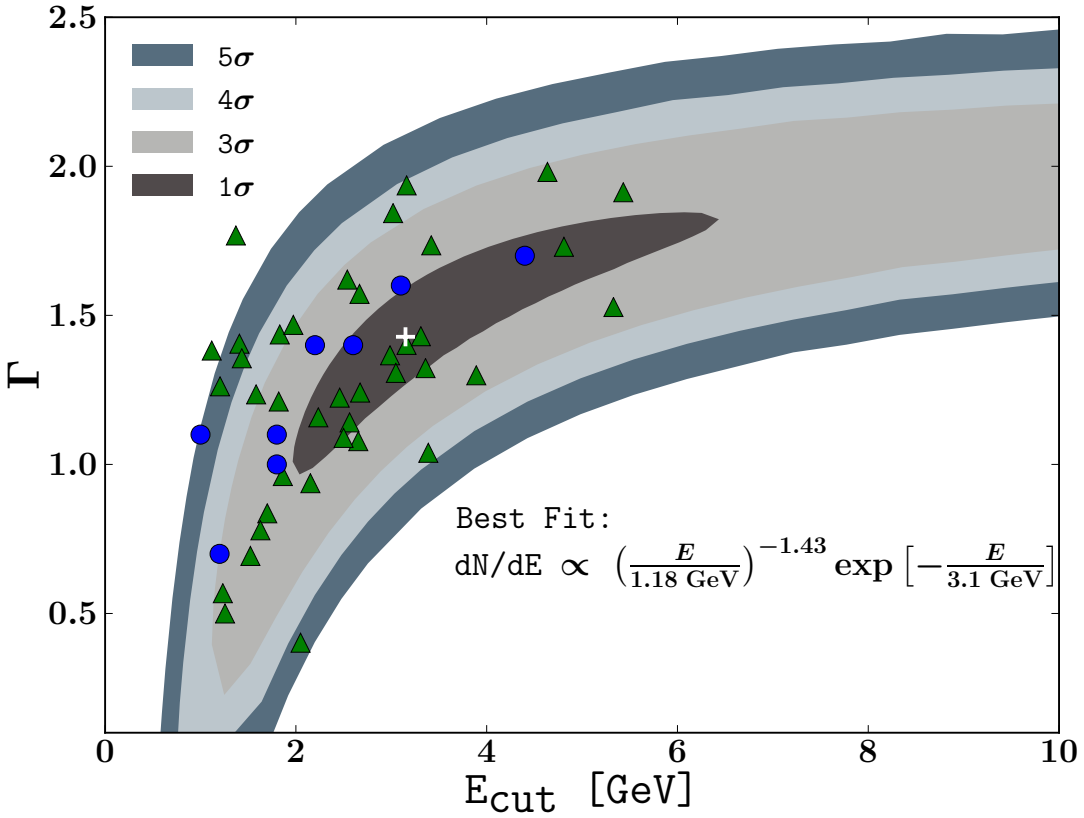

Figure 4.5: Confidence regions for an unresolved population of MSPs when the Galactic Ridge was included in the fit. The data used is shown in the top RHS panel of Fig. 4.2 and listed in Table 4.5. The best fit is denoted by a white cross. The green triangles show the best fit parameters of the MSPs detected in the second Fermi LAT catalog of gamma-ray pulsars (2FPC) [Abdo et al., 2013]. The blue circles represent the best fit parameters of MSP populated globular clusters [Abdo et al., 2010].

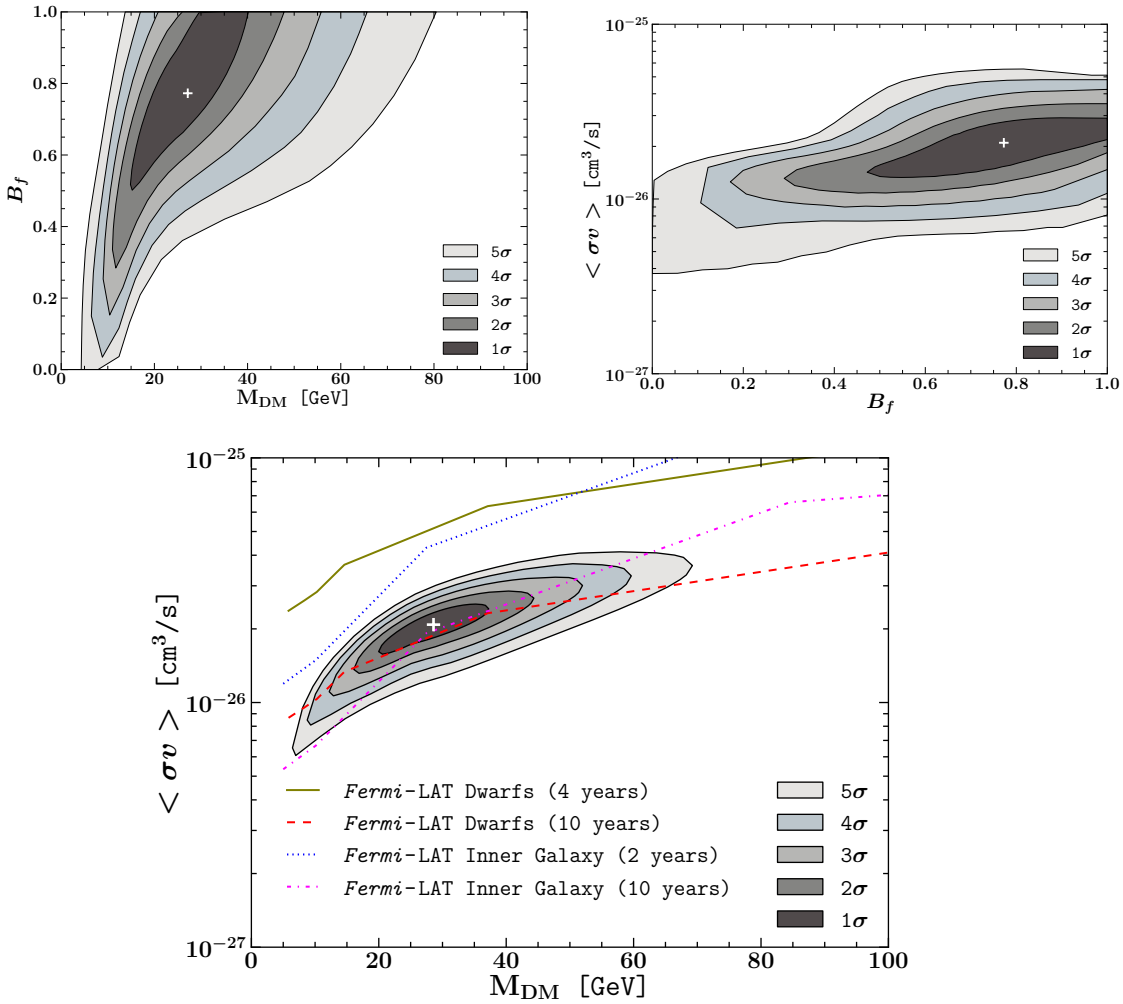

Figure 4.6: Confidence regions for the dark matter model when the Galactic Ridge source was included. The data used is shown in the top RHS panel of Fig. 4.2 and listed in Table 4.5. The parameter $B_f = 1.0$ implies 100% $b\bar{b}$ and $B_f = 0.0$ means 100% $\tau^+\tau^-$. The DM spatial distribution follows a NFW profile with inner slope $\gamma = 1.2$. The white cross denotes the best-fit values. Limits from dwarf galaxies [The Fermi-LAT Collaboration, 2013] (2σ) and the Inner Galaxy ($10^\circ \leq b \leq 20^\circ$) ($3\sigma$) [Ackermann et al., 2012] are included. We rescaled the Inner Galaxy results to account for the different γ of the current study, using the Galactic coordinate ($l = 0, b = 10$) as a reference point Chapter 3. The 10 year forecasts were approximated with a simple $1/\sqrt{\text{time}}$ scaling and in the dwarf galaxy case it was assumed there were three times more dwarf galaxies available.

4.6 Discussion

The main focus of our study was try to evaluate three competing explanations for the GCEG: MSPs, DM, or a Galactic Ridge resulting from the interaction of cosmic rays with molecular clouds. As we discuss below, the data prefer combinations of the Galactic Ridge template and a $\mathrm{NFW}^2_{1.2}$ template which has a spectrum compatible with either MSPs, DM, or some combination of the two.

4.6.1 Interaction of cosmic rays with molecular clouds

From Table 4.1 we can check the significance of adding a new component by evaluating the test statistic (TS) which is defined as in Eq. 2.1.

In the large sample limit, under the no source hypothesis, TS has a $\chi^2/2$ distribution with the number of degrees of freedom equal to the number of parameters associated with the proposed positive amplitude new source Mattox et al. [1996]; Wilks [1938]. As the amplitude is restricted to be non-negative, a $\chi^2/2$ distribution rather than the χ^2 distribution is needed.

As can be seen from Table 4.1, the improvement in the fit of the 20-cm Galactic Ridge relative to 2FGL is TS$= 648 - 425 = 213$ for $13 - 9 = 4$ extra degrees of freedom (dof). This corresponds to a 14σ detection (if we convert to the equivalent p-value for 1 degree of freedom) and so confirms that the 20-cm Galactic Ridge does improve the fit to the GCEG. However, the corresponding TS for a $\mathrm{NFW}^2_{1.2}$ template is 870 and for only 3 extra dof and so clearly also improves the fit substantially.

We can check whether the 20-cm Galactic Ridge still improves the fit once the $\mathrm{NFW}^2_{1.2}$ template is included. From Table 4.1 we obtain a TS$= 1330 - 1295 = 35$ for 4 extra dof which corresponds to a 5σ detection. This shows that the GCEG motivates a sum of the $\mathrm{NFW}^2_{1.2}$ and the Galactic Ridge being included.

The parts of the data which require the $\mathrm{NFW}^2_{1.2}$ and the 20-cm Galactic Ridge are shown in Fig. 4.3. The elongation in the longitudinal direction, indicating the need for the 20-cm Galactic Ridge, is particularly evident in the energy ranges 1.73 to 5.57 GeV.

We also did the above analysis with the HESS residual Galactic Ridge and we found that a TS=30 for 4 extra dof which is less than the 20-cm case, but the

difference is not statistically significant.

Additionally, we checked whether the inclusion of the Galactic Ridge affected the spectral parameters of the $\mathrm{NFW}^2_{1.2}$ model. As can be seen from Tables 4.3 and 4.4, the inclusion of the Galactic Ridge does not significantly alter the spectral parameters of the $\mathrm{NFW}^2_{1.2}$ template.

In Yusef-Zadeh et al. [2013], it was argued that the Arc and Sgr B were associated with cosmic rays interacting with molecular clouds and so should not be included when evaluating the parameters of the Galactic Ridge. They also investigated the effects of adding Sgr C, but we found once the $\mathrm{NFW}^2_{1.2}$ was included, Sgr C had a very low TS and so we have not included it in our analysis.

As can be seen from Table 4.1, the Arc and Sgr B do significantly improve the fit even when the Galactic Ridge and the $\mathrm{NFW}^2_{1.2}$ template are included. However, it is common practice Ackermann et al. [339]; Uchiyama et al. [2012] to exclude such point sources when analyzing a physical model for the cosmic rays interacting with molecular gas. Otherwise, some of the signal will be lost to the apparent point sources arising from cosmic rays interacting with molecular gas. As shown in Table 4.1, in this case there is also no significant difference in the goodness of fit between HESS Galactic Ridge and 20-cm Galactic Ridge, but as the 20-cm template has a slightly higher TS in both models 1 and 2, we use it as the default.

In Fig. 4.4 we provide confidence regions for the magnetic field B and hydrogen density n_H. The Galactic Ridge is consistent with the Yusef-Zadeh et al. [2013] best fit even though the extra $\mathrm{NFW}^2_{1.2}$ component is included.

4.6.2 Millisecond Pulsars

In Fig. 4.5 we show the confidence intervals for the exponential cut off fit. Although, they are not significantly different from the ones without an extended Galactic Ridge template (see Chapter 3), here we also show the MSPs reported in the second Fermi LAT catalog of gamma-ray pulsars (2FPC) Abdo et al. [2013] and also the globular clusters which can contain multiple unresolved MSPs Abdo et al. [2010]. As can be seen the spectrum of the GCEG is consistent with the majority of MSPs and MSP containing globular clusters.

E_{min}	E_{max}	dN/dE	Stat. Error	Syst. Error	TS
0.30	0.40	1.11×10^{-6}	6.41×10^{-7}	3.92×10^{-7}	3.06
0.40	0.54	7.17×10^{-7}	6.71×10^{-8}	2.84×10^{-7}	5.93
0.54	0.72	4.28×10^{-7}	4.54×10^{-8}	1.26×10^{-7}	10.45
0.72	0.97	3.02×10^{-7}	3.05×10^{-8}	7.98×10^{-8}	25.21
0.97	1.29	1.95×10^{-7}	2.57×10^{-8}	3.80×10^{-8}	49.1
1.29	1.73	1.23×10^{-7}	1.81×10^{-8}	1.83×10^{-8}	73.51
1.73	2.32	5.44×10^{-8}	1.48×10^{-8}	9.38×10^{-9}	63.94
2.32	3.11	3.39×10^{-8}	7.25×10^{-9}	4.35×10^{-9}	84.03
3.11	4.16	1.33×10^{-8}	6.11×10^{-9}	1.98×10^{-9}	43.3
4.16	5.57	3.42×10^{-9}	3.17×10^{-9}	3.17×10^{-9}	10.46
5.57	7.47	2.26×10^{-9}	6.97×10^{-10}	3.01×10^{-10}	14.14
7.47	10.00	1.21×10^{-9}	2.51×10^{-10}	2.40×10^{-10}	12.82
10.00	100.00	–	–	–	0.12

Table 4.5: $\text{NFW}^2_{1.2}$ spectrum and corresponding statistical and systematic errors using model 1 in Table 4.1. The spectral points dN/dE [GeV^{-1} cm^{-2} s^{-1}] were obtained at the logarithmic midpoint of each band. Energy is presented in GeV and Errors are [GeV^{-1} cm^{-2} s^{-1}].

E_{min}	E_{max}	dN/dE	Stat. Error	Syst. Error	TS
0.30	0.40	–	–	–	0.0
0.40	0.54	2.70×10^{-7}	7.19×10^{-8}	9.21×10^{-8}	5.04
0.54	0.72	1.24×10^{-7}	3.41×10^{-8}	5.57×10^{-8}	5.42
0.72	0.97	1.14×10^{-7}	2.13×10^{-8}	4.83×10^{-8}	20.71
0.97	1.29	5.32×10^{-8}	1.11×10^{-8}	4.35×10^{-8}	18.53
1.29	1.73	2.45×10^{-8}	7.20×10^{-9}	9.16×10^{-9}	16.49
1.73	2.32	1.39×10^{-8}	3.19×10^{-9}	7.09×10^{-9}	19.42
2.32	3.11	7.63×10^{-9}	1.71×10^{-9}	1.98×10^{-9}	22.89
3.11	4.16	5.04×10^{-9}	1.39×10^{-9}	8.02×10^{-10}	33.45
4.16	5.57	2.05×10^{-9}	3.83×10^{-10}	3.68×10^{-10}	21.57
5.57	7.47	7.67×10^{-10}	2.64×10^{-10}	1.59×10^{-10}	8.82
7.47	10.00	2.37×10^{-10}	1.10×10^{-10}	8.06×10^{-11}	3.02
10.00	100.00	3.53×10^{-12}	1.90×10^{-11}	5.69×10^{-12}	1.06

Table 4.6: Galactic Ridge spectrum generated using model 2 in Table 4.1.

Using the GCEG energy flux for 100 MeV$\leq E \leq$ 100 GeV (G_{100}) of our best fit exponential cut off model from Table 4.3 we evaluate the luminosity as $L_\gamma = 4\pi d^2 G_{100} \sim 10^{37}$ erg s^{-1} where we take the distance to the Galactic Center as $d \sim 8$ kpc.

The 2FPC contains 40 MSPs with estimated luminosities ranging from about 5×10^{31} to 7×10^{34} erg s^{-1}. The average MSP luminosity in the 2FPC is $\bar{L}_{\rm MSP} \sim 10^{34}$ erg s^{-1}. Only about 20% of known MSPs have been detected by Fermi-LAT Abdo et al. [2013] and so the catalog is biased towards higher gamma-ray luminosity MSPs. Therefore, we expect the 2FPC average MSP luminosity will be greater than the MSP population average. So we use the average 2FPC value to estimate a lower bound of $\sim$ 1000 MSPs for $r \lesssim$ 150pc in order to explain the GCEG.

If we assume each of the MSPs at the Galactic Center has a luminosity of $\bar{L}_{\rm MSP}$ and then convert this to a flux using $d \sim 8$ kpc we get each MSP at the Galactic Center has a flux $\sim 10^{-12}$ erg cm $^{-2}$ s^{-1} which, as can be seen from Fig. 17 of Abdo et al. [2013], is below the detection limit ($\sim 10^{-11}$ erg cm $^{-2}$ s^{-1}) at the Galactic Center. This is consistent with these proposed Galactic Center MSPs being unresolved.

The Galactic Center $r \lesssim$ 150 pc region corresponds to about 6 square degrees. As the Fermi-LAT resolution is $\gtrsim 0.1^\circ$ at the relevant energy level of this work, it follows that each (0.1 deg)^2 pixel of the Fermi-LAT image of the Galactic Center would contain $\gtrsim$ 1 MSP.

This MSPs explanation of the GCEG is consistent with the results presented in Wharton et al. [2012]. Their analysis is based on the number of neutron stars which are computed from the core collapse supernovae rate which in turn is obtained from measurements of the total mass of ^{26}Al in the Galaxy. Using this method they estimate the number of MSPs as $\sim 10^5 f_r$ for $r \lesssim$ 150 pc where f_r is the fraction of neutron stars that get recycled to MSPs. Based on Galactic disk and globular cluster radio observations, they estimate $f_r \sim 10^{-2}$ for $r \lesssim$ 150 pc.

A justification for the MSPs resulting in a NFW$^2_{1.2}$ profile with $\gamma \sim 1.2$ was proposed in Abazajian & Kaplinghat [2012a] who noted the observations of low mass X-ray binaries (LMXBs) in M31 follow a similar profile and MSPs are believed to arise from LMXBs. They also note some indication of a similar trend

in the Milky Way although the LMXB observational data in that case is currently not very conclusive.

4.6.3 Dark Matter

Although the estimates for the DM parameters are not significantly changed, as can be seen from Fig. 4.6, the $\tau^+\tau^-$ channel is now only excluded as 4σ rather than 5σ as was the case when no Galactic Ridge was included (see Chapter 3). As can be seen in the bottom panel of Fig. 4.6, neither Fermi-LAT dwarfs nor the Fermi-LAT inner Galaxy will be able to definitively detect the DM self-annihilation if it is causing the GCEG. Also, as there is likely to be at least some MSP contribution, the actual $\langle\sigma v\rangle$ will be correspondingly lower and so even harder to detect.

4.7 Conclusions

We have found that the GCEG is best fit by adding to the base 2FGL model both a $\mathrm{NFW}^2_{1.2}$ source and a Galactic Ridge based on a 20-cm continuum emission template. Similar results were found for a Galactic Ridge template based on the HESS data residuals. The addition of the Galactic Ridge was not found to significantly affect the $\mathrm{NFW}^2_{1.2}$ spectral parameters. We found that the GCEG is consistent with a lower bound of ~ 1000 on the number of MSPs at the Galactic Center. This is consistent with estimates based on core collapse supernovae inferences from ^{26}Al measurements. We also demonstrated that current and 10-year Fermi-LAT measurements of dwarf spheroidals and the inner Galaxy are unlikely to be able to conclusively check a DM annihilation explanation of the GCEG. As the modeling based on the ^{26}Al measurements indicates there is likely to be ~ 1000 MSPs in the Galactic Center, this implies that if there is a DM annihilation component then it probably has a significantly smaller $\langle\sigma v\rangle$ and so will be even harder to check.

We also constrained a bremsstrahlung model of the Galactic Ridge and showed that the B and n_H constraints are consistent with a previous analysis [Yusef-Zadeh et al., 2013] done without a $\mathrm{NFW}^2_{1.2}$ component.

Chapter 5

Summary and Conclusions

Searches for a signature of annihilating DM have been carried out in dwarf galaxies Ackermann et al. [2011]; Geringer-Sameth & Koushiappas [2011] and Galaxy clusters (e.g., . Ando & Nagai [2012]; Han et al. [2012d]; Chapter 2). Amongst the best candidates are massive nearby clusters such as Virgo, Fornax or Coma Pinzke et al. [2011]. Interestingly a recent paper Han et al. [2012a] claimed a 4.4σ detection of DM emission in the Virgo cluster. However, in Chapter 2 we have refuted this claim by showing that the measured excess γ-ray emission was mainly due to the appearance of a population of previously unresolved γ-ray point sources in the region of interest (beyond those found in the two year catalogue Nolan [2012]). These are likely to be Active Galactic Nuclei (AGN) or radio galaxies (Chapter 2). Our results were later confirmed in Han et al. [2012d], they showed that removing the previously-unaccounted-for astrophysical point sources, one can impose stringent bounds using the same Virgo cluster observation.

Several groups have reported evidence of extended excess γ-ray emission above the diffuse galactic background from the central $1^\circ - 2^\circ$ around the Galactic Center that is consistent with WIMPs of roughly $10-100$ GeV mass annihilating into $\tau^+\tau^-$ or $b\bar{b}$ final states or a combination of both Abazajian et al. [2014]; Abazajian & Kaplinghat [2012b]; Daylan et al. [2014]; Goodenough & Hooper [2009b]; Hooper & Linden [2011b]; Chapters 3 and 4. The signal was also shown to be consistent with a population of millisecond pulsars in the Galactic Center (see Chapters 3 and 4). A preliminary study by the Fermi-LAT Collaboration reported an excess in observed counts around energies of $2-5$ GeV Morselli et al.

[2011]; Vitale et al. [2011]. In Chapters 3 and 4, we corrected the estimates made in Goodenough & Hooper [2009b]; Hooper & Linden [2011b] (and references therein by the same research group). This was possible as in our approach we marginalized over the point sources parameters – which present a large degeneracy with any proposed model for the excess Galactic Center Emission.

In Chapter 3 we extended the treatment in Abazajian & Kaplinghat [2012b] in a number of ways. Firstly we estimated the uncertainties in a way which was similar to that done in the analysis of the Supernova remnant W49B Abdo et al. [2010]. This entailed examining the residuals away from the Galactic Center. We did a band analysis which we checked could act as an efficient form of data compression. We then redid the band analysis with spatial and systematic errors added to the data. By examining the change in the band analysis we estimated the systematic error at around 20%. We then estimated confidence intervals for different model parameters and also evaluated the goodness of fit. We obtained that the optimal fit was a ratio of 3 to 1 of of $b\bar{b}$ to $\tau^+\tau^-$ with a cross-section of $\langle\sigma v\rangle = 2\times10^{-26}$ cm^3 s^{-1} and a mass of about 24 GeV. This is intriguing as these are natural values from the WIMP paradigm Bertone et al. [2005].

Importantly, by measuring the gamma-ray spectrum we showed that it would be hard to explain the data with only prompt emission from a pure leptophilic model, we demonstrated that WIMPs models with branching ratios near 100% in the $\tau^+\tau^-$ channel are ruled out at 5σ if the effects of diffusion of the resulting secondary leptons are not considered. However, as subsequently shown by Lacroix et al. [2014], the effects of diffusion and other secondary leptons can make the $\tau^+\tau^-$ channel acceptable. This has a negligible effect on the $b\bar{b}$ channel. Notwithstanding we found that the average measured Fermi-LAT millisecond pulsar spectrum was also a good fit. In fact, our analysis showed that a superposition of $\sim 10^3$ millisecond pulsars (MSPs) within a radius of $r \lesssim 150$ pc of the Galactic Center whose number density follows a generalized NFW profile was also strongly favored by the data. We notice that these results go beyond the work of Abazajian & Kaplinghat [2012b] as we present confidence level intervals for the full parameter space of the models considered as well as take into account uncertainties in the Galactic diffuse emission model.

Studies have also looked at the possibility of the signal arising from cosmic-ray

interaction with gas in the Galactic Center Hooper & Linden [2011b]; Linden et al. [2012b]; Yusef-Zadeh et al. [2013]; Chapters 4. This alternative solution can be divided in two different scenarios; the hadronic and nonthermal bremsstrahlung. The first one consists of π^0 decays resulting from the emission of high energy protons and their subsequent collision with gas in the Galactic Center. In Linden & Profumo [2012] it was found that a model based on hadronic emission from Sgr A* would appear point-like to the Femi-LAT γ-ray detector. This would be in conflict with the apparent extended nature of the galactic center γ-ray excess. The second scenario, the nonthermal bremsstrahlung emission model, is mainly motivated by a thorough radio data analysis of the central $\sim$ 200 pc region of the GC Yusef-Zadeh et al. [2013]. Based on observations obtained with the Green Bank Telescope (GBT), Susaku, XMM-Newton, Chandra, Fermi-LAT and HESS it was argued Yusef-Zadeh et al. [2013] that the γ-ray Galactic Center excess emission is generated by a population of synchrotron emitting electrons interacting with gas in molecular clouds.

In Chapter 4 we scrutinized the non-thermal brehmsstrahlung model using rigorous techniques of accounting for the systematic uncertainties in the Galactic diffuse emission model. We determined the relative likelihoods of the non-thermal bremsstrahlung emission model and DM (or MSPs) explanation for the excess emission. This was done by adding a Galactic Ridge component to our model of the Galactic Center that already included a DM (or MSPs) source. Then using a spatial template fitting technique we obtained that the test statistics of the DM (or MSPs) source is still at least four times higher than that of the Galactic Ridge with non-thermal bremsstrahlung spectrum. Importantly the GC excess emission is best fit by adding to the base 2FGL Nolan [2012] γ-ray point sources catalog model both a DM (or MSPs) source and a new population of non-thermal bremsstrahlung interacting CR electrons. The addition of the Galactic Ridge was not found to significantly affect the DM spectral parameters. We found that the γ-ray data from the GC is consistent with a lower bound of $\sim$ 1000 on the number of MSPs at the Galactic Center. This agrees with estimates based on core collapse supernovae inferences from ^{26}Al measurements Wharton et al. [2012]. We also constrained the parameter space of the bremsstrahlung model of the Galactic Ridge and showed that if a 20 cm Galactic Ridge template is used, then the

Galactic magnetic field B and the average total gas density n_H constraints are consistent with a previous analysis Yusef-Zadeh et al. [2013] done without a DM or MSPs component.

Indirect detection experiments, such as the Fermi-LAT and H.E.S.S. are starting to probe the thermal relic interaction rate. However, as we have discussed extensively in this thesis, uncertainties about the dark matter density distributions and the astrophysical backgrounds have a serious impact on the detectability of DM annihilation signals. Ultimately, a DM signal will only be convincing if it is detected in multiple sources and all astrophysical alternatives have been ruled out.

Appendix A: Nonthermal Bremsstrahlung Spectrum

In this appendix we discuss the relevant synchrotron and bremsstrahlung formula which were used in the analysis of chapter 4 and Ref. [Yusef-Zadeh et al., 2013]. As these formulas are only briefly alluded to in Ref. [Yusef-Zadeh et al., 2013] we provide more details here which are based on notes kindly supplied to us by Prof. Mark Wardle.

Relativistic cosmic ray electrons that are deflected in the Coulomb field of nuclei in molecular clouds at the Galactic Center emit bremsstrahlung γ-ray photons [Schlickeiser, 2002]. In this region the ionized gas component contribution to the radiation process can be neglected [Schlickeiser, 2002]. By considering this the differential cross section for the bremsstrahlung interaction [Bethe & Heitler, 1934; Schlickeiser & Thielheim, 1978] can be written as[1]

$$\sigma(E_\gamma,\gamma) = \frac{3}{8\pi E_\gamma}\,\alpha\,\sigma_T\,\Phi_{\rm H}\left[\frac{4}{3}-\frac{4}{3}\frac{E_\gamma}{E}+\left(\frac{E_\gamma}{E}\right)^2\right] \quad {\rm cm}^2\ {\rm eV}^{-1} \tag{1}$$

where E_γ is the photon energy, $E=\gamma mc^2$ the relativistic electron energy, $\alpha = 1/137.0$ the fine structure constant, $\sigma_T = 6.652\times10^{-25}$ cm^2 the Thomson cross section and $\Phi_{\rm H}\simeq 45$ the scattering function assumed to be in the strong-shielding limit which is appropriate for relativistic electrons. We take the invariant electron

[1] We note that Eq. 4.4.1 of Ref. [Schlickeiser, 2002] is missing a factor of $1/E_\gamma$.

mass to be $m = 9.109 \times 10^{-28}$ g [Beringer et al., 2012b] and for the speed of light we use $c = 2.998 \times 10^{10}$ cm/s.

The nonthermal electron bremsstrahlung omnidirectional source function produced by a single relativistic electron in a medium dominated by atomic and molecular hydrogen nuclei of corresponding number density $n_{\rm H} = n_{\rm HI} + 2n_{\rm H_2}$ is given by [Schlickeiser, 2002]

$$\begin{aligned} q(E_\gamma) &= c\, n_{\rm H} \int_{E_{\rm L}}^{+\infty} d\gamma\; n(\gamma)\; \sigma(E_\gamma, \gamma) \\ &\quad \text{photons cm}^{-3}\ \text{s}^{-1}\ \text{eV}^{-1} \end{aligned} \tag{2}$$

where $E_{\rm L} = \max(E_\gamma, E_1)$ and $E_1 = \gamma_1 mc^2$ represents a low-energy cutoff in the electron distribution. The energy distribution function $n(\gamma)$ of the radiating relativistic electrons is assumed to follow a broken power law of the form

$$n(\gamma) = \begin{cases} n_1\ \gamma^{-p_1} & \text{if } 1 \leq \gamma \leq \gamma_b \\ n_2\ \gamma^{-p_2} & \text{if } \gamma \geq \gamma_b, \end{cases} \quad \text{cm}^{-3} \tag{3}$$

with $n_1 \gamma_b^{-p_1} = n_2 \gamma_b^{-p_2} \equiv n_b$ and $E_b = \gamma_b mc^2$ the break energy. After substituting Eq. 1 and 3 into Eq. 2 and solving the corresponding integrals we get for the omnidirectional source function

$$\begin{aligned} q(E_\gamma) &= \frac{3\ \alpha\ \sigma_T}{8\pi} \Phi_{\rm H}\ n_{\rm H} \frac{n_b}{mc}\ J\left(E_\gamma / E_b\right) \\ &\quad \text{photons cm}^{-3}\ \text{s}^{-1} \text{eV}^{-1}, \end{aligned} \tag{4}$$

where

$$J(x) = \begin{cases} \left[I_{p_1}(1) - I_{p_1}(1/x)\right] x^{-p_1} + I_{p_2}(1/x)\ x^{-p_2} & \text{for } x < 1 \\ I_{p_2}(1)\ x^{-p_2} & \text{for } x \geq 1, \end{cases} \tag{5}$$

and

$$I_{p_i}(x) = \frac{1}{3}x^{-p_i}\left(\frac{3}{x+p_i\,x}+\frac{4x}{p_i-1}-\frac{4}{p_i}\right) \quad \text{for } i=1,2. \tag{6}$$

In Ref. [Yusef-Zadeh et al., 2013] it was argued that the morphological distribution of diffuse radiation from the GC measured at 1.45 GHz, GeV and TeV energies is correlated. Importantly, in that work it was assumed that all the synchrotron emitting electrons are interacting with the molecular clouds. It is thus interesting to find an expression for the bremsstrahlung spectrum in terms of the synchrotron flux.

Synchrotron emission at frequency ν (taken to be the characteristic synchrotron radiation frequency) is associated with particles of energy (see Eq. 4.1.9 of [Schlickeiser, 2002])

$$\begin{aligned} E_\nu &= \gamma_\nu mc^2 \\ &= \left(\frac{4\pi mc\nu}{3eB}\right)^{1/2} mc^2 \\ &= 7.89\left(\frac{B}{\mu\text{G}}\right)^{-1/2}\left(\frac{\nu}{\text{GHz}}\right)^{1/2} \quad \text{GeV}\,. \end{aligned} \tag{7}$$

where the electron charge is $e = 4.803\times10^{-10}$ statcoulomb. Eq. 7 can be rewritten as

$$\gamma_\nu = \left(\frac{\nu}{\nu_B}\right)^{1/2} \text{where } \nu_B = \frac{3eB}{4\pi mc} = 4.20\left(\frac{B}{\mu\text{G}}\right) \quad \text{Hz}. \tag{8}$$

We therefore obtain that particles radiating at the synchrotron break frequency

ν_b obey the relation

$$\nu_b = \nu_B \gamma_b^2 \quad \text{Hz.} \tag{9}$$

The synchrotron emission coefficient resulting from an electron spectrum that is a simple power law can be obtained from Eq.(6.36) of Ref. [Rybicki & Lightman, 1985] which can be rewritten as

$$j_\nu = \frac{1}{\sqrt{3}} f_j(p) \frac{e^2}{c} \, \nu_B \, \gamma_\nu \, n\left(\gamma_\nu\right) \quad \text{erg cm}^{-3}\,\text{ster}^{-1}\,\text{s}^{-1}\,\text{Hz}^{-1} \tag{10}$$

where

$$f_j(p) = \frac{2^{(p-1)/2}}{p+1} \Gamma\left(\frac{3p-1}{12}\right) \Gamma\left(\frac{3p+19}{12}\right), \tag{11}$$

and $\Gamma(z)$ is the Gamma function. Using Eq. 10 we can estimate the emission coefficient for a broken power law at the synchrotron break frequency

$$j_b = \tilde{j} n_b \quad \text{erg cm}^{-3}\,\text{ster}^{-1}\,\text{s}^{-1}\,\text{Hz}^{-1}, \tag{12}$$

where

$$\tilde{j} = \frac{1}{\sqrt{3}} \bar{f}_j(p) \frac{e^2}{c} \sqrt{\nu_B \nu_b} \quad \text{erg ster}^{-1}\,\text{s}^{-1}\,\text{Hz}^{-1}, \tag{13}$$

and

$$\bar{f}_j(p) = \frac{1}{2}\left[f_j(p_1) + f_j(p_2)\right]. \tag{14}$$

where p_1 and p_2 are the broken power law spectral indices before and after the

break.

Then the spectral value of synchrotron radiation from a source of volume V at a distance d at the break frequency is given by

$$S_b = 4\pi \frac{\tilde{j} n_b V}{4\pi d^2} \quad \text{Jy}. \tag{15}$$

Finally, the source function given in Eq. 4 is multiplied by a factor V to get the photon luminosity spectrum and then divided by $4\pi d^2$ to obtain the bremsstrahlung photon flux spectrum and using the results of Eq 15 we thus get for the bremsstrahlung γ-ray spectrum

$$\begin{aligned} \frac{dN_{\rm brem}}{dE_\gamma} &= \frac{3\ \alpha\ \sigma_T}{32\pi^2 \tilde{j}} \Phi_{\rm H}\ n_{\rm H} \frac{S_b}{mc}\ J\left(E_\gamma/E_b\right) \\ &\quad \text{photons erg}^{-1}\ \text{cm}^{-2}\ \text{s}^{-1}, \end{aligned} \tag{16}$$

where $J\left(E_\gamma/E_b\right)$ is given by Eq. 5.

References

Aad, G., et al. 2013, JHEP, 1304, 075 xi, 10

Aalseth, C., et al. 2013, Phys.Rev., D88, 012002 xi, 8

Abazajian, K. N. 2011, JCAP, 1103, 010 31

Abazajian, K. N., Canac, N., Horiuchi, S., & Kaplinghat, M. 2014, arXiv:1402.4090 [astro-ph.HE] 84

Abazajian, K. N., & Kaplinghat, M. 2012a, Phys.Rev., D86, 083511 30, 31, 32, 34, 35, 39, 52, 53, 56, 63, 66, 82

—. 2012b, Phys.Rev., D86, 083511 84, 85

—. 2013, Phys. Rev. D, 87, 129902 30, 31, 32, 34, 35, 39, 52, 53, 56, 63, 66

Abdo, A., Ackermann, M., Ajello, M., et al. 2010, Astrophys.J., 722, 1303 43, 45, 85

Abdo, A., et al. 2013, Astrophys.J.Suppl., 208, 17 77, 80, 82

Abdo, A. A., et al. 2009, Science, 325, 845 63

—. 2010, , 524, A75 77, 80

Acciari, V., Aliu, E., Arlen, T., et al. 2009, arXiv:0911.0873 [astro-ph.CO] 15

Acero, F. 2009, arXiv:0909.4651 [astro-ph.HE] 15

Ackermann, M., Ajello, M., Allafort, A., et al. 2010, JCAP, 1005, 025 16

Ackermann, M., et al. 2011a, Phys.Rev.Lett., 107, 241302 30

—. 2011b, Phys.Rev.Lett., 107, 241302 55, 57, 58

Ackermann, M., Ajello, M., Albert, A., et al. 2011, Physical Review Letters, 107, 241302 84

Ackermann, M., et al. 2012, , 761, 91 78

Ackermann, M., et al. 2012a, The Astrophysical Journal, 750, 3 43, 63, 70

—. 2012b, Astrophys.J.Suppl., 203, 4 13, 31

—. 339, Science Magazine 2013, 807 31, 80

Ade, P., et al. 2014, Astron.Astrophys., arXiv:1303.5076 [astro-ph.CO] xi, 3

Agnese, R., et al. 2013, Phys.Rev.Lett., 111, 251301 xi, 8, 10

Aharonian, F., et al. 2006, , 439, 695 61, 67, 69, 71, 75

Akimov, D. Y., Araujo, H., Barnes, E., et al. 2012, Phys.Lett., B709, 14 xi, 8

Albornoz Vásquez, D., Belikov, A., Coc, A., Silk, J., & Vangioni, E. 2012, , 86, 063501 3

Ando, S., & Nagai, D. 2012, JCAP, 1207, 017 30, 84

Angloher, G., Bauer, M., Bavykina, I., et al. 2012, Eur.Phys.J., C72, 1971 xi, 8

Aprile, E., et al. 2013, Phys.Rev.Lett., 111, 021301 xi, 8

Armengaud, E., et al. 2011, Phys.Lett., B702, 329 xi, 8

Atwood, W., et al. 2009, Astrophys.J., 697, 1071 12

Bergstrom, L., Ullio, P., & Buckley, J. H. 1998, Astropart.Phys., 9, 137 11, 35, 39

Beringer, J., et al. 2012a, Phys. Rev. D, 86, 010001 53

—. 2012b, Phys.Rev., D86, 010001 89

Bernabei, R., et al. 2008, Eur.Phys.J., C56, 333 xi, 8

Bertone, G., Hooper, D., & Silk, J. 2005, , 405, 279 85

Bertone, G., Hooper, D., & Silk, J. 2005, Phys.Rept., 405, 279 4, 11

Bethe, H., & Heitler, W. 1934, Proc.Roy.Soc.Lond., A146, 83 88

Boehm, C., & Fayet, P. 2004, Nucl.Phys., B683, 219 4

Boyarsky, A., Malyshev, D., & Ruchayskiy, O. 2011, Phys.Lett., B705, 165 30, 39, 63

Brown, A. M., & Adams, J. 2012, arXiv:1201.0034 [astro-ph.HE] 18

Cembranos, J., de la Cruz-Dombriz, A., Gammaldi, V., Lineros, R., & Maroto, A. 2013, arXiv:1305.2124 [hep-ph] 41

Chiu, H.-Y. 1966, Phys.Rev.Lett., 17, 712 5

Ciafaloni, P., Comelli, D., Riotto, A., et al. 2011, JCAP, 1103, 019 42

Daylan, T., Finkbeiner, D. P., Hooper, D., et al. 2014, arXiv:1402.6703 [astro-ph.HE] 84

Diffuse, & Collaboration, M. C. S. W. G. F. L. A. T. 2009, Description and Caveats for the LAT Team Model of Diffuse Gamma-Ray Emission, Version: gll_iem_v02.fit, http://fermi.gsfc.nasa.gov/ssc/data/access/lat/ring_for_FSSC_final4.pdf 68, 70

Dugger, L., Jeltema, T. E., & Profumo, S. 2010, JCAP, 1012, 015 16

Gao, L., Frenk, C., Jenkins, A., Springel, V., & White, S. 2012, Mon.Not.Roy.Astron.Soc., 419, 1721 15, 16, 24

Geringer-Sameth, A., & Koushiappas, S. M. 2011, Phys.Rev.Lett., 107, 241303 30, 84

Gondolo, P., Edsjo, J., Ullio, P., et al. 2004, JCAP, 0407, 008 41

Goodenough, L., & Hooper, D. 2009a, arXiv:0910.2998 [hep-ph] 30, 39, 65

—. 2009b, arXiv:0910.2998 [hep-ph] 84, 85

Goodman, M. W., & Witten, E. 1985, Phys.Rev., D31, 3059 6

Gordon, C., & Macias, O. 2013, arXiv:1306.5725 [astro-ph.HE] v

—. 2014, arXiv:1410.7840 [astro-ph.HE] v

Gordon, C., & Macias, O. 2014, in IAU Symposium, Vol. 303, IAU Symposium, ed. L. O. Sjouwerman, C. C. Lang, & J. Ott, 414 v

Han, J., Frenk, C. S., Eke, V. R., Gao, L., & White, S. D. 2012a, arXiv:1201.1003 [astro-ph.HE] 16, 17, 34, 84

Han, J., Frenk, C. S., Eke, V. R., et al. 2012b, arXiv:1207.6749 [astro-ph.CO] 27

—. 2012c, Mon.Not.Roy.Astron.Soc., 427, 1651 35

Han, J., et al. 2012d, Mon.Not.Roy.Astron.Soc., 427, 1651 30, 84

Hooper, D., Cholis, I., Linden, T., Siegal-Gaskins, J., & Slatyer, T. 2013a, Phys.Rev., D88, 083009 31

—. 2013b, arXiv:1305.0830 [astro-ph.HE] 50, 52, 63

Hooper, D., & Goodenough, L. 2011, Phys.Lett., B697, 412 30, 39, 62

Hooper, D., Kelso, C., & Queiroz, F. S. 2012, arXiv:1209.3015 [astro-ph.HE] 30, 61

Hooper, D., & Linden, T. 2011a, Phys.Rev., D84, 123005 30, 39, 56, 58, 59, 60, 61, 62, 65

—. 2011b, Phys.Rev., D84, 123005 84, 85, 86

Hooper, D., & Slatyer, T. R. 2013, arXiv:1302.6589 [astro-ph.HE] 31, 62, 63

Huang, W.-C., Urbano, A., & Xue, W. 2013, arXiv:1307.6862 [hep-ph] 31

Huang, X., Vertongen, G., & Weniger, C. 2012, JCAP, 1201, 042 16, 21

Iocco, F., Pato, M., Bertone, G., & Jetzer, P. 2011, JCAP, 1111, 029 30, 41, 61, 62

James, F., & Roos, M. 1975, Comput.Phys.Commun., 10, 343 52, 53

Jeltema, T. E., Kehayias, J., & Profumo, S. 2009, Phys.Rev., D80, 023005 16

Jeltema, T. E., & Profumo, S. 2008, JCAP, 0811, 003 24, 41, 76

Kachelriess, M., Serpico, P., & Solberg, M. A. 2009, Phys.Rev., D80, 123533 42

Klypin, A., Zhao, H., & Somerville, R. S. 2002, , 573, 597 40

Lacroix, T., Boehm, C., & Silk, J. 2014, arXiv:1403.1987 [astro-ph.HE] 64, 85

Law, C. J., Yusef-Zadeh, F., Cotton, W. D., & Maddalena, R. J. 2008, , 177, 255 66, 67, 68

Linden, T., Lovegrove, E., & Profumo, S. 2012a, Astrophys.J., 753, 41 30, 65

—. 2012b, Astrophys.J., 753, 41 86

Linden, T., & Profumo, S. 2012, Astrophys.J., 760, 23 86

Macias, O., Crocker, R., Gordon, C., & Profumo, S. 2014, arXiv:1410.1678 [astro-ph.HE] v

Macias, O., & Gordon, C. 2014, Phys.Rev., D, arXiv:1312.6671 [astro-ph.HE] v

Macias, O., Gordon, C., Brown, A. M., & Adams, J. 2012, Phys.Rev., D86, 076004 v, 27

Mattox, J., Bertsch, D., Chiang, J., et al. 1996, Astrophys.J., 461, 396 17, 19, 26, 32, 79

Mirabal, N. 2013, , 436, 2461 31

Mitsou, V. A. 2013, Int.J.Mod.Phys., A28, 1330052 9

Morselli, A., Canadas, B., & Vitale, V. 2011, Nuovo Cim., C034N3, 311 84

Navarro, J. F., Frenk, C. S., & White, S. D. 1996, Astrophys.J., 462, 563 40

Nolan, P. L. 2012, Astrophys.J.Suppl., 199, 31 16, 18, 19, 21, 24, 26, 30, 32, 34, 42, 45, 49, 52, 67, 68, 70, 84, 86

Peacock, J. A., Cole, S., Norberg, P., et al. 2001, , 410, 169 3

Perlmutter, S., Aldering, G., Goldhaber, G., et al. 1999, , 517, 565 3

Pinzke, A., & Pfrommer, C. 2010, arXiv:1001.5023 [astro-ph.CO] 16

Pinzke, A., Pfrommer, C., & Bergstrom, L. 2009, Phys.Rev.Lett., 103, 181302 15

—. 2011, Phys.Rev., D84, 123509 15, 16, 84

Planck Collaboration, Ade, P. A. R., Aghanim, N., et al. 2013, ArXiv e-prints, arXiv:1303.5062 2

Profumo, S. 2013, arXiv:1301.0952 [hep-ph] 60

Refregier, A. 2003, , 41, 645 2

Rolke, W. A., López, A. M., & Conrad, J. 2005, Nuclear Instruments and Methods in Physics Research A, 551, 493 41, 52

Rubin, V. C., & Ford, Jr., W. K. 1970, , 159, 379 2

Rybicki, G. B., & Lightman, A. P. 1985 91

Scherrer, R. J., & Turner, M. S. 1986, Phys.Rev., D33, 1585 5

Schlickeiser, R. 2002, Cosmic Ray Astrophysics 88, 89, 90

Schlickeiser, R., & Thielheim, K. O. 1978, , 182, 103 88

Schumann, M. 2014, Braz.J.Phys., 44, 483 xi, 8, 10

Sjostrand, T., Mrenna, S., & Skands, P. Z. 2006, JHEP, 0605, 026 41

—. 2008, Comput.Phys.Commun., 178, 852 42

Steigman, G. 1979, Ann.Rev.Nucl.Part.Sci., 29, 313 5

Steigman, G., Dasgupta, B., & Beacom, J. F. 2012, Phys.Rev., D86, 023506 60

Strong, A., & Moskalenko, I. 1998, Astrophys.J., 509, 212 70

Suzuki, N., Rubin, D., Lidman, C., et al. 2012, , 746, 85 3

The Fermi-LAT Collaboration. 2012, ArXiv e-prints, arXiv:1202.4039 [astro-ph.HE] 13, 14

—. 2013, ArXiv e-prints, arXiv:1310.0828 [astro-ph.HE] 78

Uchiyama, Y., Funk, S., Katagiri, H., et al. 2012, arXiv:1203.3234 [astro-ph.HE] 80

Vitale, V., & Morselli, A. 2009, arXiv:0912.3828 [astro-ph.HE] 30

Vitale, V., Morselli, A., & Fermi/LAT Collaboration. 2011, Nuclear Instruments and Methods in Physics Research A, 630, 147 30, 85

Vladimirov, A. E., Digel, S. W., Johannesson, G., et al. 2011, Comput.Phys.Commun., 182, 1156 70

Wharton, R. S., Chatterjee, S., Cordes, J. M., Deneva, J. S., & Lazio, T. J. W. 2012, , 753, 108 31, 82, 86

Wilks, S. S. 1938, Ann.Math.Stat., 9, 60 17, 26, 32, 79

Yusef-Zadeh, F., Hewitt, J., Wardle, M., et al. 2013, Astrophys.J., 762, 33 33, 34, 63, 65, 66, 67, 68, 69, 72, 75, 80, 83, 86, 87, 88, 90

Zeldovich, Y. B. 1965, Adv. Astron. Astrophys., 241 5

Zwicky, F. 1937, , 86, 217 1